(12)

OBJECTIVE ANALYSIS AND PREDICTION TECHNIQUES - 1984

Alan M. Gerlach (ed.)

AD-A160 377

Systems and Applied Sciences Corporation (SASC)
1577 Springhill Road, Suite 600
Vienna, VA 22180

November 30, 1984

Scientific Report No. 8
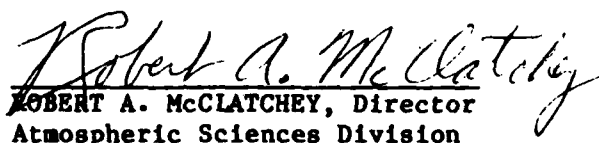
DTIC FILE COPY

DTIC
ELECTE
OCT 16 1985
S   D
B

85 10 16 109

This technical report has been reviewed and is approved for publication.

ALLAN J. BUSSEY
Contract Manager

FOR THE COMMANDER

ROBERT A. McCLATCHEY, Director
Atmospheric Sciences Division

This report has been reviewed by the ESD Public Affairs Office (PA) and is releasable to the National Technical Information Service (NTIS).

Qualified requestors may obtain additional copies from the Defense Technical Information Center. All others should apply to the National Technical Information Service.

If your address has changed, or if you wish to be removed from the mailing list, or if the addressee is no longer employed by your organization, please notify AFGL/DAA, Hanscom AFB, MA 01731. This will assist us in maintaining a current mailing list.

REPORT DOCUMENTATION PAGE

1a. REPORT SECURITY CLASSIFICATION	1b. RESTRICTIVE MARKINGS
UNCLASSIFIED	

2a. SECURITY CLASSIFICATION AUTHORITY	3. DISTRIBUTION/AVAILABILITY OF REPORT
2b. DECLASSIFICATION/DOWNGRADING SCHEDULE	Approved for public release; distribution unlimited

4. PERFORMING ORGANIZATION REPORT NUMBER(S)	5. MONITORING ORGANIZATION REPORT NUMBER(S)
	AFGL-TR-84-0328

6a. NAME OF PERFORMING ORGANIZATION	6b. OFFICE SYMBOL (If applicable)	7a. NAME OF MONITORING ORGANIZATION
Systems and Applied Sciences Corporation		Air Force Geophysics Laboratory

6c. ADDRESS (City, State and ZIP Code)	7b. ADDRESS (City, State and ZIP Code)
1577 Springhill Road, Suite 600 Vienna, VA 22180	Hanscom AFB, MA 01731 Monitor/LY/Allan J. Bussey

8a. NAME OF FUNDING/SPONSORING ORGANIZATION	8b. OFFICE SYMBOL (If applicable)	9. PROCUREMENT INSTRUMENT IDENTIFICATION NUMBER
Air Force Geophysics Laboratory	LY	Contract No. F19628-82-C-0023

8c. ADDRESS (City, State and ZIP Code)	10. SOURCE OF FUNDING NOS.			
	PROGRAM ELEMENT NO.	PROJECT NO.	TASK NO.	WORK UNIT NO.
Hanscom AFB, MA 01731				
11. TITLE (Include Security Classification) Objective Analysis and Prediction Techniques - 1984	62101F	6670	00	AC

12. PERSONAL AUTHOR(S)
Gerlach, Alan M. (ed.)

13a. TYPE OF REPORT	13b. TIME COVERED	14. DATE OF REPORT (Yr., Mo., Day)	15. PAGE COUNT
Scientific Rpt. No. 8	FROM 83/12/1 TO 84/11/30	84/11/30	168

16. SUPPLEMENTARY NOTATION

17.	COSATI CODES		18. SUBJECT TERMS (Continue on reverse if necessary and identify by block number)	
FIELD	GROUP	SUB GR	Objective analysis	Interactive forecasting
0401			Initialization	Mesocyclone detection/classification
0402			VAS data processing	Satellite cloud analysis

19. ABSTRACT (Continue on reverse if necessary and identify by block number)

This report summarizes weather research in several technical areas: in numerical weather prediction, development and joint test of two objective analysis methods (optimum interpolation and fitting procedure) for AFGL global spectral models, improved specification of moisture initial conditions, study of relocatable limited area models; in mesoscale forecasting, error analysis of LFM-II forecasts during winter seasons; in boundary layer meteorology specialized computer programs for studies of tropospheric scatter propagation, atmospheric chemical dispersion modeling, microwave refractive structure determination; in radar meteorology, study of single-Doppler detection of synoptic-scale wind anomalies, detection algorithm for gust front shear, development of mesocyclone detection-classification algorithm, detection of mesocyclone precursors, detection of aircraft icing regions; in satellite meteorology, study of satellite viewing angle bias in RTNEPH IR data, study of MDR data correlation with satellite imagery, development of microprocessor-based satellite data ingest system, system design (hardware, software) for McIDAS upgrade; in climatology, data processing studies for vertical temperature-density profiles for MIL STD 210 revision, data products

20. DISTRIBUTION/AVAILABILITY OF ABSTRACT	21. ABSTRACT SECURITY CLASSIFICATION
UNCLASSIFIED/UNLIMITED ☒ SAME AS RPT. ☐ DTIC USERS ☐	UNCLASSIFIED

22a. NAME OF RESPONSIBLE INDIVIDUAL	22b. TELEPHONE NUMBER (Include Area Code)	22c. OFFICE SYMBOL
Allan J. Bussey	(617) 861-2977	LY

DD FORM 1473, 83 APR EDITION OF 1 JAN 73 IS OBSOLETE

Box 19
for investigating VHR satellite sensor capabilities for improved small cumulus detection.

This interim scientific report details the results and status of research performed by Systems and Applied Sciences Corporation (SASC) under Contract F19628-82-C-0023 with the Atmospheric Sciences Division, Air Force Geophysics Laboratory, for the period December 1, 1983 to November 30, 1984.

Presentations vary in technical detail according to their subject matter, ranging from narrative descriptions of work accomplished to technical papers.

The contract calls for effort in six discrete areas, reported upon in the monthly R&D Status Reports under these headings:

> Numerical Weather Prediction
>
> Mesoscale Forecasting
>
> Boundary Layer Meteorology
>
> Radar Meteorology
>
> Satellite Meteorology
>
> Climatology

This report is organized similarly.

Personnel associated with these areas at any time during the reporting period were:

Numerical Weather Prediction -	Donald C. Norquist, M.S.
	Isidore M. Halberstam, Ph.D.
	Shu-Lin Tung, M.S.
	Chris Johnson, B.S.
	Joan-Marie Freni, B.A.
Mesoscale Forecasting -	Randy Schechter, M.S.
	Charles F. Ivaldi, Jr., B.S.
	Michael E. Niedzielski, B.S.
	James H. Willand
Boundary Layer Meteorology -	Joan M. Ward, B.A.
	Joan-Marie Freni, B.A.
	James H. Willand
	Clyde L. Lawrance
	Leo F. Rockwood

Radar Meteorology	- F. Ian Harris, Ph.D.
	Glenn R. Smythe, M.S.
	James G. Wieler, M.S.
	Steven B. Alejandro, M.S.
	Frank H. Ruggiero, M.S.
	Ralph J. Donaldson, Jr., S.M.
	Alison L. Godfrey, B.S.
Satellite Meteorology	- Michael K. Niedzielski, B.S.
	Gary B. Gustafson, B.S.
	Randy Schechter, M.S.
	Charles F. Ivaldi, Jr., B.S.
	Barry A. Mareiro
	D. Keith Roberts
	Pao-Huo Kuo
Climatology	- James H. Willand
	Arthur J. Kantor, M.Ed.

Principal Investigator was Alan M. Gerlach, Ph.D.

Subcontracts with Harris Corporation Computer Systems Division and Perkin-Elmer Customer Service Division provided on-site maintenance services for the McIDAS and Weather Radar Data Processing System, respectively.

Reports were prepared by the scientists, engineers, and mathematicians identified in the Table of Contents.

Accession For

NTIS GPA&I ✓
DTIC TAB ☐
Unannounced ☐
Justification

By
Distribution/
Availability Codes

Dist | Avail and/or Special

A-1

4

TABLE OF CONTENTS

I. NUMERICAL WEATHER PREDICTION

A. Global Data Analysis Experiment

Two objective analysis methods were developed concurrently by SASC meteorologists for implementation with the Air Force Geophysics Laboratory (AFGL) global spectral model. These methods and the results of a joint numerical experiment to test their worthiness are detailed in Halberstam et al. (1984).[1] The following is a brief summary of the methods and their products, along with later results not included in Halberstam et al. (1984).

The two analysis techniques were an optimum interpolation (OI) procedure based on the work of Bergman (1979)[2] and a fitting procedure based on the work of Halberstam and Tung (1984).[3] Both of these methods were also discussed in Gerlach (1983).[4]

1. Optimum Interpolation Procedure

The OI procedure developed for AFGL, designated the AFGL Statistical Analysis Programs (ASAP), was modified to accelerate procedures for cross-validation of the observations as well as to enhance the geostrophy in the height-wind analysis. ASAP OI codes were designed to take several different types of observations and interpolate them to a regular grid with coincident forecast values from the AFGL global spectral model (GSM) serving as a background, or "first guess," field. In both the surface pressure and upper air OI codes, the first guess fields in spectral form

---

1. Halberstam, I. M., C. Johnson, D. C. Norquist, and S.-L. Tung, 1984: **Two Methods of Global Data Assimilation**. AFGL-TR-84-0260, Contract F19628-82-C-0023, Systems and Applied Sciences Corporation.

2. Bergman, K. H., 1979: Multivariate analysis of temperature and winds using optimum interpolation. **Mon. Wea. Rev.**, 107, 1423-1444.

3. Halberstam, I. M., and S.-L. Tung, 1984: Objective analysis using Hough vectors evaluated at irregularly spaced locations. **Mon. Wea. Rev.**, 112, 1804-1817.

4. Gerlach, A. M., ed., 1983: **Objective Analysis and Prediction Techniques - 1983**. AFGL-TR-83-0333, Contract F19628-82-C-0023, Systems and Applied Sciences Corporation, ADA142441.

are evaluated at observation sites after observations are interpolated to model sigma layers; then observation-minus-first guess residuals are formed. These residuals are then interpolated to the grid locations using the OI procedure and added to the gridded first guess values to form the analysis.

In the experiments, this analysis was initialized with the Machenhauer non-linear normal mode initialization (NMI) procedure. Another forecast was then run from the initialized field to generate a first guess for the next period. The surface pressure analysis provided an analysis of pressure on the model terrain using pressure univariately over land and equatorward of 20° latitude, and multivariately elsewhere with zonal and meridional surface wind observations assuming geostrophy and correcting for frictional effects. The upper air analysis multivariately analyzes heights and winds on sigma layers, although height residuals exist at sigma levels (layer interfaces).

Ten data assimilation cycles using 12 h forecasts were conducted with FGGE II-B[5] observations for 7 Jan 79, 12 GMT through 12 Jan 79, 00 GMT. The procedure started with a 12 h forecast from a FGGE III-A analysis for 7 Jan 79, 00 GMT, truncated to rhomboidal 30 wave resolution on 12 sigma layers. In addition, a 48 h GSM forecast was run from the ASAP analysis for 9 Jan 79, 00 GMT and from the FGGE III-A analysis for the same time for comparison. Three general conclusions were drawn from the results: (1) the fast gravity mode component of the analysis was less than the slow mode component for winds and heights at most model layers, and this ratio tended to increase with altitude for heights. The value of analysis fast mode was greater than the slow mode for the surface pressure analysis. (2) RMS differences when compared with observations were similar to differences between observations and FGGE III-A for heights and somewhat higher for winds and specific humidity, a favorable result in view of the fact that FGGE III-A analyses are based on 6 h forecasts. (3) RMS errors

5. Obtained from Department of the Air Force, OL-A, USAF Environmental Technical Applications Center (MAC), Federal Building, Asheville, NC 28801.

against observations at the 48 h forecast were somewhat higher for the ASAP based forecast than for the FGGE III-A based forecast, but the error growth rate during the forecast for some variables (especially upper level winds) was lower for the ASAP case.

2. Fitting Procedure

The fitting procedure attempted to combine aspects of initialization with objective analysis by using the linear normal mode functions (nmf) of the model as the fitting functions. The nmf would then be the medium by which the data in the form of residuals would be interpolated to the grid points. It was also assumed that by iterating between analysis and initialization the analysis could accurately reflect both the data and the "slow" mode, i.e., the large scale atmospheric structure. Experiments involving analyses with and without iterations were conducted and their results compared.

The analysis procedure, similar to ASAP, begins with a vertical optimum interpolation of data to the sigma layers. Residuals are computed by expansion of the first guess spectral coefficients at the observation sites and their subtraction from the observations. At this point the fitting procedure diverges from ASAP. The residuals are converted from wind and temperature differences to wind and height differences by invoking the Sela hydrostatic equation.[6] Surface pressure residuals are calculated by interpolation or extrapolation of the height residuals near the surface. Where observations are missing in the vertical, zero residuals are used in their stead. In grid boxes where no observations are present, zero residuals are inserted at the four corners of the grid box.

The residuals are then projected onto the vertical modes of the nmf. This presents no difficulty because the vertical modes are orthogonal to known vectors defined with respect to the sigma structure of the model, which has been preserved by the vertical interpolation of the observations to the sigma layers. The coefficients of the vertical modes are then fit

---

6. Sela, J., 1980: Spectral modeling at the National Meteorological Center. Mon. Wea. Rev., 108, 1279-1292.

to the horizontal nmf by sequential estimation of each mode's contribu-
tion. The vector containing the data that are to be fit to the nmf is
scalar multiplied by a vector containing the nmf with the lowest zonal and
frequency indices evaluated at all the observation sites. The result
defines a coefficient of the first nmf vector. The coefficient times this
vector is a first estimate of the data vector; this estimate is subtracted
from the data vector. The remainder is then fit to the second nmf vector
in the same manner and its estimate subtracted from the remainder, and so
on. What results is a set of coefficients, derived sequentially, which,
when multiplied by their respective nmf vectors, produce an estimate to the
data vector. This estimate can be interpolated to the grid points by
simply evaluating the nmf at the grid points. Once the grid values are
known, surface pressure and heights can be derived from the nmf. Temp-
eratures are then computed by a least-squares fit to the heights as pro-
posed by Flattery (see Halberstam et al., 1984[1], Appendix A). These
analyzed residuals can now be added to the first guess field on the grid,
resulting in an updated analysis. This analysis is subjected to the
Machenhauer NMI to reduce the tendencies of the gravity waves to near
zero. The initialized field can then be used to produce a forecast or can
be substituted as a new first guess field to produce new residuals for a
second iteration of the analysis procedure.

This analysis procedure was tested in a forecast-analysis cycle
similar to the ASAP test but was limited to five 12 h periods without
iteration. An analysis with three iterations was produced for 7 Jan 79 at
12 GMT and a 12 h forecast produced, based on the final analysis. Results
showed that errors grew substantially between cycles and that the iterative
procedure tended to diverge. This was initially blamed on the Flattery
fitting technique which tended to exaggerate the upper level temperatures
because of an extrapolation performed at the highest level. Indeed, the
errors seemed to propagate downward as time progressed. In a second round
of experiments, the highest layer temperatures were replaced by first guess
values after the analysis. This tended to reduce the errors somewhat but
did not completely halt the growth of error with time. It also failed to
reverse the divergence of the iterative procedure. Although the experiment
has been completed, it is now felt that the first guess field was weighted

too heavily in the analysis because of the large number of zero residuals and the lack of statistical weights for observed and forecast values. To discover the true cause, however, would require additional testing and careful analysis of the results.

B. Improved Moisture Optimum Interpolation Analysis

A major goal of the AFGL Atmospheric Sciences Division is to develop a global cloud forecasting capability. To achieve this capability, efforts are being carried out both in the global forecast model and in the specification of the initial distribution of moisture for the model. This section discusses work undertaken by SASC to specify more accurately the moisture initial conditions by modifying the moisture analysis section of the AFGL Statistical Analysis Program (ASAP) optimum interpolation procedure.

The methodology used in producing an analysis of specific humidity for the forecast model in the current version of ASAP is discussed in Gerlach (1983).[4] The ASAP experiment described in Halberstam et al. (1984)[1] focuses on the analysis of mass and motion variables, with only a passing reference to moisture. The current effort centers on improving the fit of the moisture analysis to the observations. In the case of the mass and motion analysis, the fitting emphasis has to be balanced with the ability of the analysis procedure to maximize the introduction of slow component correction to the first guess from the observations while minimizing the contribution to the analyzed fields of the spurious fast gravity mode. Since, however, the concept of a balanced field is irrelevant in moisture distribution, the improvement of the moisture analysis can be placed solely on the generation of analyzed moisture fields that are more representative of the observed values. However, another problem arises in the case of moisture: the relative lack of high quality direct observations. The only form of direct, high quality observation of upper air moisture is the rawinsonde, with an observation error judged to be about ± 5 percent relative humidity (Gustafsson, 1981).[7] Layer precipitable water measurements by satellites are thought to be somewhat

_____

7. Gustafsson, N., 1981: A review of methods for objective analysis. Dynamic Meteorology: Data Assimilation Methods, Vol. 36, Applied Mathematical Sciences Series, L. Bengtsson, M. Ghil, and E. Kallen, eds., Springer-Verlag, 330 pp.

13

less accurate, with error estimates ranging from 20 percent to 40 percent error in relative humidity. Besides these two methods of direct measures, moisture profiles have been inferred from surface weather observations and cloud analysis algorithms, such as the 3DNEPH procedure of the Air Force Global Weather Central (AFGWC).

The current version of the ASAP OI moisture analysis procedure uses only rawinsonde observations, and when available, satellite layer precipitable water observations. Plans are being made to introduce a lesser weighted representation of the inferred values from surface observations and cloud analyses in areas where no direct observation is available. In addition, the present codes will be modified to perform the analysis in relative humidity instead of specific humidity.

Two investigations relating to the moisture analysis project have been completed. They are: (1) a study of the use of the Kurihara "equal area" (EA) grid instead of the analysis transform grid on which to calculate the analyzed residuals, and (2) a study of the proper form of moisture to be used in the vertical interpolation of moisture from observation levels to sigma layers to minimize interpolation errors. In the first study analyzed residuals on the EA grid were expanded in 30 wave rhomboidal spectral coefficients, then the spectral functions were evaluated back on the EA grid locations. For almost all variables at all levels, the difference between the final values and original values was about 10 percent of the full analyzed residual values. Since this error level was considered excessive in comparison to observational errors, the analysis transform grid was retained as the analysis grid. Regarding the vertical interpolation of moisture, profiles of zonally averaged rawinsonde observations of moisture were plotted for global observations from the months of February and June. The curves were for various forms and functions of moisture vs. various functions of pressure to see which combination would yield the smallest RMS difference from an assumption of linear variation with the pressure function when such an assumption is used to interpolate between neighboring levels. The results showed that ln q (natural logarithm of specific humidity) vs. ln p showed the best agreement with the assumption of linearity of all of the combinations, therefore affording the least error in a linear interpolation. For this reason, the linear ln q vs. ln p interpolation will be employed in the ASAP OI scheme.

14

The newly modified moisture analysis will be tested in a 6 h forecast-analysis data assimilation scheme, and results will be compared with the various forms of observations and inferred values to determine how much improvement is realized.

C. Relocatable Limited Area Model

SASC is responsible for studying regional numerical weather prediction model development and performance. The task will follow a two-pronged approach: (1) to develop and test a relocatable limited area model (RLAM) of versatile framework, using as guidelines the suggestions and recommendations of Yang and Brenner,[8] and (2) to acquire an operational model and perform tests with it as a basis of comparison with the developed model. To date, the regional model being implemented at AFGWC, which was recommended as the operational model, has not become available for implementation at AFGL. Thus, the thrust of the SASC effort so far has been the development of the RLAM. This development has made progress in two areas: (1) formulation of software for computation of necessary geographic quantities for regular grids of varying resolution and staggering on several map projections, and (2) design and some implementation of coding for horizontal and vertical finite difference schemes, with an eye on their relationship to appropriate time differencing procedures.

Developmental guidelines call for coding to allow for easy switching between a latitude-longitude grid and a Cartesian grid on any of three different map projections: polar stereographic, Mercator, or Lambert conformal. The grids, which are superimposed on these various projections, allow for regular spacing in latitude and longitude between grid points for the latitude-longitude grid, and equal spacing of map distance between grid points for the various Cartesian map projections. The objective of this stage of software development is to produce a modularized code to generate values of x (map distance from origin in left-right direction), y (map distance from origin in top of grid, bottom of grid direction), ϕ (actual latitude on earth's surface), λ (actual longitude on earth's surface), m

---

8. Private communication.

(map factor, relationship of map distance to actual earth distance), and f
(coriolis parameter, $= 2 \Omega \sin \phi$ where Ω is the angular rotation rate
of the earth in radians/second) for each grid point. The specification of
the location, spatial extent, horizontal resolution, vertical resolution,
and relative location of mass, motion, and moisture variable grid points to
allow for staggered or unstaggered grid systems should all be entered as
simple variables. Once the geographic quantities have been generated for
the selected grid, ϕ and λ values at grid points for the prognostic
variables should be used as input to generate initial values for the
prognostic variables from a global spectral representation of the fields of
these variables.

For the three Cartesian map projections, the NCAR (National Center
for Atmospheric Research) graphics routines available at AFGL were used to
produce maps containing continental outlines and latitude/longitude lines.
Whole mesh grids were then superimposed over each of the maps. These plots
are designed for the user of the RLAM to specify the indices of the grid
points that surround the area of the forecast to be generated. FORTRAN
subroutines which take as input these indices, as well as the choice of map
projection, horizontal resolution, and type of horizontal staggering, have
been successfully formulated for the three Cartesian map projections.
These codes then generate the x, y, λ, ϕ, m, f values for each prog-
nostic variable's grid under the specified conditions. Coding to use the
generated grid point ϕ, λ to evaluate spectral forms of the prognostic
variables for initial values is underway. The subroutine for generating
the values of ϕ, λ, m, f for the latitude-longitude grid, including
horizontal staggering, has been designed and will be implemented soon.

Emphasis in the RLAM development is being placed on designing the
model in modular form so that various components can be easily replaced.
This means that routines dealing with horizontal differencing, vertical
differencing, time stepping, physical processes, initialization, and other
specific functions are required to remain independent of each other. The
reason for this is to achieve the greatest degree of interchangeability so
that various combinations of functions can be used in model sensitivity
tests.

As a starting point, a particular choice of horizontal, vertical, and time differencing schemes was made as a framework for the model. This test model contains the primitive, dry adiabatic equations without friction. Numerical schemes chosen are a compact fourth order horizontal differencing scheme and the Brown-Campana time differencing scheme. There are 12 layers in the vertical with the vertical coordinate $\sigma = p/p_s$ defined in each layer in the same way as in the AFGL global spectral model (Brenner et al., 1982).[9] The horizontal resolution is comparable to the whole mesh spacing at the Air Force Global Weather Central (Hoke et al., 1981).[10] Even with such a simple model, however, modularity is not easily achieved. It is very difficult to separate the numerical schemes from the other components of the model without trivializing the main programs. A decision on whether variables should appear on a staggered grid or not, for example, affects the way in which certain terms are calculated. Thus, while it is feasible to design a grid that can allow for both unstaggered and staggered specifications, it is not possible to anticipate what effect different types of staggering will have on various differencing schemes. It is also true that different time stepping routines demand that certain terms be calculated in specific ways in order to insure stability. But that makes it difficult to generalize a time differencing scheme without taking the horizontal differencing into account. In short, it was necessary to forego the modularity of the differencing schemes for this test model in order to maintain separateness in the calculation of the other terms of the equations. As this model is tested, further modifications will be attempted to blend modularity and separateness of calculation.

---

9. Brenner, S., C. H. Yang, and S. Y. K. Yee, 1982: The AFGL Spectral Model of the Moist Global Atmosphere: Documentation of the Baseline Version. AFGL-TR-82-0393, Air Force Geophysics Laboratory, Hanscom AFB, MA, ADA129283.

10. Hoke, J. E., J. L. Hayes, and L. G. Renniger, 1981: Map Projections and Grid Systems for Meteorological Applications. AFGWC/TN-79/003, U. S. Air Force, Air Weather Service (MAC), Air Force Global Weather Central, Offutt AFB, NE.

The test model has been coded in two forms, each with its own perspective on modularity. The first computes the various types of terms (horizontal advection, vertical advection, pressure gradient, etc.) of the equations in separate subroutines. Differencing schemes are built into these subroutines, which would have to be completely replaced if a different scheme were to be selected. The second method computes the actual terms of the equation in the main program, but the derivations or averages whose products or quotients make up those terms are calculated in individual subroutines depending on type of derivative or average. For the advective terms, for example, a subroutine would find the x and y derivatives of the advected variable while another would find the averaged wind components multiplying the derivatives. The first of the two methods has the advantage of compactness and is highly readable as code, but is not as modular. The second allows for greater interchangeability of units but is less readable. Tests will be conducted to determine which approach is more practical.

In order to step ahead in time to test the Brown-Campana scheme, boundary values for each time step will be supplied from the global spectral model on boundary grid points. At this point, the test model will be complete, and an effort to maximize modularity and generality for staggered and unstaggered grids will be undertaken. Attempts will be made to add other time differencing schemes as modules, and a quasi-Lagrangian approach to the combined space and time differencing problem will be formulated as a separate module. These will all be built into the code containing the calculation of geographical and initial values for the choice of map projection and area of forecast. Meanwhile, the operational model acquired from AFGWC will be brought online and prepared for parallel adiabatic tests with the RLAM in its various stages of development.

II. MESOSCALE FORECASTING

A. An Error Analysis of LFM-II Forecasts During Winter Seasons

1. Introduction

An error analysis was performed on Limited Area Fine Mesh Model (LFM-II) forecasts for the 1983-84 cool season similar to the analysis conducted for the 1982-83 winter.[11] As in the original study an examination of systematic errors in forecasts made by the LFM-II was performed by summing individual forecast errors over the period of study (1 Oct 83 - 30 Apr 84) and computing average errors.

Individual forecast errors from 89 stations were obtained from the FOUS 60-78 bulletins decoded by McIDAS. Forecast values for each variable at each station for 12, 24, 36, and 48 h forecasts were obtained from the appropriate location in the FOUS 60-78 bulletin. Verification values were obtained from the initial conditions in the relevant successive FOUS 60-78 bulletins that were derived from the LFM-II initial analysis. Forecast errors of the variables were accumulated at each of the 89 locations by subtracting the verification value from a variable forecast value. The variables analyzed included sea level pressure, 1000-500 mb thickness, mean relative humidity, boundary layer relative humidity, and boundary layer temperature. By calculating the forecast errors in the manner described, a positive number indicated an overforecast (i.e., the forecast was too warm, too moist, pressure too high, etc.) and a negative number indicated an underforecast (too cold, too dry, pressure too low, etc.).

To examine the sensitivity of the forecast errors to diurnal influences, the data at each of the 89 stations were stratified into error sums from 00 GMT model runs and 12 GMT model runs. Table 1 displays the total number of forecast sets making up the final sums of the forecast errors along with the percentage of possible forecasts available during the test period. For a more complete description of the methodology employed in this study, see Gerlach (1983).[4]

---

11. Schechter, R., 1984: An error analysis of LFM-II forecasts during the 1982-1983 winter season. Bull. Amer. Met. Soc., 65, 1073-1080.

TABLE 1.   NUMBER OF FORECASTS USED TO CALCULATE AVERAGE LFM-II VARIABLE
            FORECAST ERRORS

	00 GMT	12 GMT
12 hour forecasts	153 (72%)	154 (72%)
24 hour forecasts	134 (63%)	170 (80%)
36 hour forecasts	145 (68%)	147 (69%)
48 hour forecasts	127 (60%)	164 (77%)

2. Results

In general the systematic errors found in LFM-II forecasts for 1983–84 (Figs. 1–10) are very similar to the errors found in the 1982–83 study (see Gerlach 1983,[4] pp. 62–73). Sea level pressure (Figs. 1 and 2) is, on average, forecast too high west of the Rockies and too low east of the Rockies. The magnitudes of the errors show some tendency to grow with forecast length although the positive errors for the 48 h forecasts at both 00 and 12 GMT are smaller than those for 36 h forecasts.

Figs. 3 and 4 show the results of the error analysis for 1000–500 mb thickness in meters at 00 and 12 GMT respectively. Positive errors are seen east of the Rockies with the exception of some small negative errors for certain forecast periods in eastern New England. The largest positive errors occur at the 12 GMT verification times (12 and 36 h forecasts from the 00 GMT initial time and 24 and 48 h forecasts from the 12 GMT initial time). Negative errors are found mostly in the southwestern United States except for the 12 h forecast from the 00 GMT runs. Maximum negative errors occur at the 00 GMT verification time (i.e., 24 and 48 h forecasts from 00 GMT model runs and 12 and 36 h forecasts from 12 GMT model runs).

Layer mean relative humidity in the LFM-II (approximately 1000–490 mb) is forecast too moist in the Rockies (Figs. 5 and 6) particularly in the vicinity of western Montana. The model in general is too dry along the Gulf Coast with the largest dry bias occurring in southern Florida. The moist errors tend to be largest at the 00 GMT verification time while no strong diurnal variation is apparent for areas that have a dry bias.

Fig. 1. Average LFM Forecast Sea Level Pressure Error (tenths of mb) from 00 GMT Model Runs: (a) 12 h Forecasts; (b) 24 h Forecasts; (c) 36 h Forecasts; (d) 48 h Forecasts

Fig. 2. Same as Fig. 1 Except 12 GMT Model Runs
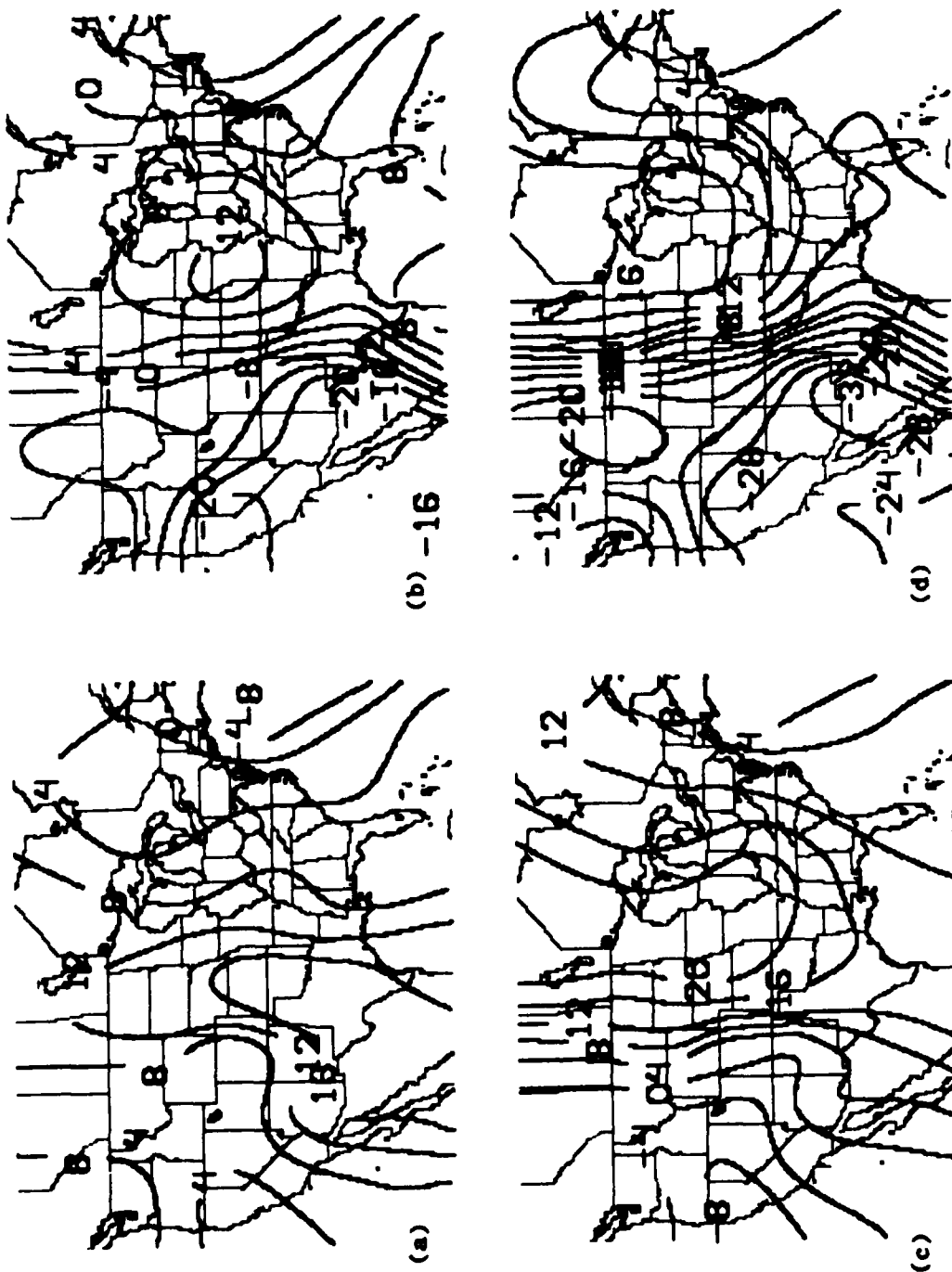
Fig. 3. Average LFM Forecast 1000-500 mb Thickness Error (meters) from 00 GMT
Model Runs: (a) 12 h Forecasts; (b) 24 h Forecasts; (c) 36 h Forecasts;
(d) 48 h Forecasts

Fig. 4. Same as Fig. 3 Except 12 GMT Model Runs

Fig. 5. Average LFM Forecast Mean Relative Humidity Error (whole percent) from 00
GMT Model Runs: (a) 12 h Forecasts; (b) 24 h Forecasts; (c) 36 h
Forecasts; (d) 48 h Forecasts

25

Fig. 6. Same as Fig. 5 Except 12 GMT Model Runs

A pervasive dry bias is noticeable in the average errors for boundary layer (lowest 50 mb) relative humidity (Figs. 7 and 8). Exceptions are the 12 h forecasts from the 12 GMT runs and the Rocky Mountains for forecasts that verify at 00 GMT. Unlike the layer mean relative humidity errors (Figs. 5 and 6) the largest dry bias for boundary layer relative humidity occurs on the Texas and Louisiana side of the Gulf of Mexico.

Forecasts of boundary layer temperature (Figs. 9 and 10) are too warm along the Gulf Coast especially in southern Florida and, with the exceptions of the 12 h and 36 h forecasts from the 00 GMT model runs, too cold in the Great Lakes region. As with most of the other error fields a distinct difference can be discerned in the biases between the two model initial times. The largest warm biases occur at the 12 GMT verification time and the largest cold biases (or reduced warm biases) occur at the 00 GMT verification time.

3. Discussion

As previously stated the analyzed error fields from the 1983-84 cool season generally exhibit the same patterns as were found for the biases in the 1982-83 winter season. Note however that some differences do exist. Errors for sea level pressure in the 1983-84 study are generally smaller and the negative errors are found further south (see Figs. 1 and 2). An hypothesis was presented in the earlier report (Gerlach, 1983,[4] p. 76) that attributed the location of the maximum positive sea level pressure errors in the southwestern United States to a "large southern displacement of the jet stream during much of the 1982-83 winter." Since the error pattern was basically the same for 1983-84 (particularly the location of the error centers) and the jet stream in 1983-84 was not similarly displaced southward, the hypothesis must be rejected. Apparently the location of the positive sea level pressure errors is determined by other (unknown) factors.

The magnitude of the 1000-500 mb thickness errors in 1983-84 is generally larger than in 1982-83, particularly in areas that show a negative bias. For layer mean relative humidity the errors in the present study show a larger dry bias, i.e., the positive (moist) errors tend to be smaller while the negative errors tend to be larger. Errors in boundary layer relative humidity are virtually identical for both years. The same

27
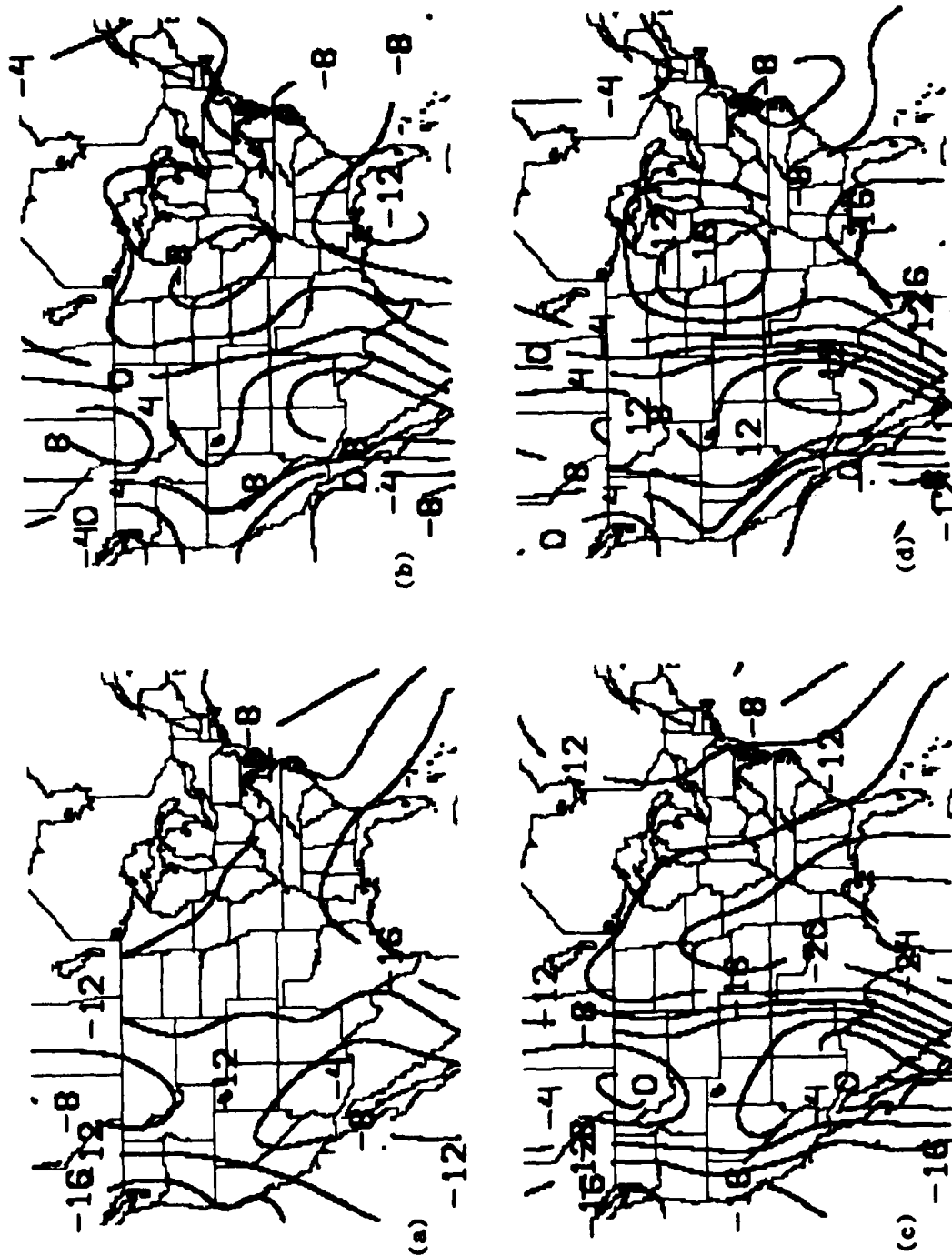
Fig. 7. Average LFM Forecast Boundary Layer Relative Humidity Error (whole percent) from 00 GMT Model Runs: (a) 12 h Forecasts; (b) 24 h Forecasts; (c) 36 h Forecasts; (d) 48 h Forecasts
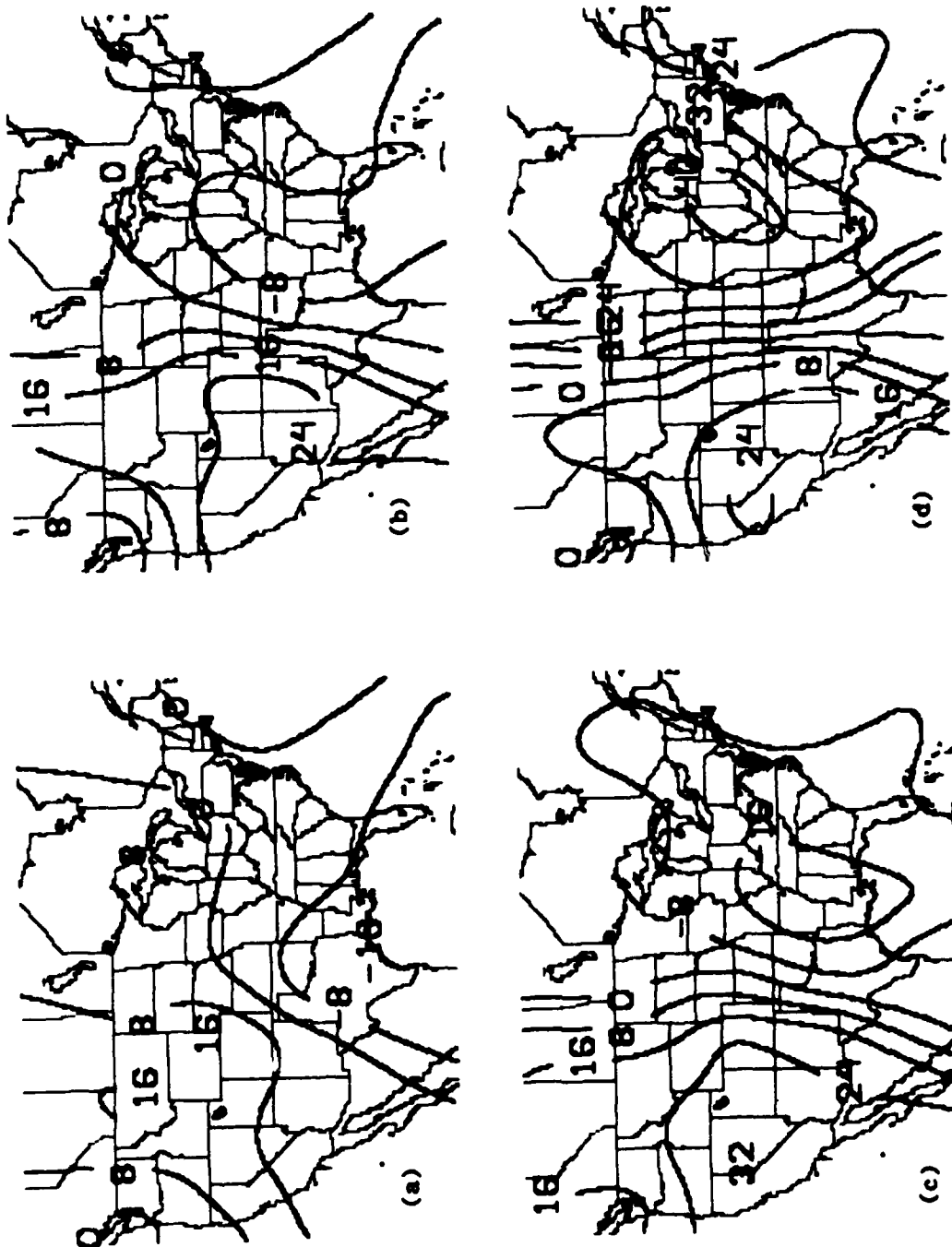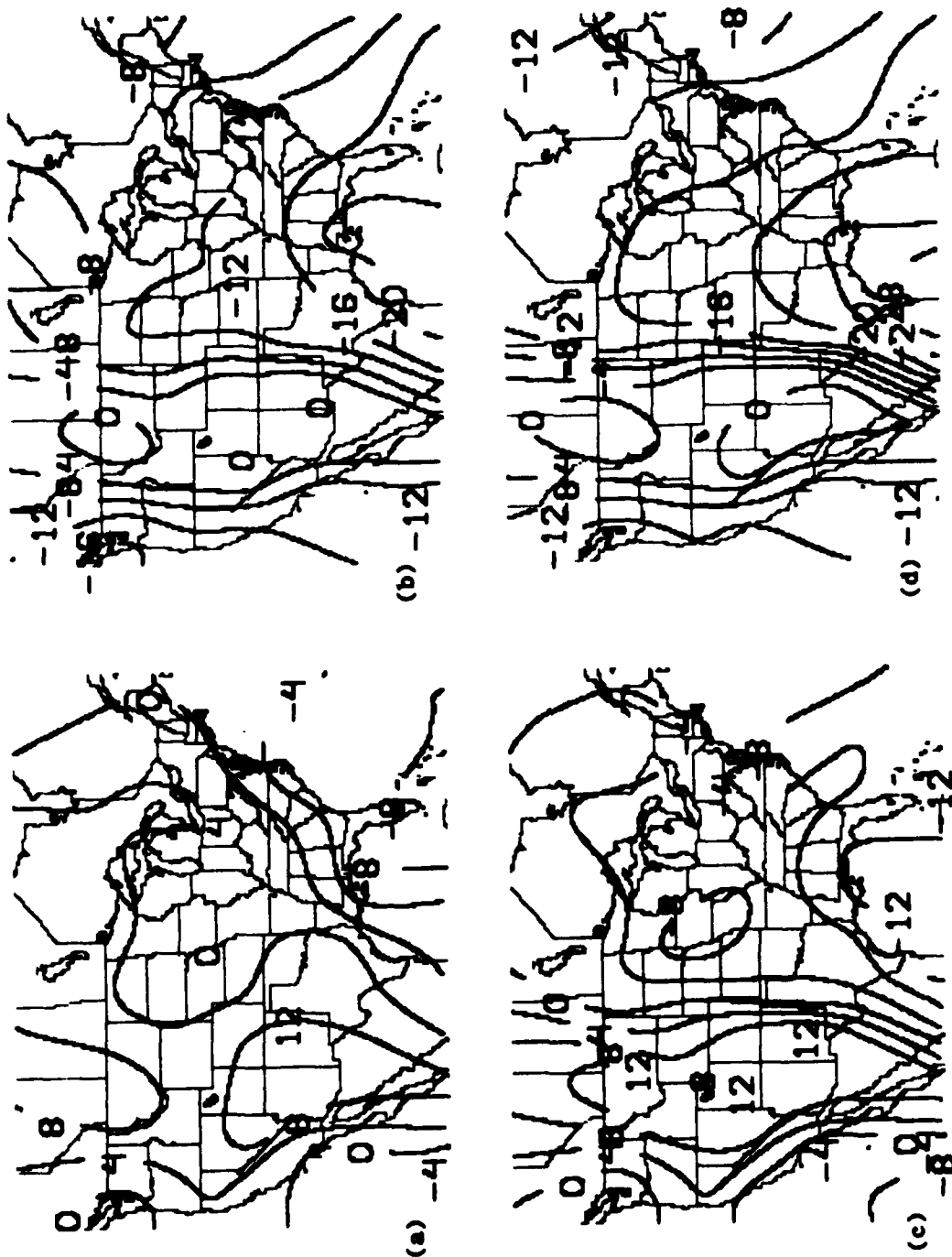
Fig. 8. Same as Fig. 7 Except 12 GMT Model Runs

29
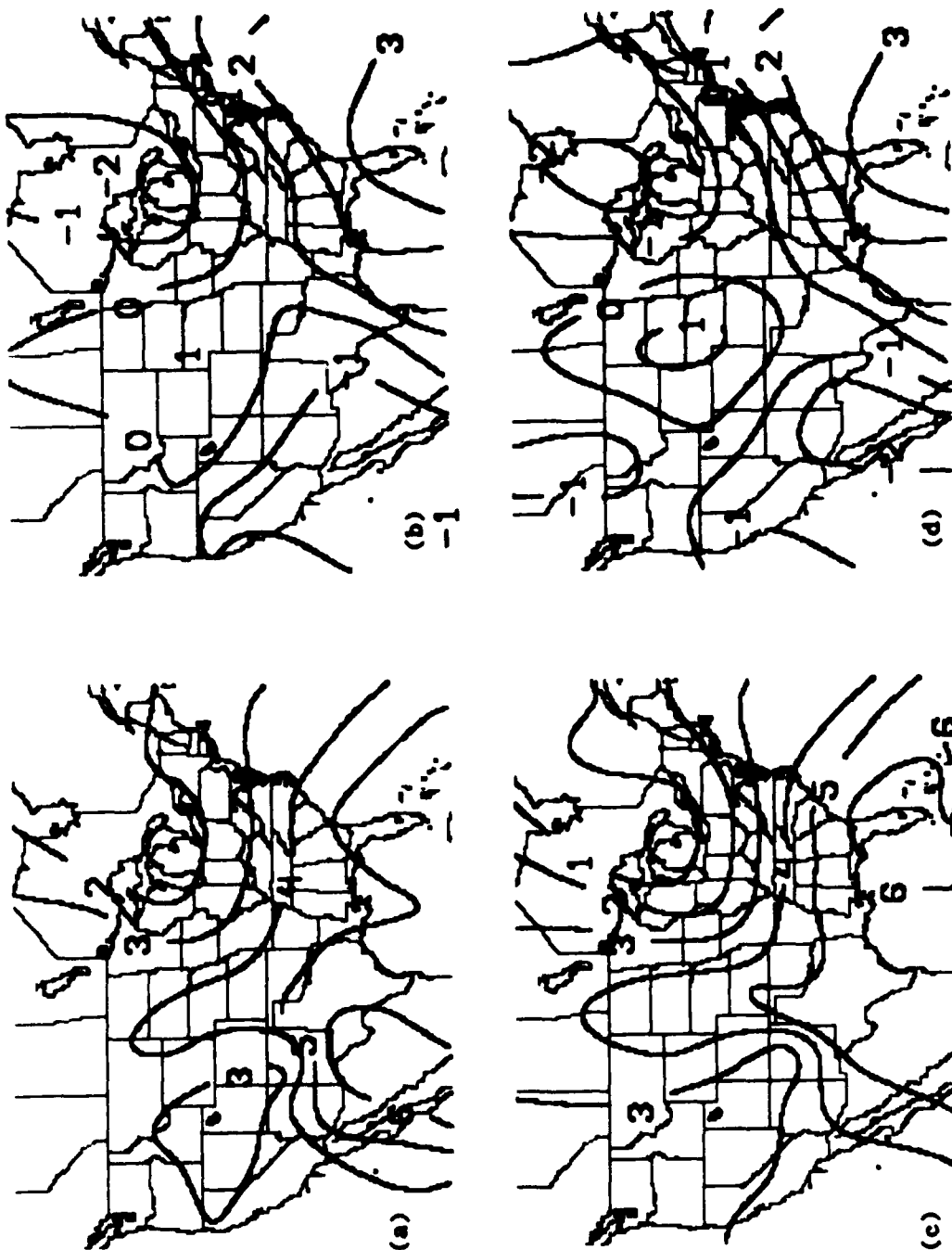
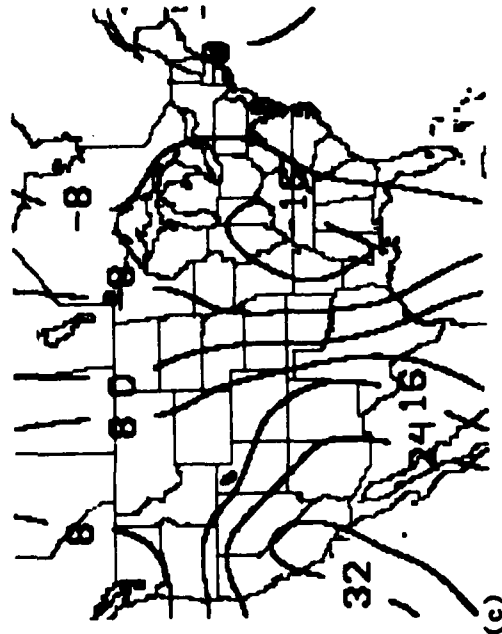Fig. 9. Average LFM Forecast Boundary Layer Temperature Error (°K) from 00 GMT Model Runs: (a) 12 h Forecasts; (b) 24 h Forecasts; (c) 36 h Forecasts; (d) 48 h Forecasts
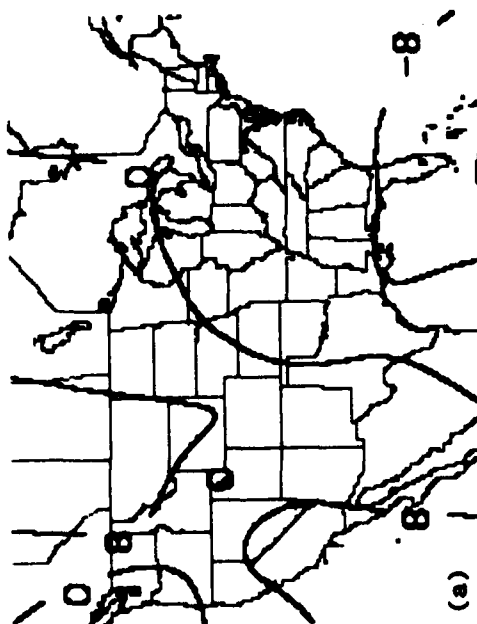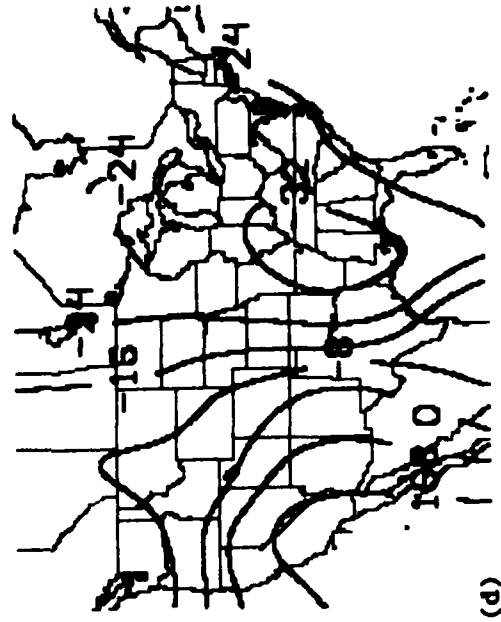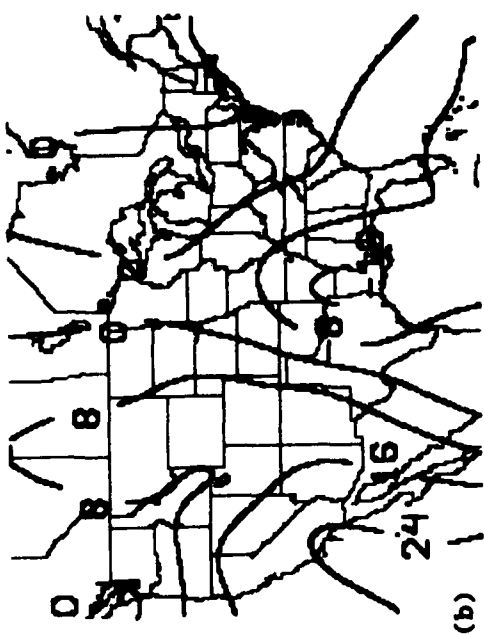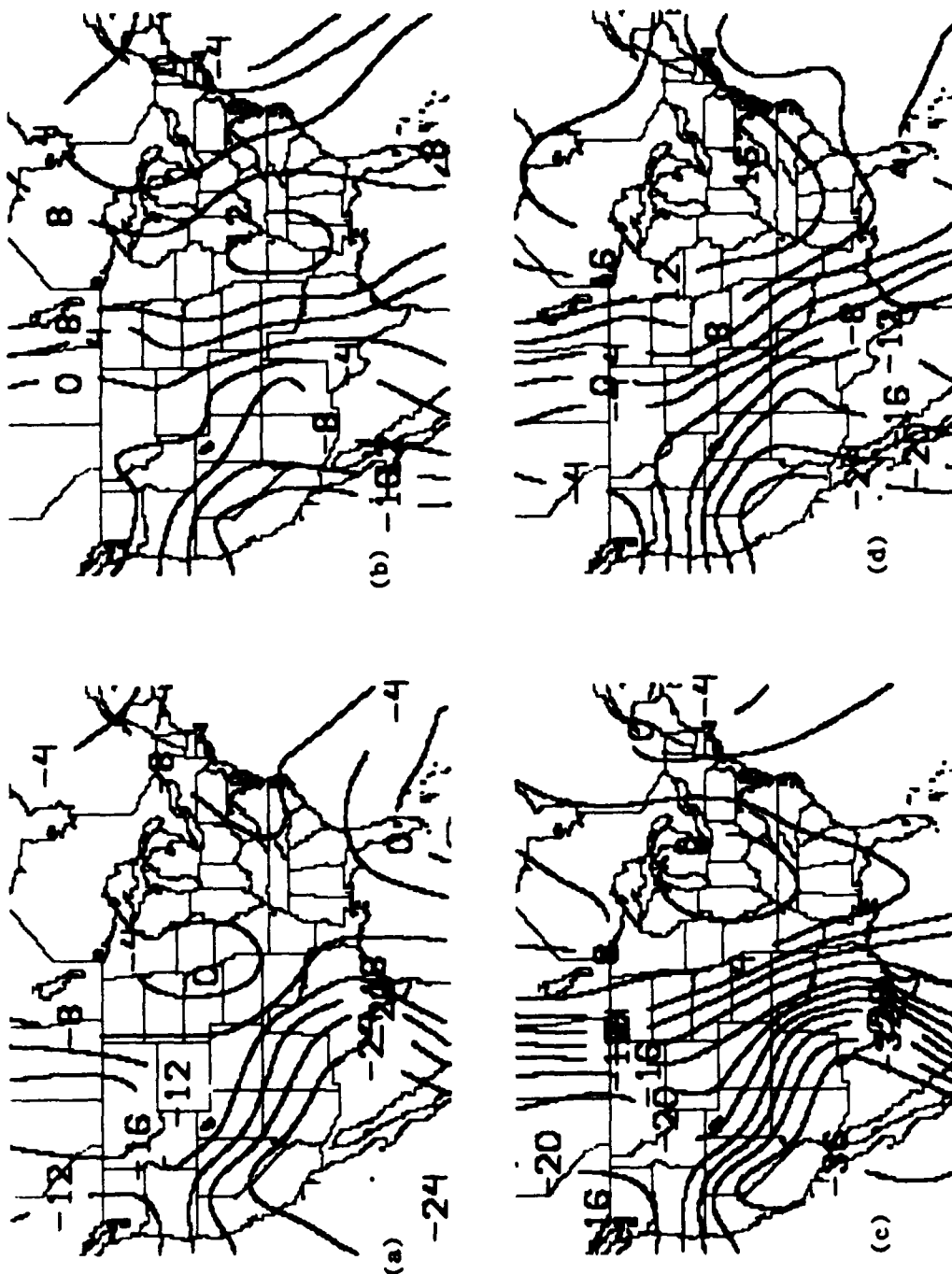
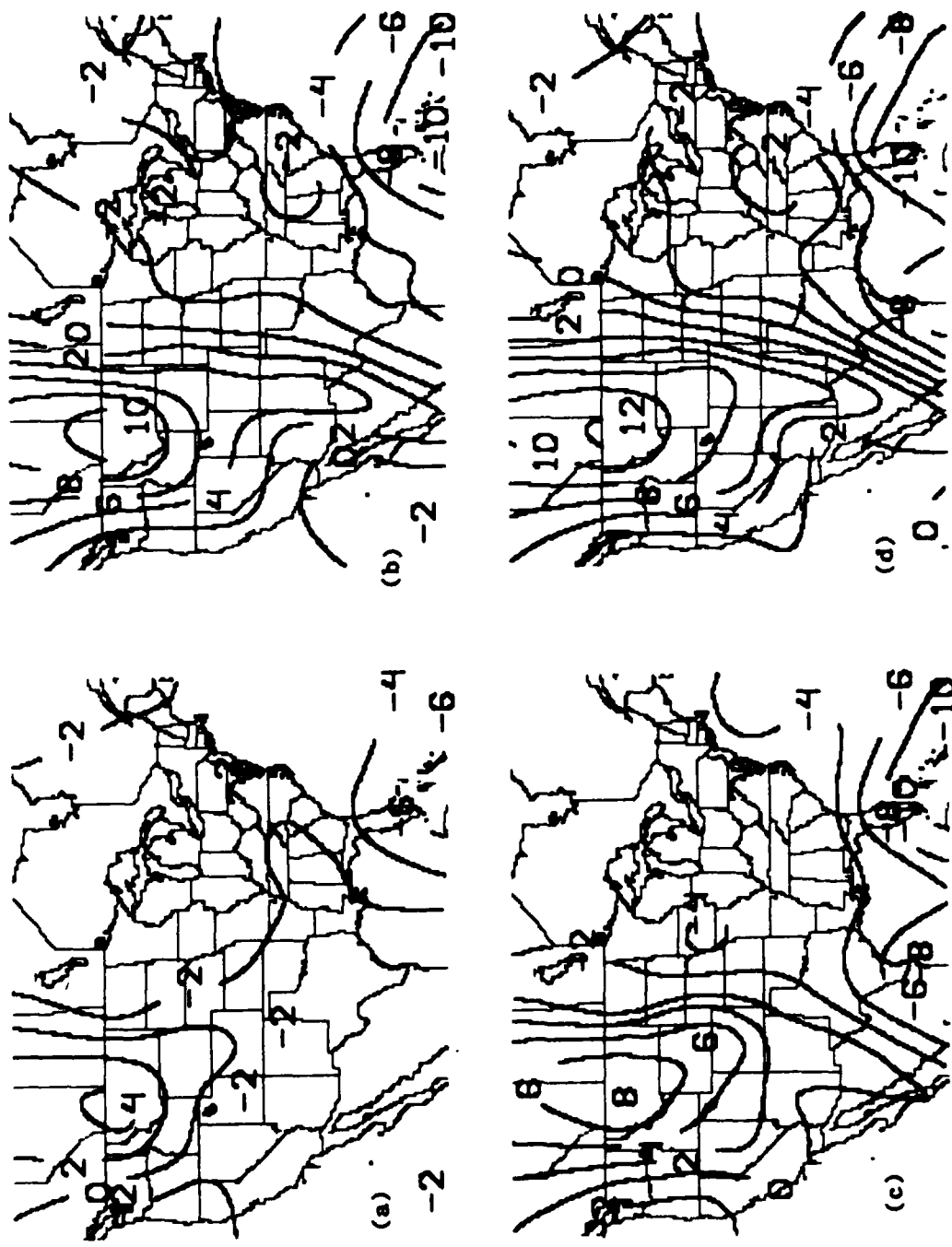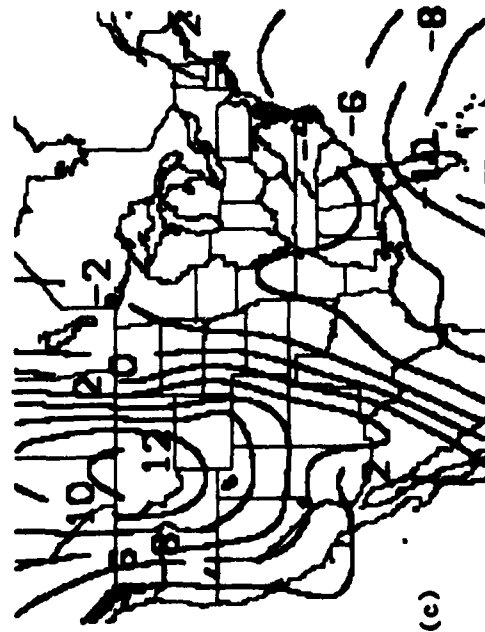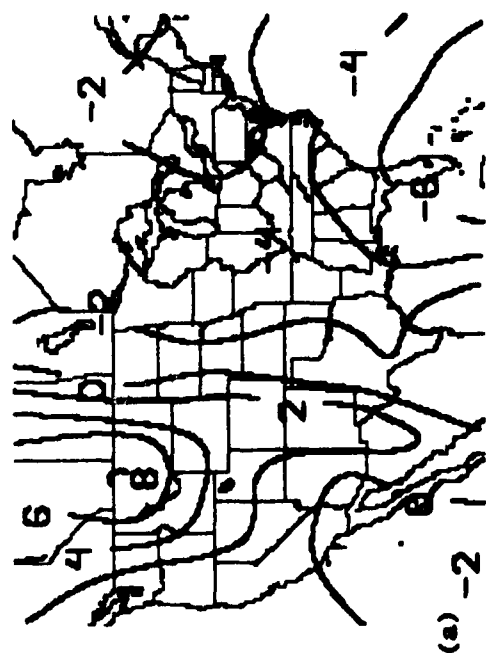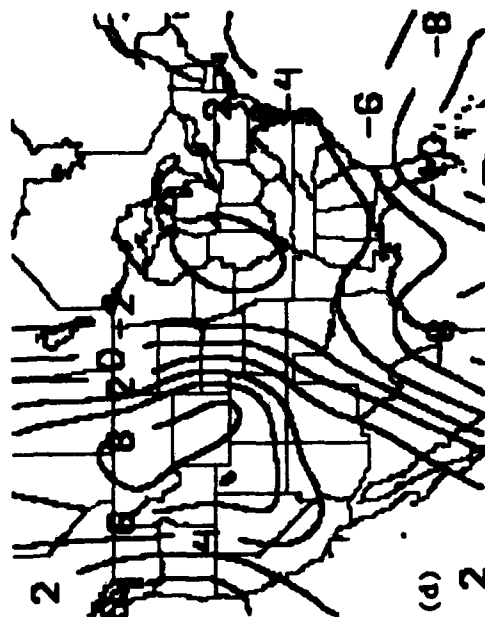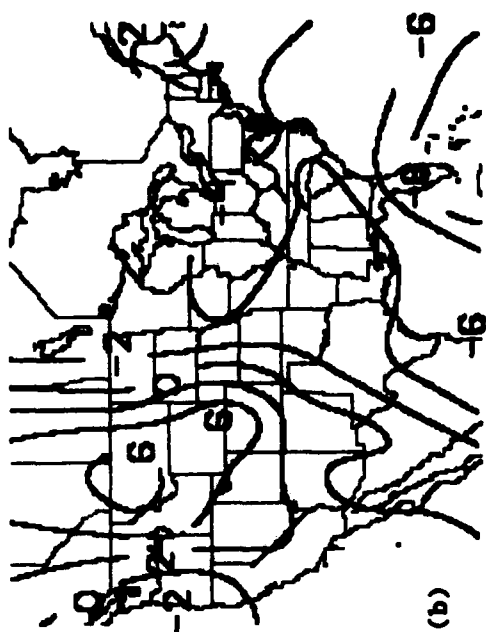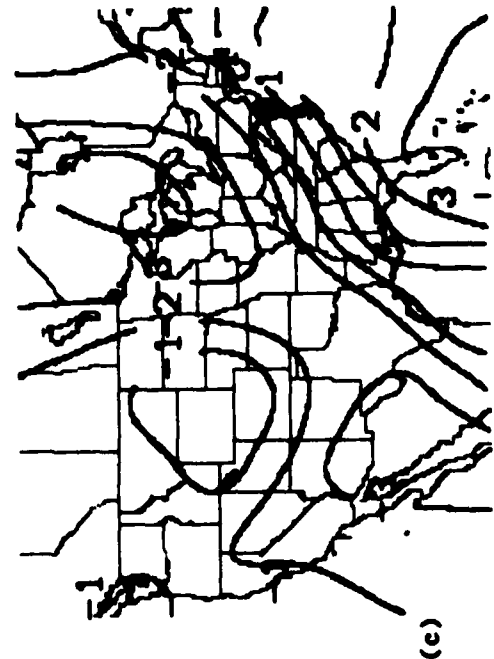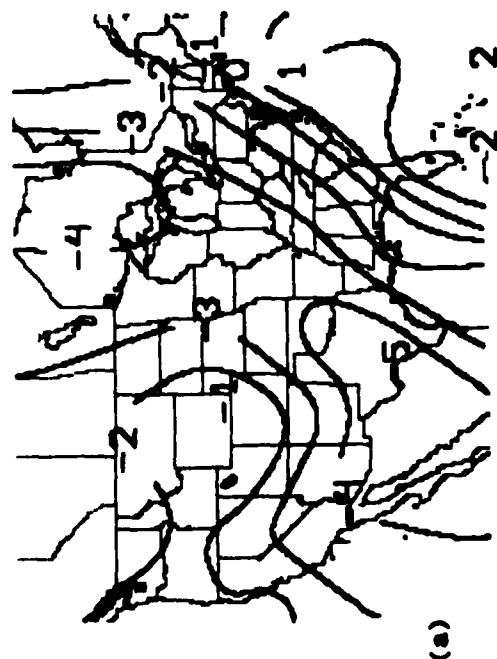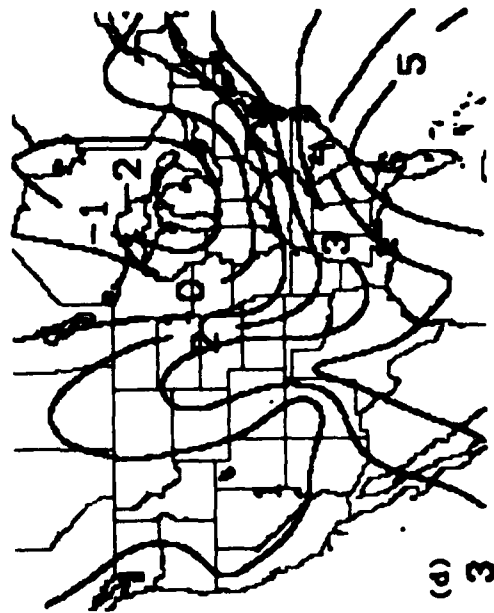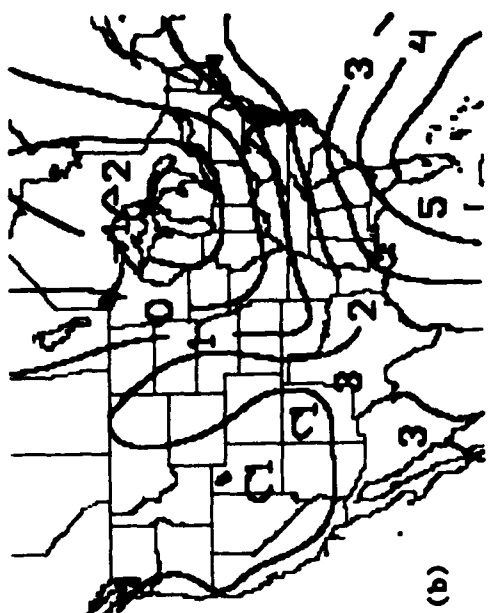Fig. 10. Same as Fig. 9 Except 12 GMT Model Runs

can be said for boundary layer temperature except that at 48 h the negative errors in the Great Lakes are smaller for both 00 GMT and 12 GMT forecasts in 1983-84.

The average errors from 1983-84 were stratified by month (12 GMT forecasts only) to see if the error patterns change coherently over the course of the cool season. Negative sea level pressure errors are relatively small in October, increase to a maximum in December, and then decrease. Positive sea level pressure errors are small in October through January (almost entirely absent in December), then increase slowly through April.

Positive 1000-500 mb thickness errors in the eastern United States tend to increase to a December maximum and then fall off. The moist bias in mean relative humidity found in the Rockies increases in the fall and early winter, peaking in February, and then declines. The monthly stratification for boundary layer temperature reveals no obvious trends but the largest north-south temperature gradient occurs in December. December is also the month when most of the variables investigated show the largest absolute errors and the time when the difference between the positive biases and negative biases is greatest.

The stratification of the forecast errors by month did not offer as much insight into the causes of the biases as had been hoped. Few coherent trends could be found for most of the variables; in fact, no obvious seasonal variations are apparent for boundary layer temperature or boundary layer relative humidity. Another possible way of stratifying the forecast errors is by flow regime. An effort is under way to reanalyze the data from the 1983-84 cool season using discrete 500 mb flow pattern categories. The major problem is the difficulty in developing a method to classify the flow patterns objectively. It may turn out that a more subjective approach will be resorted to.

The similarity of the bias patterns for the two winter seasons examined suggested that it might be possible to develop a forecast correction technique. The goal of the technique would be, using the identified error characteristics, to adjust the model forecasts with the objective of reducing the forecast errors. Such a technique was devised using 12 GMT forecasts from the 1983-84 cool season to test the feasibility of the concept.

The first step in the procedure was to generate a correction factor for each station, variable, and forecast interval. This was accomplished by using the 10 most recent model runs (an independent set of factors was calculated for 00 GMT and 12 GMT forecasts) and determining the average error over this interval. The correction factors were constantly updated by including the newest forecast in the average and removing the oldest forecast. Using 10 forecasts to determine the correction factor was arbitrary but it was felt that this length of time was long enough to remove some of the random component inherent in the errors and at the same time retain some of the error component that might be dependent on the flow regime existing during the period.

Once the correction factors were established, modifications to the next forecast in a series were made by subtracting the correction factor from the variable's forecast value. For example, if the 10 day average 36 h forecast boundary layer temperature error for Boston was + 2° K and the next 36 h forecast of boundary layer temperature in Boston was 288° K, the modified boundary layer temperature forecast for Boston after applying the correction would be 286° K.

Evaluation of the effects of the correction technique was accomplished in several ways. Printed output (Fig. 11) was produced which listed the individual station forecast errors, map average RMS errors and standard deviations, and numbers of stations whose forecast error values fell within specified ranges, both before and after the correction technique was applied. This printout was examined in order to compare the individual station errors before and after correction to help judge if the technique improved or degraded the forecast. By looking at the number of stations that fell into various error category ranges and noting the changes in the distribution, it was possible to gain an understanding of how the modification technique had altered the error patterns. Ideally one would like to see the number of errors on both extremes of the range get smaller and the number of errors in the middle categories (near 0) get larger. The usual result (see Fig. 11) was to reduce the number of errors at one extreme, increase the number of errors in the middle categories, and increase slightly the number of errors at the opposite extreme. Comparing the map average RMSE and standard deviations before and after correction gives an objective measure of the value of the modification procedure. Improvement

12 HOUR FORECAST OF RH

A.

-80	30	-90	-40	80	-190	50	30
-80	-10	20	100	60	-120	-40	-190
-90	-180	-20	10	-50	-20	60	-60
30	150	100	140	190	110	10	150
-50	-30	50	-100	-190	-40	-90	-70
-150	-20	30	-110	-110	-90	-110	-70
-170	-130	-100	-170	-40	0	-20	-130
-20	-160	-100	60	-160	-130	-100	130
50	150	-80	40	110	40	140	70
100	150	140	60	150	150	-70	-20
-100	150	140	-10	-50	-130	-160	-190
-180	20						

RMSE = 105.1216   STANDARD DEVIATION = 163.3297

< -141	-95 to -141	-48 to -94	-1 to -47	0 to 47	48 to 94	95 to 141	> 141
12	13	14	13	11	9	10	7

12 HOUR FORECAST OF RH

B.

-89	-89	-45	116	-183	65	32
-87	65	147	115	-93	-25	-151
-79	-58	-23	-8	21	63	-76
36	74	93	168	61	-29	107
-31	18	-121	-198	-89	-96	-116
-98	24	-91	-96	-117	-77	-88
-163	-40	-131	20	-16	17	-77
15	-123	129	-148	-143	-116	30
-32	25	-17	44	58	102	19
-29	-46	-64	43	81	-172	-89
-105	33	-23	-17	-149	-215	-208
-230	110					

RMSE = 100.4297   STANDARD DEVIATION = 164.5880

< -141	-95 to -141	-48 to -94	-1 to -47	0 to 47	48 to 94	95 to 141	> 141
13	11	15	14	18	9	6	3

Fig. 11. Printed Output Generated for the FOUS Forecast Correction Technique

    A. Individual FOUS station forecast errors, map average root mean square error, and standard deviation (all multiplied by 10), and number of stations falling into labeled category ranges before correction procedure was applied

    B. Same as A except after correction procedure was applied

in the forecast is indicated by a reduction of both RMSE and standard deviation after the correction technique is applied.

Examples of a graphical display of the RMSE and standard deviations before and after correction over a seven day period are presented in Figs. 12-18. On balance, they suggest that improvements to LFM-II forecasts can be realized using a dynamic correction procedure of this type. Specifically, we found that forecasts of sea level pressure (Fig. 12) are improved on some days and degraded on others. 1000-500 mb thickness forecasts show improvement in the 12 h forecasts (Fig. 13) but little effect or even slight deterioration in 24, 36, and 48 h forecasts (Fig. 14). The effect on layer mean relative humidity forecasts is very similar to that for sea level pressure; i.e., better forecasts on some days but degraded forecasts on others. Prospects for improving boundary layer temperature forecasts are better, with clear improvement shown for 12 and 36 h forecasts (Fig. 15) but mixed results at 24 and 48 h (Fig. 16). Boundary layer relative humidity forecasts show clear improvement at 24 and 48 h (Fig. 17) and marginal improvement at 12 and 36 h (Fig. 18). It would appear that the diurnal variations found for the forecast errors in boundary layer variables also have an impact on the effects of the forecast correction technique.

One other method was used to help evaluate the effectiveness of the FOUS correction technique. Four-panel displays were generated in which panel (a) depicts the LFM-II forecast, panel (b) the corrected LFM-II forecast, panel (c) the raw error field, and panel (d) the error field after the correction has been applied. Fig. 19 shows the four-panel display for boundary layer temperature and is a good example of a case in which the correction technique proved to be effective in improving the forecast. Note that in Fig. 19(c) there are negative boundary layer temperature errors whose magnitudes exceed $8°$ K. Fig. 19(d), representing the error field after the application of the technique, shows negative errors of only $1°$ K in the same area and an overall reduction in the magnitude of most of the forecast errors. This example is not meant to represent a typical result since, as should be clear from the discussion above, not all variables to which the correction technique was applied showed consistent improvement in the forecasts.
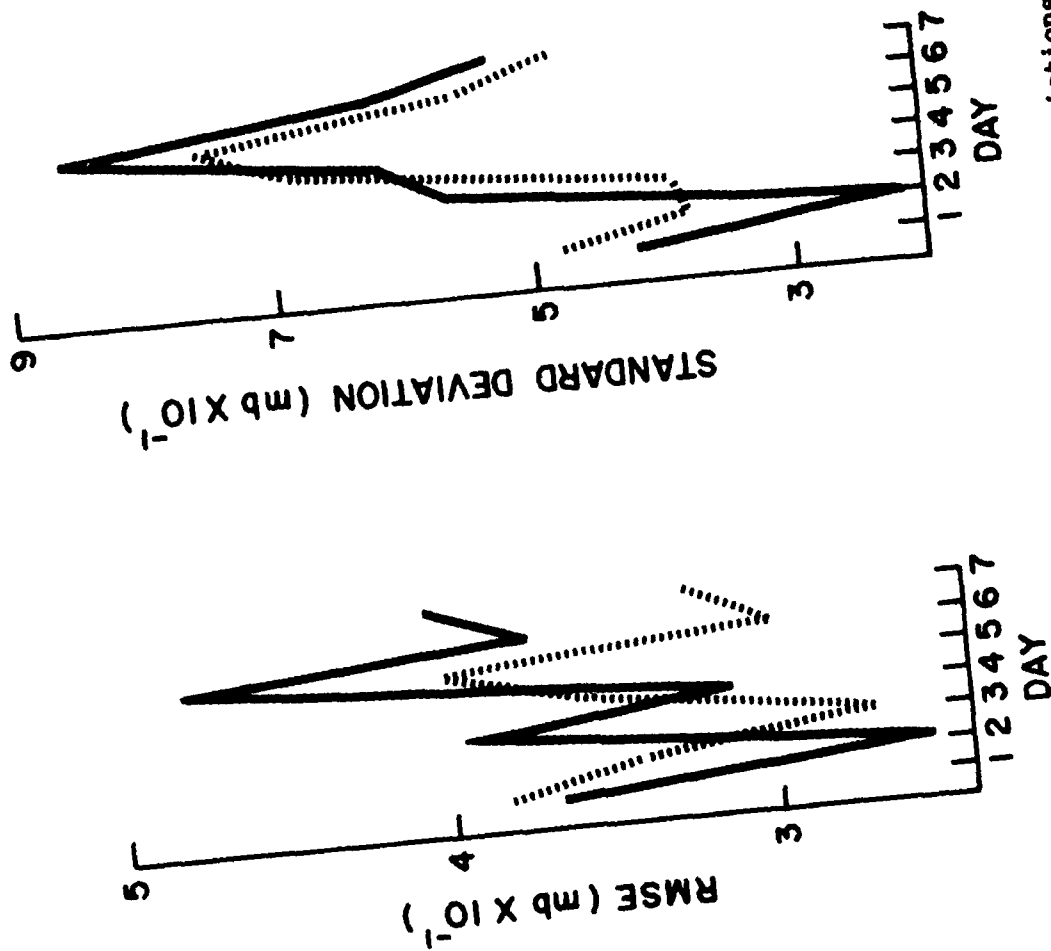
Fig. 12. Map Average Root Mean Square Errors and Standard Deviations (tenths of mb)
Before (dotted line) and After (solid line) Correction over a Seven Day Period
for 24 h Forecasts of Sea Level Pressure

36
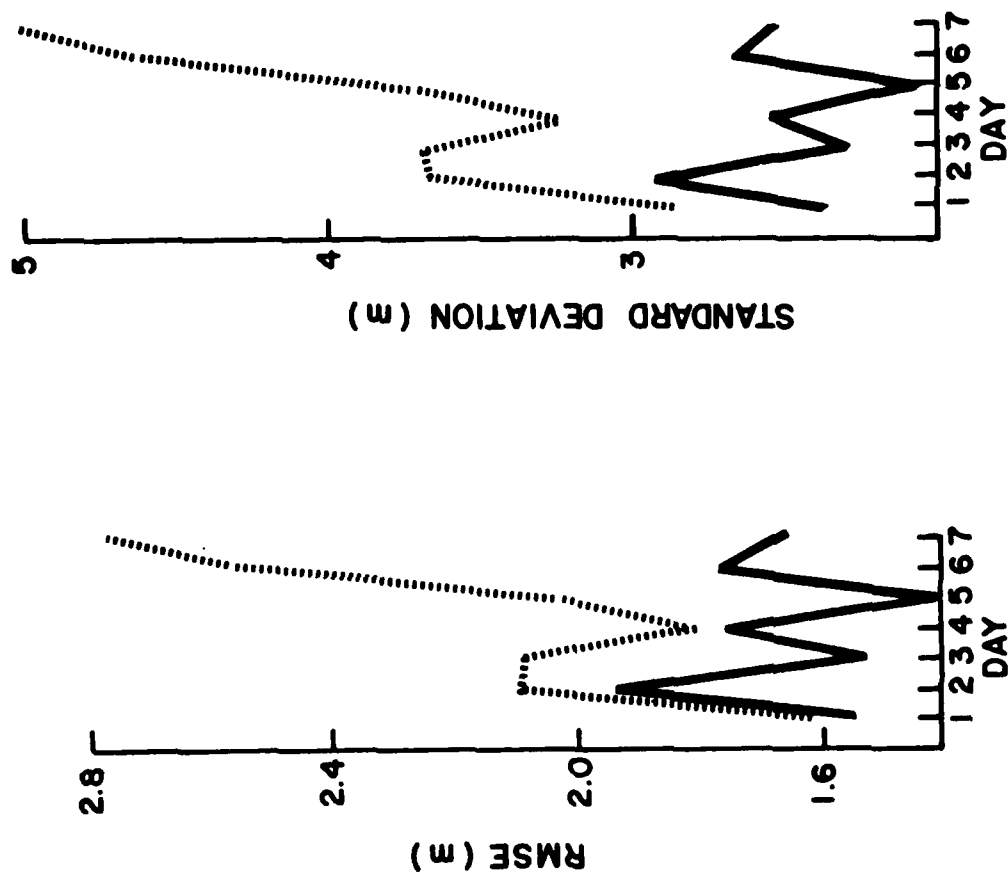
Fig. 13. Map Average Root Mean Square Errors and Standard Deviations (meters) Before (dotted line) and After (solid line) Correction over a Seven Day Period for 12 h Forecasts of 1000 – 500 mb Thickness
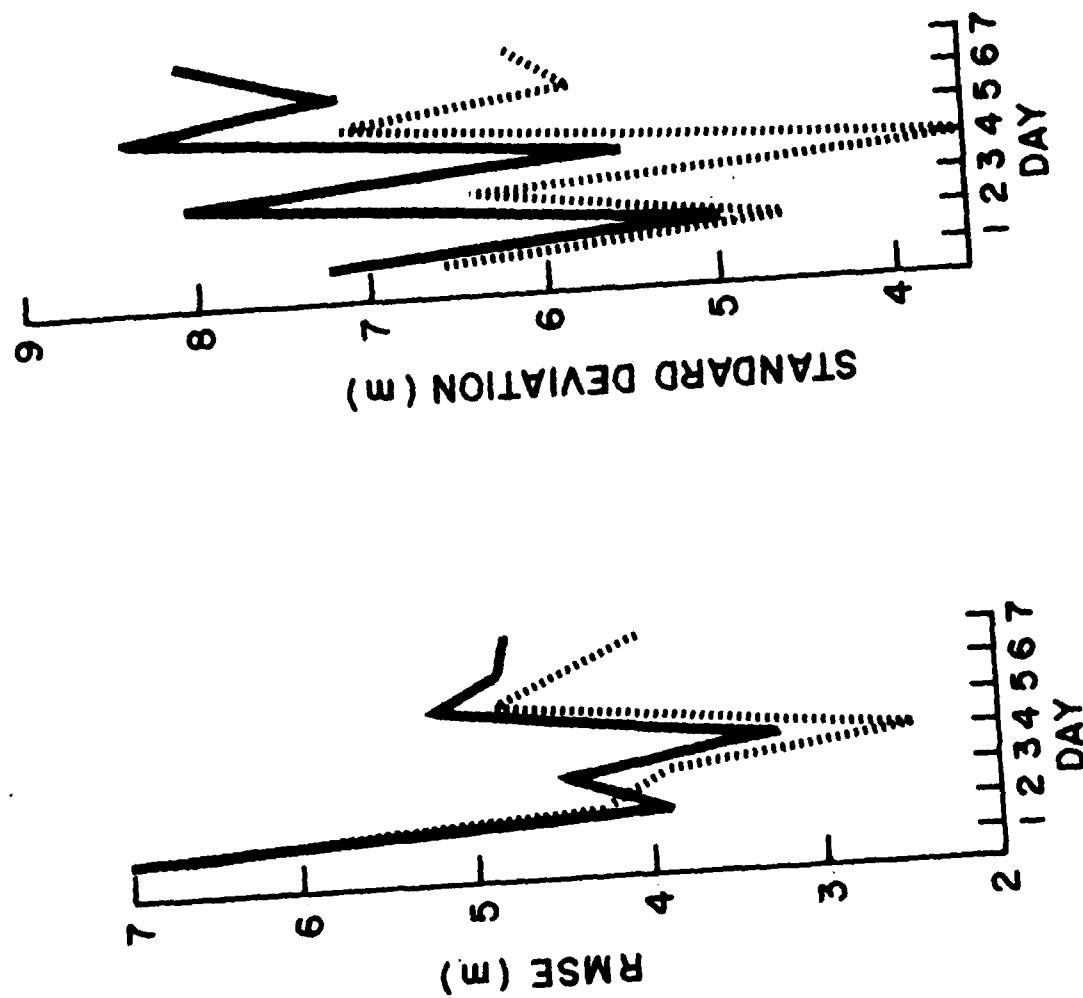
Fig. 14. Same as Fig. 13 Except 48 h Forecasts of 1000 – 500 mb Thickness
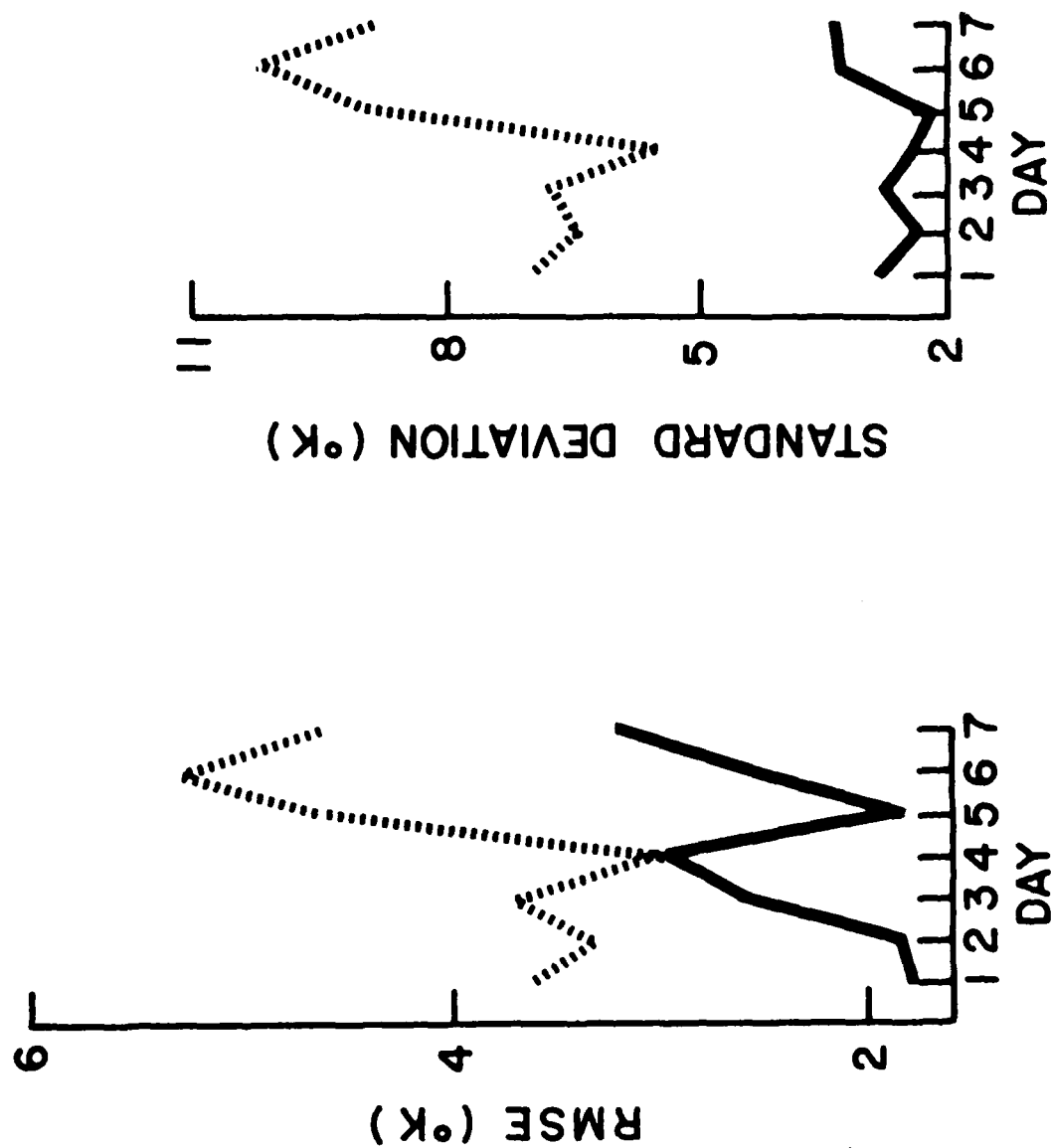
Fig. 15. Map Average Root Mean Square Errors and Standard Deviations (°K) Before (dotted line) and After (solid line) Correction over a Seven Day Period for 12 h Forecasts of Boundary Layer Temperature
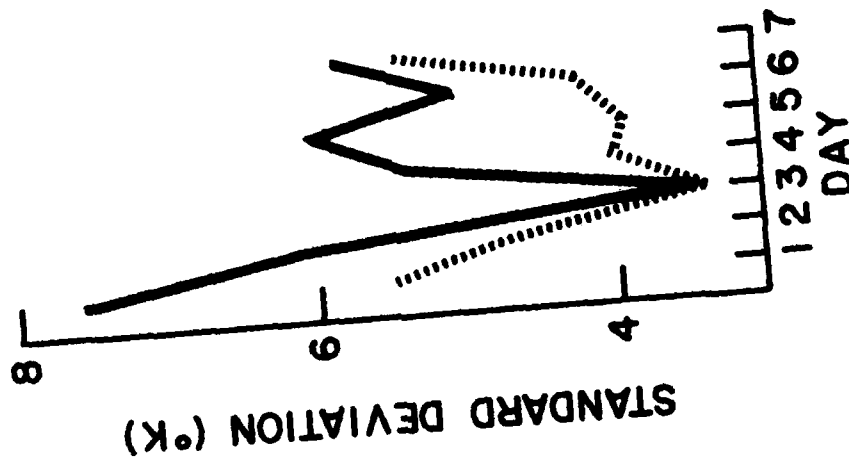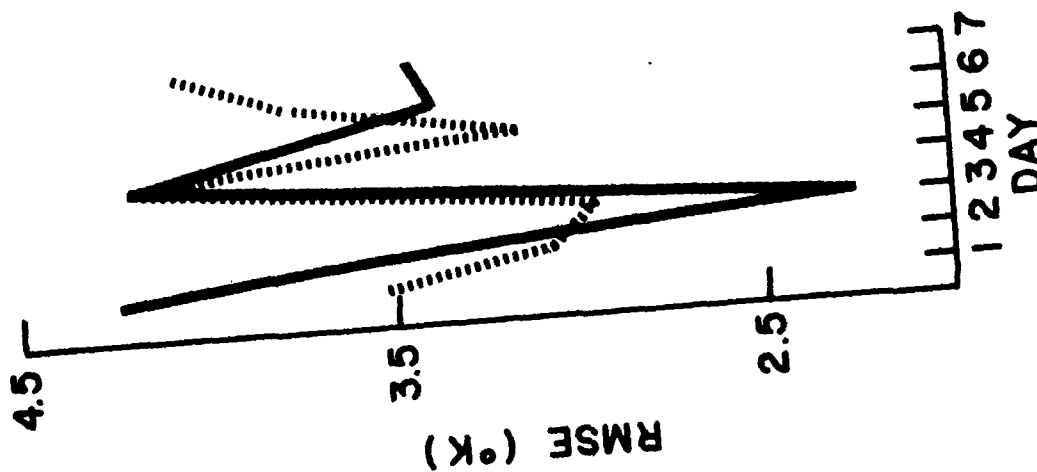
Fig. 16. Same as Fig. 15 Except 24 h Forecasts of Boundary Layer Temperature
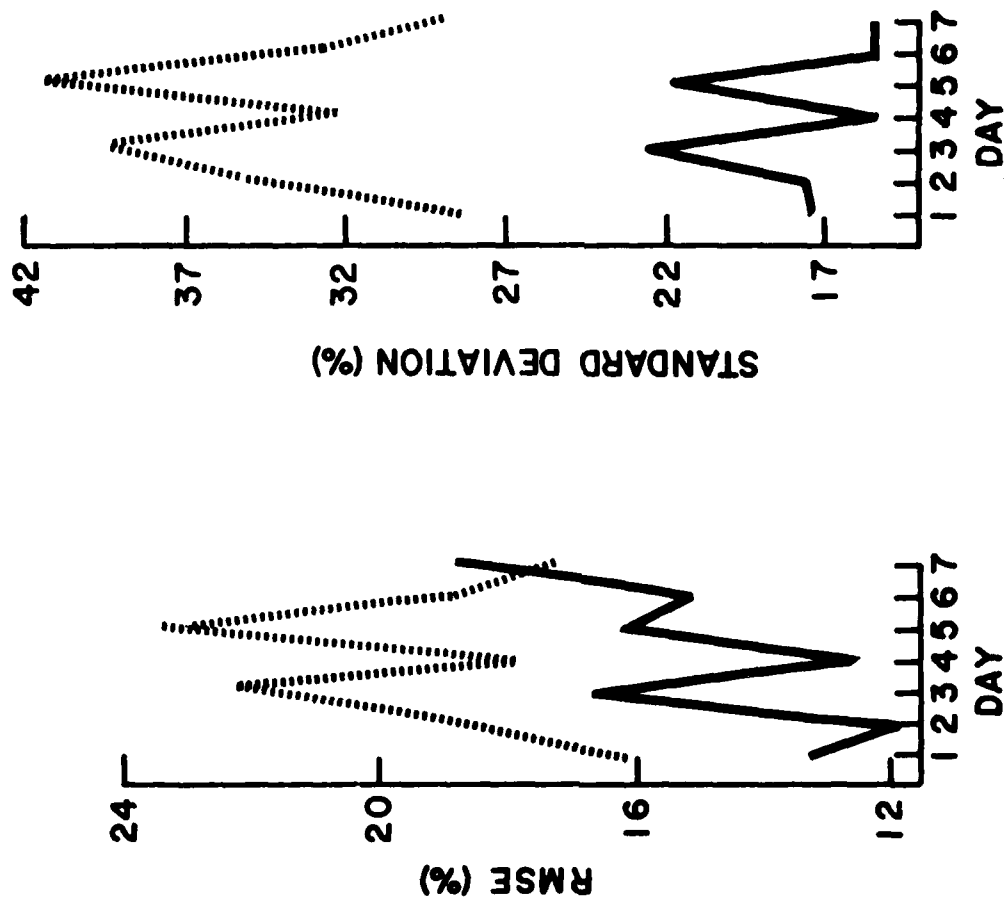
Fig. 17. Map Average Root Mean Square Errors and Standard Deviations (%) Before (dotted line) and After (solid line) Correction over a Seven Day Period for 24 h Forecasts of Boundary Layer Relative Humidity

41
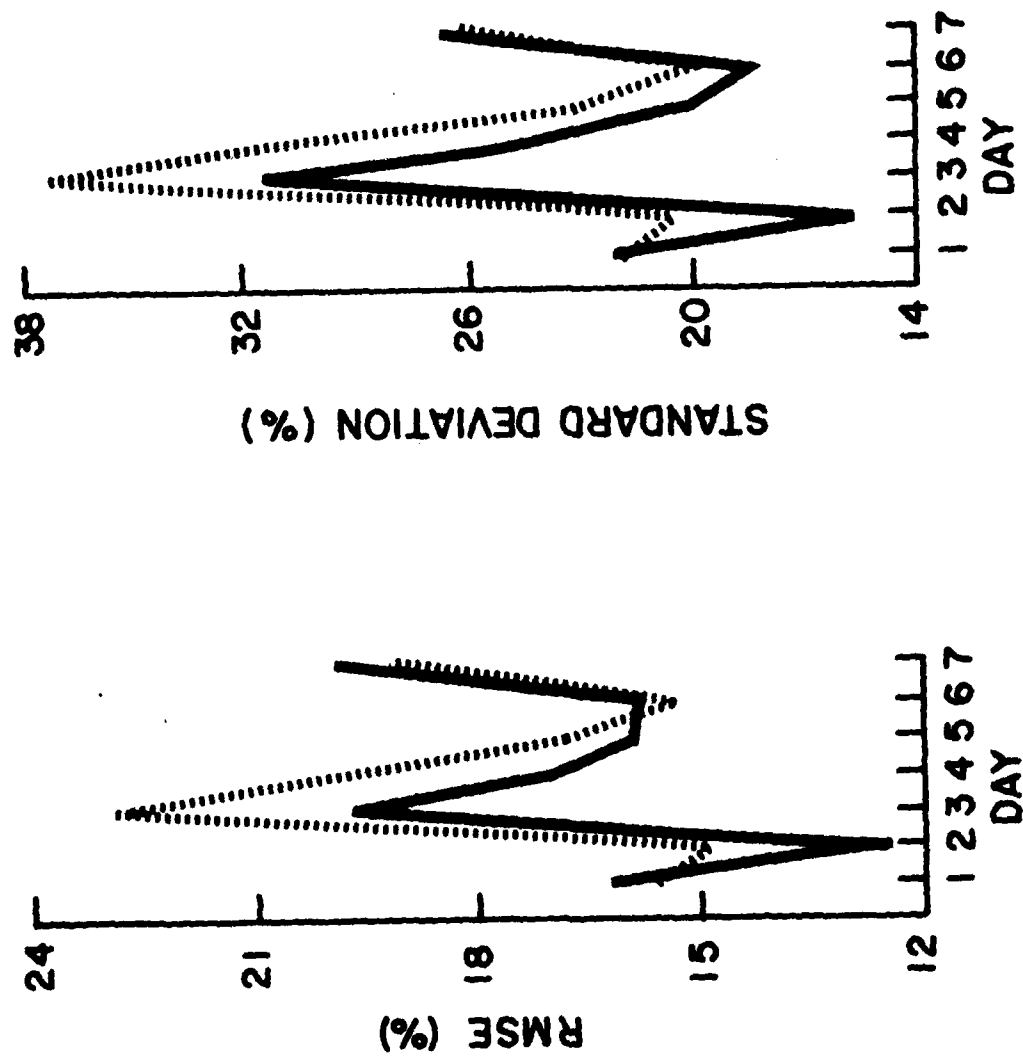
Fig. 18. Same as Fig. 17 Except 36 h Forecasts of Boundary Layer Relative Humidity

42
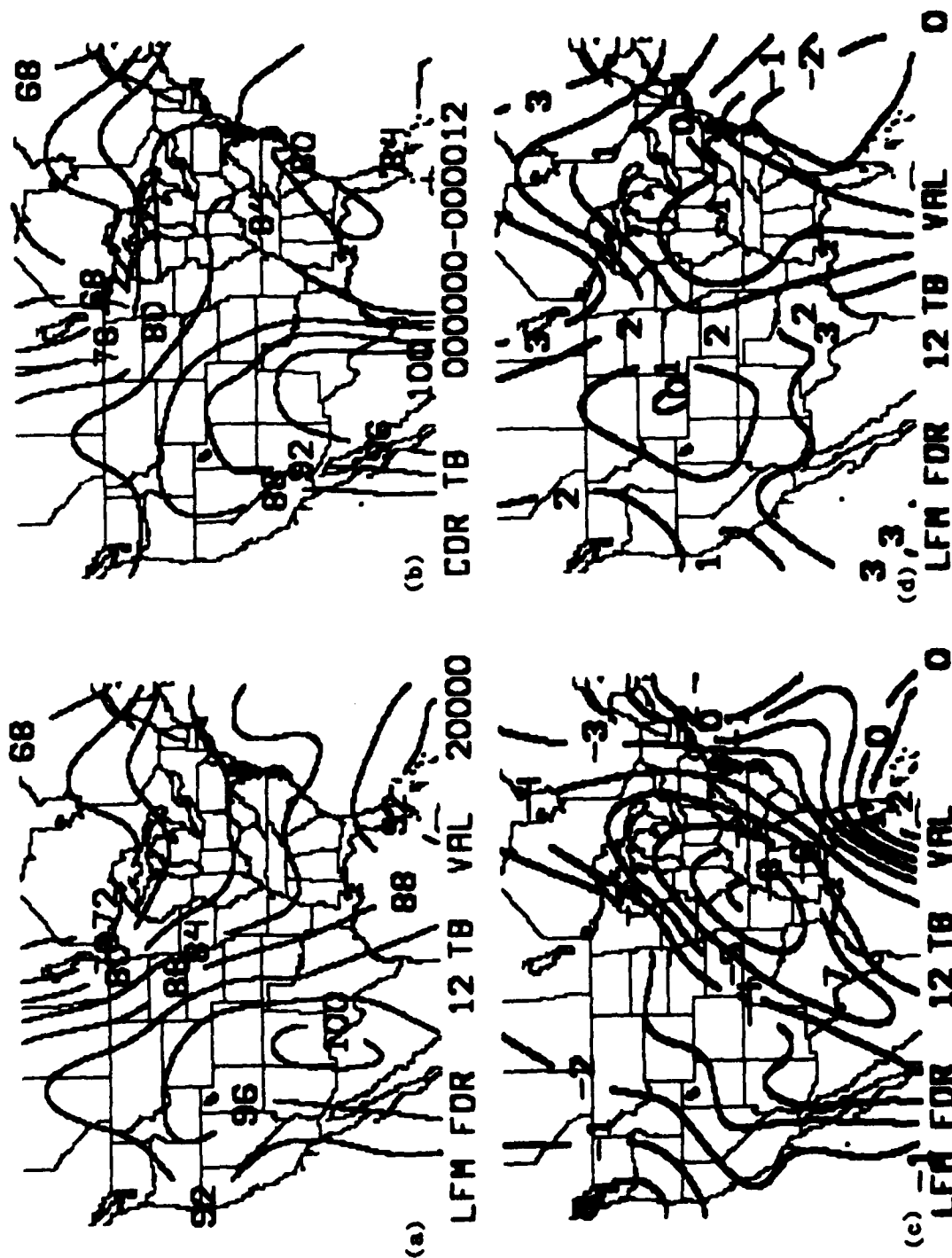
Fig. 19. Four-Panel Display Depicting: (a) 12 h Forecast of Boundary Layer Temperature (°K); (b) 12 h Forecast of Boundary Layer Temperature (°K) After Application of Forecast Correction Technique (200° K must be added to all values in both (a) and (b)); (c) Error Field for Forecast Depicted in (a) (°K); (d) Error Field for Adjusted Forecast Depicted in (b).

4. Conclusions

A second season of LFM-II forecasts was analyzed to identify persistent errors (bias) in selected variables. Forecasts were examined from 1 Oct 83 to 30 Apr 84 and were stratified into 00 and 12 GMT model runs. The results of the error analysis were very similar to those from a similar study performed on 1982-83 LFM-II forecasts. Sea level pressure is forecast too low east of the Rockies and too high west of the Rockies. Positive 1000-500 mb thickness errors are generally found east of the Rockies while negative errors can be found in the southwestern United States. Layer mean relative humidity is, on average, forecast too moist in the northern Rockies and too dry along the Gulf Coast. A similar pattern is apparent in the boundary layer relative humidity errors except that more of the nation shows a dry bias and the moist bias in the Rockies disappears for some forecast periods. Boundary layer temperature is forecast too warm along the Gulf Coast and too cold in the Great Lakes region. Errors in forecasts of boundary layer relative humidity and boundary layer temperature show strong diurnal variations. This diurnal influence is also apparent in some forecasts for 1000-500 mb thickness and layer mean relative humidity.

When the forecast errors were stratified by month no coherent trends are apparent although many of the variables show their maximum errors in December. A technique designed to test the feasibility of correcting FOUS forecasts based on a dynamic error adjustment procedure demonstrated some success. Some forecasts were degraded while others (particularly the boundary layer variables) showed a noticeable improvement at some forecast intervals.

The season to season consistency of the error fields lends credibility to the view that the errors are systematic. It is planned to stratify the forecasts from 1983-84 according to 500 mb flow patterns in an effort to gain additional insight into the sources of the model bias.

B. Forecast Guidance Displays

One of the most difficult variables to specify in meteorology is vertical velocity. It is also one of the most important atmospheric variables since it has a great impact on total cloud cover and precipitation. There are many methods used to estimate vertical velocity. The kinematic

method uses wind reports from three co-located radiosonde stations to calculate vertical profiles of vertical velocity, vorticity, and divergence. Variable values calculated by this method are valid near the center of the triangle formed by the three radiosonde sites. Ideally the three stations should be reasonably close to each other and all angles should be greater than about 35°.

SASC has written software to display vertical profiles of vertical velocity, vorticity, and divergence on McIDAS using the kinematic approach. The user need only specify a time (00 or 12 GMT) and three valid five-digit radiosonde station identifiers. Options exist to send the display to the McIDAS line printer (Fig. 20) or to the graphics terminal (Fig. 21), in which case the variable values are displayed on the McIDAS CRT. If the graphics terminal is selected, the user can also specify which variable(s) he wishes to see displayed (an option exists to display all three with one command), the color of the display, and whether the profile is to be plotted as solid or dashed lines. A triangle utilizing radiosonde reports from Chatham, MA, Albany, NY, and Portland, ME seems to give good results for the Boston area.

The displays depicted in Figs. 20 and 21 have pressure decreasing upward along the y-axis (linear scale for printed output and logarithmic scale for graphics terminal output) and variable values plotted on the x-axis. The units of the variable values are indicated in the level by level listing provided with the profiles. Documentation of the command structure for the vertical profiles is provided in Fig. 22.

*** TRIANGLE 1 72606 - 72518 - 74498 29120GMT ***

72606 43.60N 70.31W

PRESSURE MB	WIND DEG	M/S
100.0	310.0	14.0
150.0	315.0	17.0
200.0	315.0	27.0
250.0	335.0	21.0
300.0	340.0	43.0
350.0	340.5	39.0
400.0	340.0	22.0
450.0	338.0	19.2
500.0	340.0	17.0
550.0	347.8	19.0
600.0	345.0	13.7
650.0	350.0	7.8
700.0	355.0	7.0
750.0	5.8	8.0
800.0	11.5	8.7
850.0	10.0	10.0
900.0	14.0	9.2
950.0	361.0	11.3
1000.0	330.0	7.0
1012.0	320.0	4.0

72518 42.75N 73.79W

PRESSURE MB	WIND DEG	M/S
100.0	315.0	15.0
150.0	325.0	36.0
200.0	320.0	48.0
250.0	315.0	39.0
300.0	330.0	43.0
350.0	332.2	43.3
400.0	335.0	35.0
450.0	338.7	34.3
500.0	359.8	33.0
550.0	360.0	34.0
600.0	359.5	28.4
650.0	355.0	26.3
700.0	359.6	29.0
750.0	352.0	22.3
800.0	5.0	17.8
850.0		12.0
900.0	363.2	12.0
950.0	317.5	10.0
1000.0	305.0	6.0
1012.0	300.0	8.0

74498 41.66N 69.96W

PRESSURE MB	WIND DEG	M/S
100.0	295.0	10.0
150.0	295.0	23.0
200.0	315.0	28.0
250.0	305.0	28.0
300.0	330.0	35.0
350.0	335.0	39.3
400.0	330.0	24.0
450.0	325.0	15.6
500.0	336.0	19.0
550.0	335.9	16.0
600.0	337.0	16.0
650.0	347.1	12.7
700.0	355.0	9.0
750.0	380.0	10.1
800.0	343.7	10.3
850.0	350.0	9.0
900.0	3.2	8.0
950.0	355.3	9.0
1000.0	345.0	7.0
1012.0	380.0	5.0

PRESSURE MB	OMEGA 10-3MB/SEC	VORTICITY 10-5/SEC	DIVERGENCE 10-5/SEC
100.0	0.00000	.67714	-1.65268
150.0	.86798	12.56221	-.21926
200.0	1.40858	10.18838	-3.54320
250.0	3.36883	10.58162	-4.28016
300.0	5.78623	2.28198	-4.40702
350.0	7.87615	5.03910	-2.95266
400.0	8.48385	6.30538	-.57845
450.0	8.47801	8.42734	-.50171
500.0	8.02202	7.15238	2.32567
550.0	6.84878	7.03268	2.36731
600.0	5.37368	6.74332	3.53328
650.0	3.50140	6.17617	3.95571
700.0	2.02919	7.21489	1.93313
750.0	.97851	6.43898	2.24550
800.0	.17811	4.92977	.90001
850.0	-.17744	2.30852	.52218
900.0	-.83000	1.80778	.88807
950.0	-.22755	.18547	-1.29788
1000.0	.10885	-1.60173	-.03009
1012.0	0.00000	-1.78601	1.77085

INTEGRATION OF DIVERGENCE = .00000 10-5/SEC

W=OMEGA V=VORTICITY D=DIVERGENCE

Fig. 20. Line Printer Display of Vertical Profiles and Variable Values

46
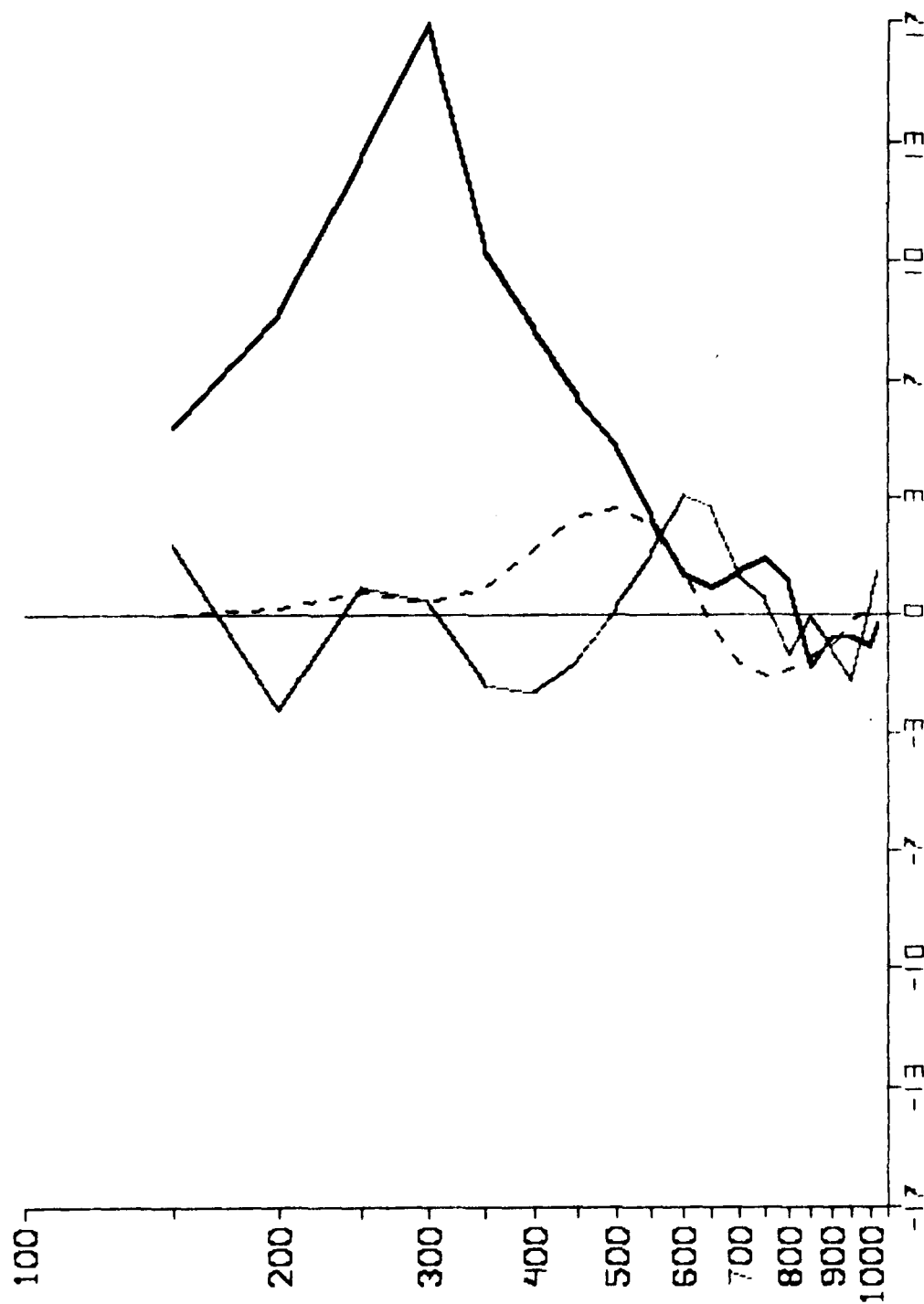
Fig. 21. Graphics Terminal Display of Vertical Profiles

COMMAND: PLOT VERTICAL PROFILES   KEY IN: WV
PROGRAMMER(S): R. Schechter/M. Niedzielski   DATE: July 84

                                                CHAPTER 9

COMMAND FORMAT:

        WV TIME ID1 ID2 ID3 PARAMETER COLOR

PARAMETER DESCRIPTION:

        TIME - Date and time of radiosonde observations (DDHHOO). If date
               is omitted, most recent day is used.

        ID1 - ID3 - Five digit RAOB station identifiers

        PARAMETER -   OMG = OMEGA (Vertical Velocity)
                        VOR = VORTICITY
                        DIV = DIVERGENCE
                        ALL = ALL THREE (OMG, VOR, DIV) ARE PLOTTED
                        If no parameter is specified the vertical
                        profiles and parameter values at each pressure
                        level are sent to the line printer.

        COLOR -   1 for red, 2 for green, 3 for yellow. Negative
                        values produce dashed profiles. If no color is
                        specified, default is yellow. Color is not
                        specified if PARAMETER = ALL (OMG will be dashed
                        yellow, VOR solid green and DIV solid red) or if
                        output is to be sent to line printer.

EXPLANATION: The WV command is used to display a plot of vertical
                profiles of OMEGA (vertical velocity), VORTICITY, and
                DIVERGENCE calculated by the Bellamy (kinematic) method.

        Fig. 22. Command Structure Format for Display of Vertical Profiles

                                    48

III. BOUNDARY LAYER METEOROLOGY

A. Turbulence Structure Function C_N^2

The Air Force Electronic Systems Division and Mitre Corp. are investigating the performance of a tactical tropospheric scatter radio link during different seasons and at varied geographic locations. AFGL is conducting atmospheric research to enhance the understanding and interpretation of test results.

Troposcatter radio propagation is based on the scattering of electromagnetic energy from refractive discontinuities existing in turbulence in the lower atmosphere. Measurements and characterization of such refractive index fluctuations in the atmosphere are therefore needed.

The microwave refractive index n of a medium is defined as the ratio of the speed of microwave propagation in free space to its speed in the medium.

Turbulent eddies, which are the dominant factor in microwave scattering, have characteristic dimensions in the inertial subrange (i.e., 1,000 m – 1 m). In this region energy cascades from larger eddies where energy is input, to smaller and smaller eddies until dissipation occurs in the molecular range. Theory and measurement support the hypothesis that this cascading has a defined energy to frequency ratio described by Energy = $CK^{-5/3}$. Assuming the validity of this relationship, turbulence can be defined completely by the coefficient C. When discussing refractive index of turbulence, C is designated as C_N^2, the refractive index structure function, where $N = (n-1)10^6$. Other structure functions refer to temperature (C_T^2) and humidity (C_Q^2).

Two methods were used in this study to produce C_N^2. The first determines the energy spectrum and calculates the associated C. The second is derived according to the formula

$$\overline{(N(X_1) - N(X_2))^2} = C_N^2 \, r^{2/3}$$

(Tatarskii, 1971),[12] where N is the fluctuating refractive index at two points X_1 and X_2 separated by distance r.

---

12. Tatarskii, V. I., 1971: **The Effects of the Turbulent Atmosphere on Wave Propagation**. Kefer Press, Jerusalem, 472 pp.

Turbulence data were recorded onto magnetic tape by an aircraft-mounted refractometer flown in 1984 in a series of flights over England, Florida, Arizona, and Massachusetts. Multi-channel data retrieval was employed, recording up to 200 samples per second of digitized refractivity data, and temperature and pressure readings, in level flight and during downward spiraling flight paths.

SASC developed software to process these data tapes, separating out refractivity from temperature and pressure and displaying representative samples of each of these quantities for each data record.

Subsequent computer programming produced C_N2 values by both methods mentioned above. To find the energy spectrum, time-sequenced digitized refractometer data were converted to the frequency domain (.01 to 25 cycles) by Fast Fourier Transform. Aircraft indicated air speed and instrument gainfactors were applied and C_N2 was calculated for 256 frequency bands, samples were printed, and power spectra plots were produced showing fit to the -5/3 slope. Fig. 23 shows a sample of such a plot for record 35 of the first data tape over England on 7 Feb 84.

C_N2 was also produced according to Tatarskii's formula by using the difference between separated refractivity points, divided by $r^{2/3}$, where r is the product of the air speed and distance per sampling rate. C_N2 was produced for eight distances between selected points.

In addition, computer displays were produced showing temperature, pressure, and refractivity values during spiraling down flight periods. These resulted from a program that examined voltage data strings recorded during flight in a manner which interspersed temperature, pressure, and reference voltages on the same recorder channel. Temperature and pressure voltages were identified, selected out of each record and plotted, together with refractivity, as a function of time.

Turbulence profiles were completed for the English data and for the first series of flights originating at Hyannis, MA. Data from Florida, Arizona, and a second series from Hyannis remain to be analyzed.

B. RAYTRACE Program

The raytrace program used with atmospheric refractive profiles was the basis for several new computer programs developed to research various aspects of anomalous propagation of line-of-sight (LOS) microwave links and troposcatter links.
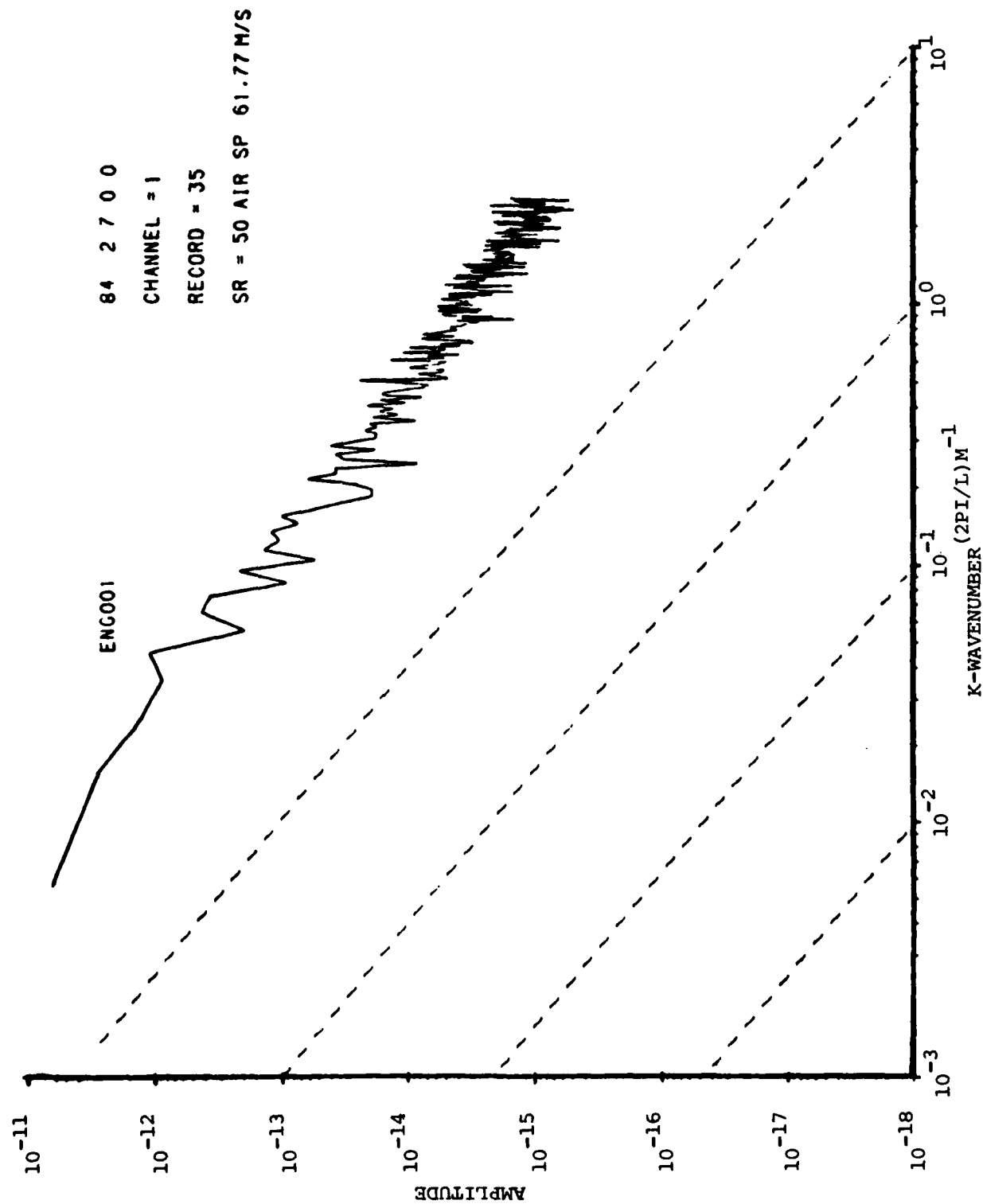
Fig. 23. Power Spectrum from Refractometer Flight over England, 7 Feb 1984

1. Troposcatter Links

Two raytrace programs, RYCRHST (a two-dimensional model) and RAYPR3D (a three-dimensional model), were formulated to examine the scattering of microwave energy by upper air turbulence in the common volume. The common volume is the zone created by the crossing of the beams of the transmitter and receiver which are positioned at opposite ends of the troposcatter link. The programs:

(1) Compute the common volume using given beam geometry modified by a measured refractive index profile.

(2) Subdivide the common volume into cells. The raytrace program is used to calculate the trajectory of the ray from the transmitter that illuminates each of these cells and is scattered down to the receiver.

(3) Develop a histogram of the relative time of arrival of the rays from all cells.

(4) Compute a plot of the relative energy in each of the histogram bins (delay time windows) using a model of scattering based on scattered energy equal to

$$\left[\sin \frac{\theta}{2} \right]^{-11/3} \cdot C_N^2,$$

where θ is the scattering angle and C_N^2 is the refractive index structure function. The values of C_N^2 are provided to the program as input data. These programs are used in conjunction with atmospheric data from the troposcatter radio tests. The purpose is to determine how well measured data and a propagation model can simulate or explain radio performance. Other scattering models will be substituted to evaluate the efficacy of the scattering models to predict radio performance.

2. LOS Links

A new program RYBEND was formulated and is used to simulate coupling energy into and out of a radio duct that is too high relative to transmitter/receiver on a LOS link to cause anomalous propagation under normal ray optics. Several days of data of this type from the Friolzheim-Muhl LOS link were reexamined and processed with the RYBEND program. Reasonable agreement between the observed and calculated rays was found in these cases (see Figs. 24 and 25).
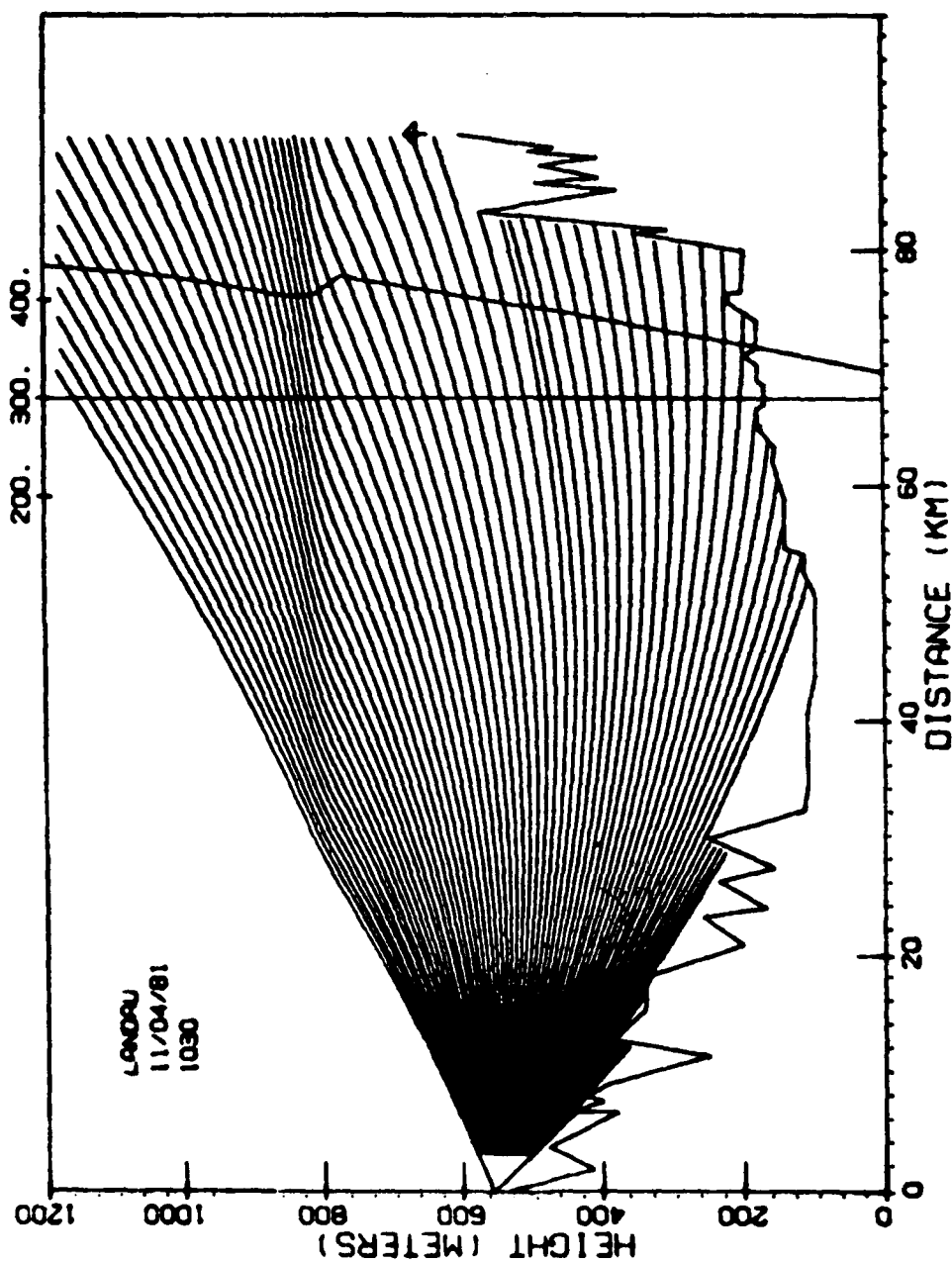
Fig. 24. Standard Raytrace on Langerkopf-Friolzheim Link Using Radiosonde Data for Landau, 4 Nov 81
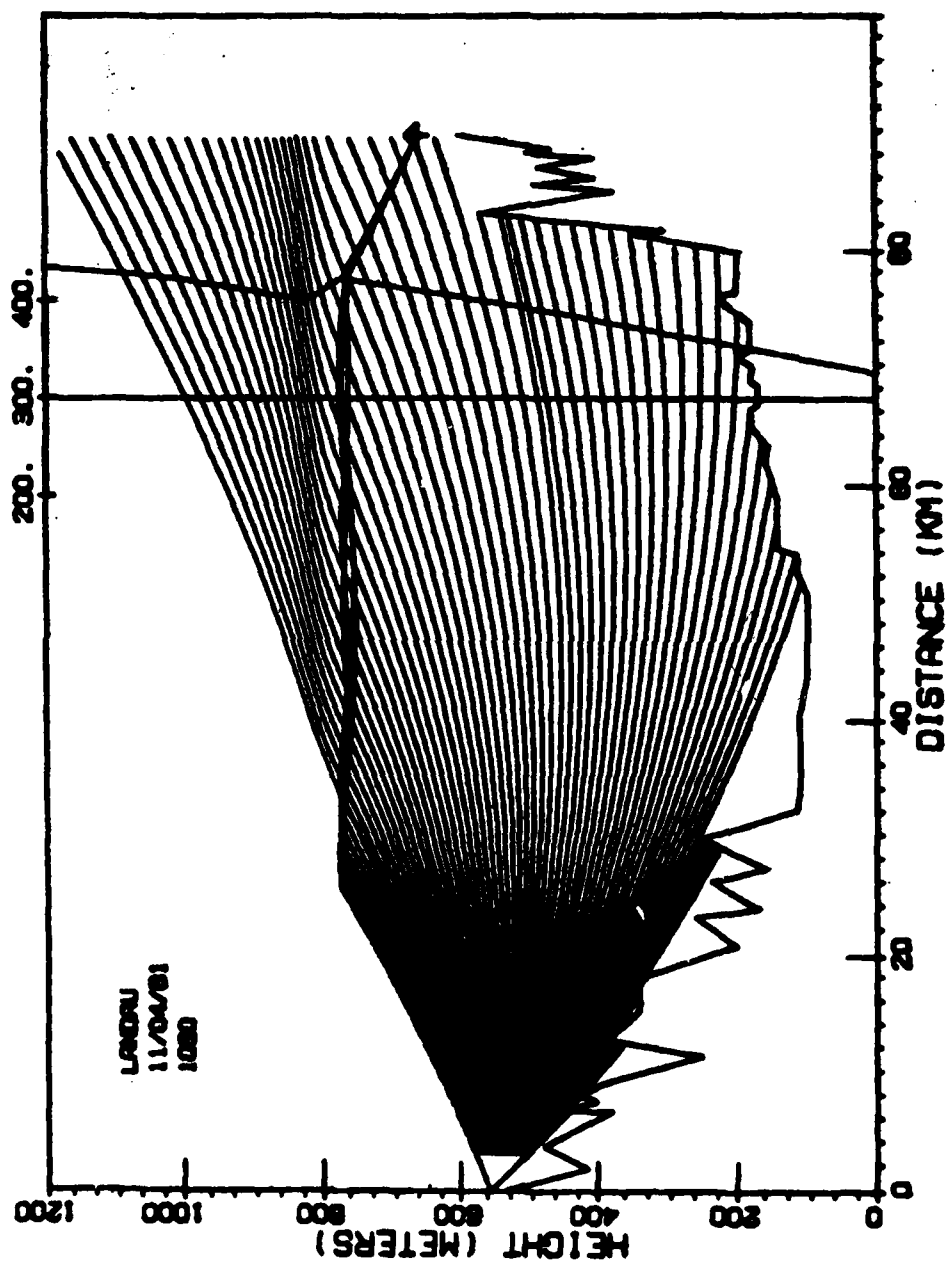
Fig. 25. Same Case as Fig. 24 with Selected Rays Mechanically Coupled Into/
Out of Duct

54

RAYPROGSUB4 is an improved version of previously-developed RAYPROG4 and the multiple profile counterpart of RAYPROGSUB (see Gerlach, 1983[4]). The program will raytrace a LOS link with a maximum of four profiles of refraction. The program was used with data from the Prospect Hill-Saddleback Mt. LOS link.

C. Automatic Data Acquisition System (ADAS) Software

The Automatic Data Acquisition System (ADAS) telemeters temperature, humidity, and pressure to a ground station during radiosonde flights. Data are recorded on cassettes which are brought back to the laboratory for editing and computation.

A plan was devised by AFGL to use the Apple IIe microcomputer in the field as an interface with ADAS. This would simplify data recording by eliminating the cassettes and would permit editing and computation in the field, thus increasing data reliability and providing field technicians with a tool for evaluating data quality. The ADAS was therefore hard-wired to the Apple as an RS 232 port.

SASC developed and debugged the following programs in Applesoft basic:

(1) RELHUM8, to calculate temperature and relative humidity, with the program requesting the proper input from the operator.

(2) PROGX30, to take in data during a balloon flight through the ADAS, format the data, and write it to disk.

(3) EDITPLOT44, used after the flight to read an edited or unedited data file from the disk, allow editing of the data, and produce line plots for pressure, temperature, pressure differences, and relative humidity as (see Fig. 26). It will also calculate various parameters, such as mean virtual temperature, virtual temperature, geopotential height increments, and refractive index. The revised edited data will then be written into a new file on the disk.

These programs are currently on hold because of problems with AFGL acquiring more Apple computers and the near future availability of the Zenith 100 computer. If the Zenith 100 is to be used in lieu of the Apple, these programs will be re-written into language suitable for the Zenith 100.

55

WHICH VARIABLE TO PLOT? YP,ZT,K,D?T

```
 0                                                            P

 1                                                         P
 2                                                          P
 3                                                         P
 4                                                         P
 5                                                         P
 6                                                         P
 7                                                         P
 8                                                        P
 9                                                        P
10                                                        P
11                                                        P
12                                                        P
13                                                       P
14                                                       P
15                                                       P
16                                                       P
17                                                       P
18                                                       P
19                                                      P
20                                                      P
21                                                      P
22                                                      P
23                                                     P
24                                                     P
25                                                     P
26                                                     P
27                                                     P
28                                                    P
29                                                    P
30                                                    P
31                                                    P
32                                                    P
33                                                   P
34                                                   P
35                                                   P
36                                                   P
37                                                   P
38                                                   P
39                                                  P
40                                                  P
41                                                  P
42                                                  P
43                                                  P
44                                                  P
45                                                 P
46                                                 P
47                                                 P
48                                                 P
49                                                 P
50                                                 P
```
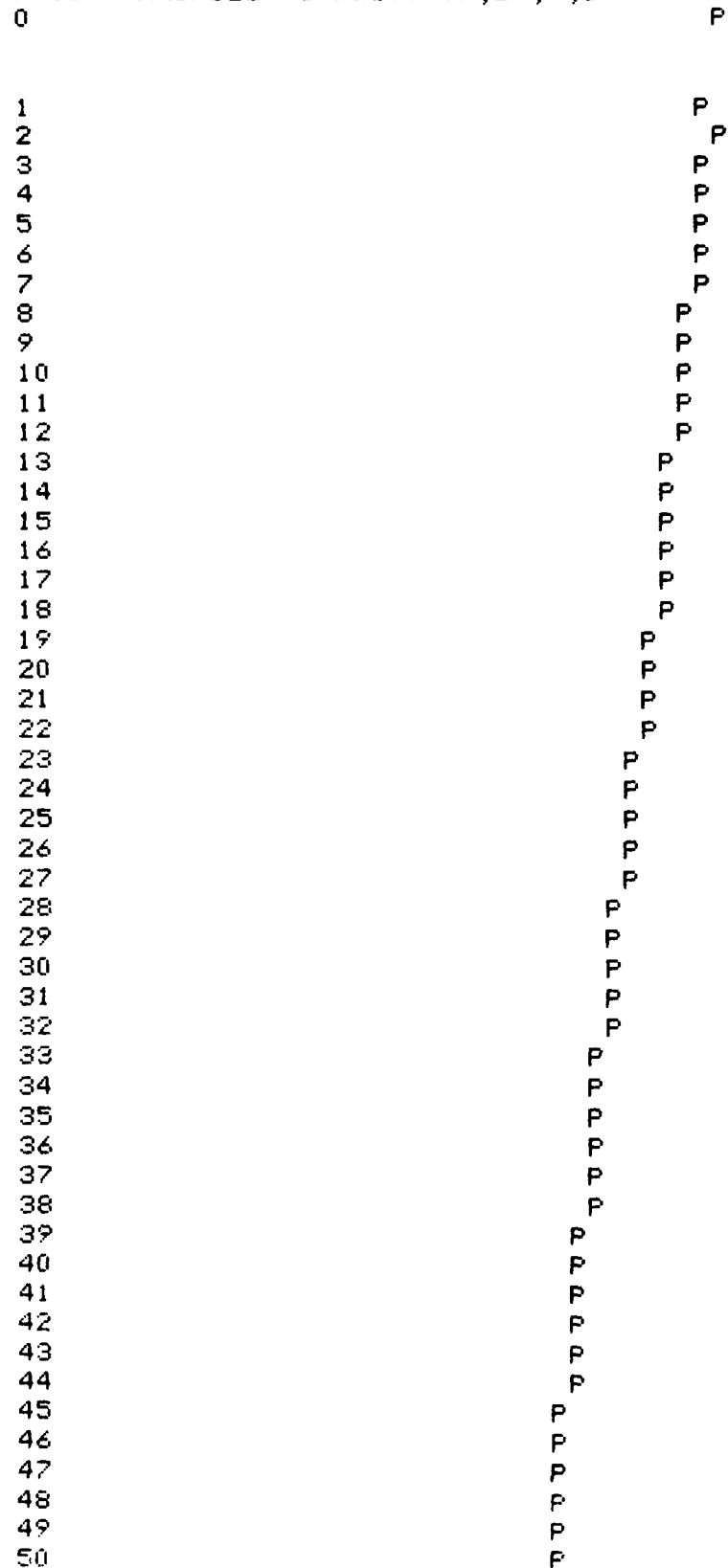
Fig. 26. Line Plot for Pressure Produced by EDITPLOT44

56

D. Surface Wind Flow Model

AFGL acquired a surface layer wind flow model from the U.S. Army
Atmospheric Sciences Laboratory at White Sands, NM. This numerical model
is used to estimate surface layer wind fields over complex terrain, at
horizontal resolutions ranging from 60 m to 400 m, covering an area
approximately 5 km X 5 km.

Inputs to the model include limited meteorological data such as
single station 850 mb and 700 mb geopotential heights and potential temp-
eratures, surface wind information, and detailed terrain and vegetation
information (100 m horizontal resolution). The model produces surface wind
and potential temperature fields which correspond primarily to terrain con-
figuration and static stability. Feasibility of using a modified version
of this model in conjunction with a Gaussian plume diffusion model for
estimating toxic chemical dispersion is being investigated by AFGL.

As acquired from the Army the computer program was designed to run
on a Univac 1108. SASC was tasked to adapt the code for use on a CDC Cyber
750, make test runs, and incorporate modifications to meet Air Force needs.

Meteorological, terrain, and vegetation data were obtained for the
area around Ft. Polk, LA for use in testing the model. These data were
reconstructed and lodged as resident Cyber mass storage files accessible by
the model. Disparities between Univac and Cyber in the method of handling
common parameters were resolved and meteorological input data were made
compatible.

Files containing fields of surface potential temperatures and u and
v-wind components were created by the model for plotting purposes. The
National Center for Atmospheric Research (NCAR) plotting package was used
to display terrain contours with wind vectors superimposed to demonstrate
the model's wind flow simulation. Temperature contours and wind stream
lines were also displayed.

Fig. 27 shows a typical model output using Ft. Polk data.

E. AFGL Weather Test Facility

SASC is responsible for maintaining and operating the Weather Test
Facility located on Otis Air National Guard Base (ANGB) near Falmouth, MA.
In addition to daily site and instrumentation maintenance and repair,
special activities were also undertaken.
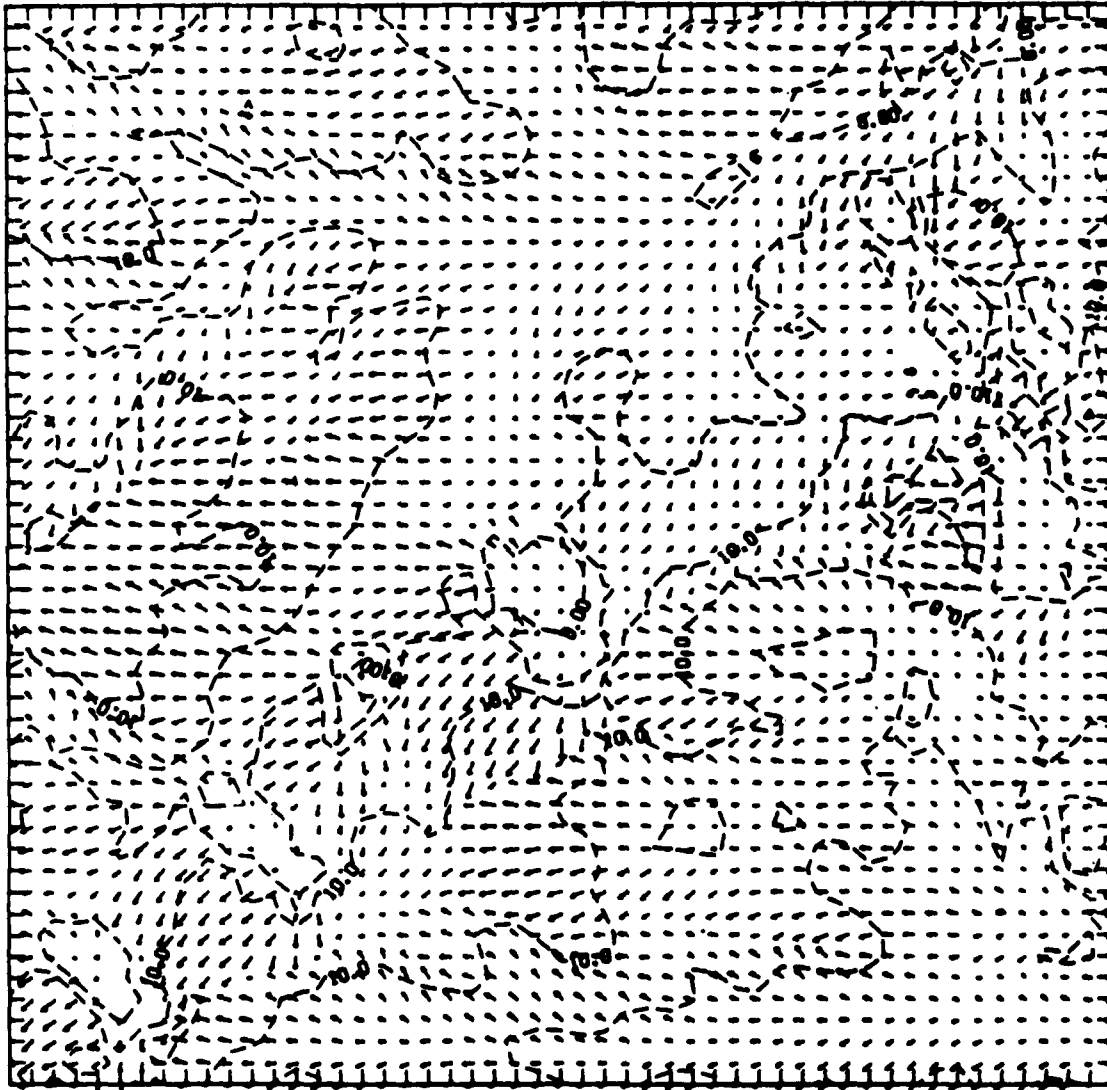
Fig. 27. Wind Vectors (arrows proportional to speed) and Terrain (dashed contours in 0.1 m) for Region around Ft. Polk, LA using Meteorological Data from a Single Observing Point

AFGL, the Department of Transportation, and the Federal Aviation Administration jointly participated in a program to evaluate visibility sensors for Runway Visual Range (RVR) and for use with the Automated Weather Observing System (AWOS). Manufacturers were invited to furnish and install their sensors. Foundations, power cables, and signal cabling were installed by AFGL, DOT, and SASC technicians. The AFGL data acquisition was used to record the data. Eighteen sensors from nine manufacturers were installed.

Sensors used as standards were four GMQ-32 transmissometers and five EG&G Model 207 forward scatter meters. Human weather observations were recorded during periods of inclement weather. Calibration of the trans-missometers was checked regularly using a laser transmissometer calibration test set. Calibration checks of the Model 207's were performed in the field using a laboratory calibrator. Any Model 207 found out of tolerance was replaced with a calibrated unit.

Calibration checks of the sensors under test were performed on a regular schedule. Frequent visual observations of the sensors were made with special emphasis during and following periods of inclement weather.

This program was completed in June 1984.

A modified version of the VR-301 visibility sensor (manufactured by HSS, Inc.) was delivered and installed. This sensor, designated "Present Weather," is designed to measure visibility and to identify types of ob-scurations to visibility, such as rain, fog, and snow. The Present Weather sensor utilizes additional inputs from a temperature sensor and a rain gauge. Data are fed into a personal computer for processing. Comparison standards are the AFGL GMQ-32 transmissometers, Model 207 forward scatter meters, and human observations. The comparison data and human observations are being used to modify the Present Weather software.

A DVM-1 Televisiometer (also from HSS, Inc.) system was installed. A shelter was provided for the DVM-1 and targets were constructed at dis-tances of 300 ft and 2,520 ft. A regular program of observation was ini-tiated. Measurements were taken using the two targets and the sky. Human observations were taken during the same time periods. These measurements and observations were normally taken twice daily. Because of the distance to the further target, visual range cannot be measured when visibility is

much less than 1.5 mi. Plans are to fabricate and install another target
at 700 ft. Visual range will then be measured to somewhat less than .25 mi
using the DVM-1.

IV. RADAR METEOROLOGY

A. Detection of Gust Front Shear by Radar

1. Introduction

Gust fronts, downdrafts, microbursts, and tornadoes are prominent and hazardous features of severe thunderstorms. These features are characterized by the presence of strong wind gradients commonly called wind shears. Strong shears are particularly hazardous to aircraft entering shear zones without warning. Several aircraft mishaps have been directly attributed to wind shear (e.g., Fujita and Caracena, 1977).[13] It would therefore be most advantageous to have a surveillance system that could provide sufficient information with enough lead time to allow the pilot to avoid regions of hazardous wind shear. Not only are these phenomena dangerous to aircraft in flight, but the effects at the ground can also be devastating. Numerous reports of straight-line wind damage have been documented. With advance warning, steps can be taken to avert disaster.

A potential advance warning system is NEXRAD (Next Generation Weather Radar), currently being developed for the U. S. Departments of Defense, Transportation, and Commerce. The nucleus of this system is a Doppler radar capable of measuring the velocity component of scatterers along its beam while sweeping through large volumes of air in short periods of time. These mean velocities are computed at distances as small as 150 m apart and are assumed to approximate the wind velocity component along the radar beam. An online computer that will be linked to the radar will generate products such as storm tracks and forecasts to assist the meteorologist or observer in issuing severe weather warnings. Among other products needed are detection and prediction of the motion and evolution of wind shear that is significant enough to pose a threat to aviation or to people and structures on the ground. From the radial velocity data one can estimate wind shear by computing shears in the radial and azimuthal directions.

---

13. Fujita, T. T., and F. Caracena, 1977: An analysis of three weather-related aircraft accidents. Bull. Amer. Meteor. Soc., 58, 1164-1181.

61

While these do not represent the total shear (the radar detects radial velocities only), it is proposed that they will provide sufficient data to identify the more significant structures.

In this report, SASC presents an algorithm for detecting strong shear regions with emphasis on locating and delineating gust fronts. One gust front case is examined. Results of several data averaging and thresholding schemes are presented and those combinations most likely to best identify high shear features are recommended for further study. Methods for the projection of feature motions are discussed.

2. Procedures

Two procedures we have developed will be described here. One uses radial shears and identifies maximum wind gradients along the radial direction only, using a quantity called "shear-weighted range." The other, more complex procedure estimates both radial and tangential shears, combines them on a rectangular coordinate system, and identifies the two-dimensional shear features.

a. Radial Shear-Weighted Range Algorithm

The radial shear-weighted range algorithm begins with a (2n+1) gate running average of Doppler velocities along the radial computed according to

$$\bar{V}_i = \sum_{k=-n}^{n} V_{i+k} \bigg/ (2n + 1), \tag{1}$$

where i is an index corresponding to range gates. Shears then are computed using

$$S_i = (\bar{V}_{i+m} - \bar{V}_{i-m})/(2m + 1) \, \Delta r. \tag{2}$$

where the difference is over 2m+1 gates and Δr is the spacing between gates. For the shears to be independent, $m \geq n$. Next, a threshold S_{th} is applied to the entire radial. For each interval along the beam in which $S_i \geq S_{th}$, a quantity we call "shear-weighted range" (R_{sw}) is computed

according to

$$R_{sw} = \sum_{i=1}^{N} S_i R_i \Big/ \sum_{i=1}^{N} S_i,$$ (3)

where R_i is a range from the radar in the interval and N is the number of gates in that interval. This R_{sw} will yield a range centroid for the shear interval. All intervals less than k gates in length are discarded at this point. The foregoing steps are applied sequentially to each beam.

An azimuthal association routine is applied to the R_{sw} values to determine if they are associated with features extended in azimuth. An R_{sw} is correlated with a shear feature if it occurs in an adjacent radial and is within 2 km of that feature's R_{sw}. For a feature to be retained the sum of the straight line distances between R_{sw}'s on adjacent beams must be at least 5 km. Fig. 28 depicts a range versus azimuth display of radial velocity radial shears. The regions outlined contain shear values above an S_{th} of $2 \times 10^{-3} s^{-1}$. Three R_{sw}'s (X's) are shown in the feature that extends over all of the azimuths. It is obvious that the largest feature meets the association criteria while the feature that extends over only three radials may or may not. It is likely that one radial feature at the top does not meet the criteria.

The azimuthal association and feature extent constraint allow the removal of insignificant or spurious shear regions while retaining the important ones. In the case of the gust front (the large feature of Fig. 28 is a gust front segment), a continuous curve can be constructed, and perhaps, in the case of a downburst, the highest shears would form an ellipse. This would facilitate determination of a curve of strongest shears that could be associated with a strong shear curve in the next consecutive radar scan at the same elevation. In this way, the feature might be tracked. (Section 5 contains a short discussion on shear tracking.)

b. Total Shear-Weighted Coordinate Algorithm

The total shear-weighted coordinate algorithm proceeds as follows: First, radial velocities are averaged as in Eq. (1) and radial shears are computed according to Eq. (2). (This averaging is necessary to reduce large spikes that would otherwise occur in shears computed beam-to-beam

63
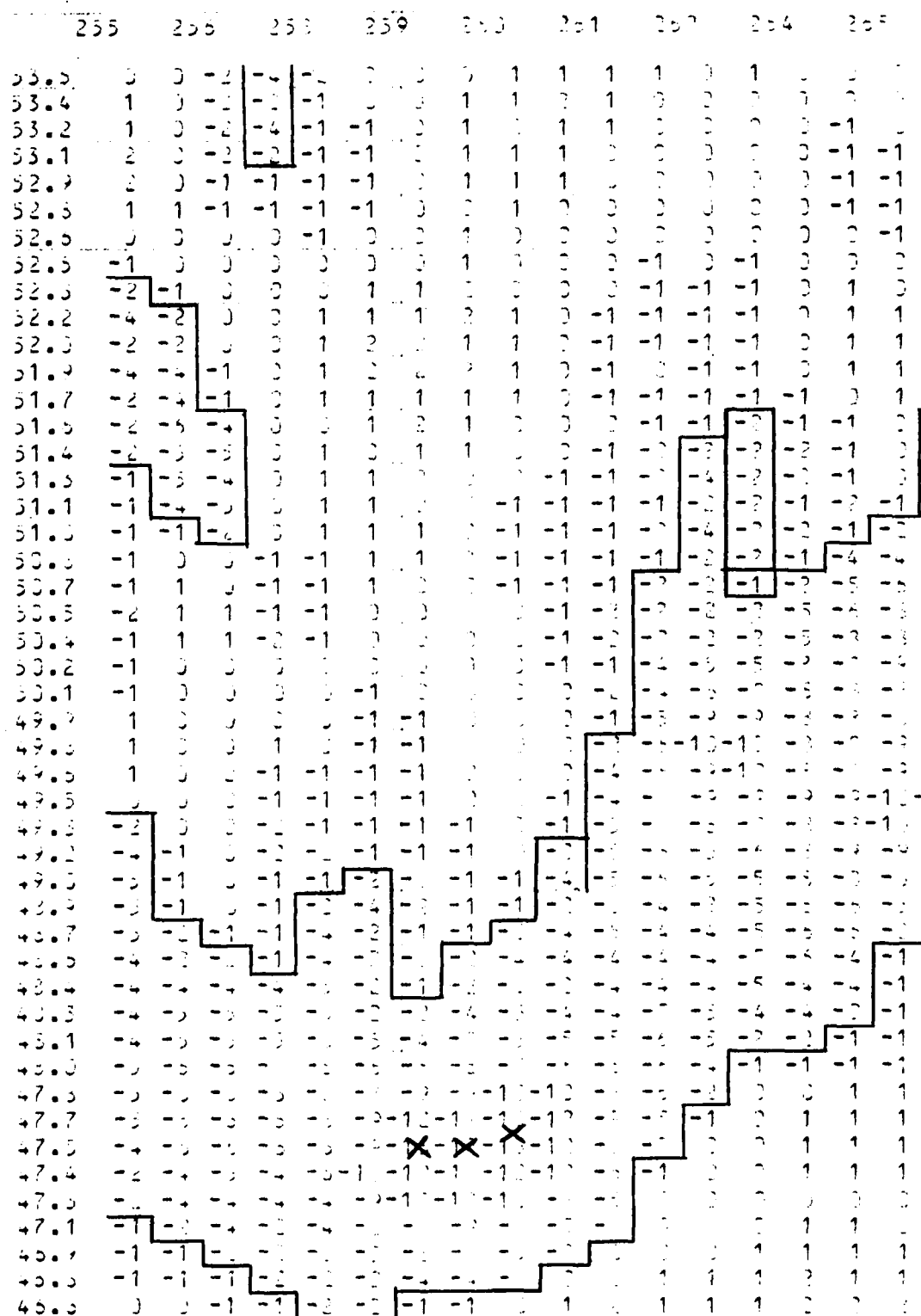
Fig. 28. Depiction of Radial Shear-Weighted Range Algorithm

Azimuth in degrees across top and range in km along left; numbers are radial shears [times $10^{-3}s^{-1}$]; straight lines are shear threshold contours; X's are examples of shear-weighted ranges.

or gate to-gate without averaging along the radial. If these spikes were not removed, there would be computational problems.) Then tangential shears are computed using

$$S_{\text{tan } ij} = (\bar{V}_{ij} - \bar{V}_{i,j-1}) \, R_i \Delta\theta \tag{4}$$

where the index i is over each range gate and j is the beam index. $\Delta\theta$ is the angular distance (in radians) between the two beams and R_i is the range at gate i. The foregoing steps are accomplished for all beams of interest.

Next a rectangular grid is defined to cover the region of the scan that contains the data to be analyzed. The radial shear values at polar points located within a radius of r_I from a rectangular grid point are averaged (with uniform weighting) and this average value $\bar{S}_{\text{rad}}$ is assigned to that rectangular grid point. Likewise, tangential shears at polar points located within r_I are averaged and the average value $\bar{S}_{\text{tan}}$ is assigned to that rectangular grid point. To do this, we must assume that in the small circle of radius r_I all radials are nearly parallel. At each rectangular grid point the average radial and tangential shears are combined. The shears are treated as orthogonal components of a two-dimensional wind gradient vector. The magnitude of the vector is computed according to

$$S_{T \ ij} = (S^2_{\text{rad } ij} + S^2_{\text{tan } ij})^{1/2} \tag{5}$$

where S_T is the total shear.

The next step is to apply a threshold S_{Tth} to the total shear. Then a quantity called "shear-weighted coordinate," which is analogous to R_{sw}, is computed for each shear interval containing values that exceed S_{Tth}. The scheme is illustrated in Fig. 29. Fig. 29a shows all east-west oriented intervals within a 20 km X 20 km square that contains a portion of a gust front. Fig. 29b depicts all north-south oriented intervals within the same square.

3. 30 Apr 78 Gust Front Case

The data we will examine are those of a gust front that occurred on 30 Apr 78 in Oklahoma. It was under surveillance by the Norman 10 cm Doppler radar of the National Severe Storms Laboratory (NSSL), Norman, OK.
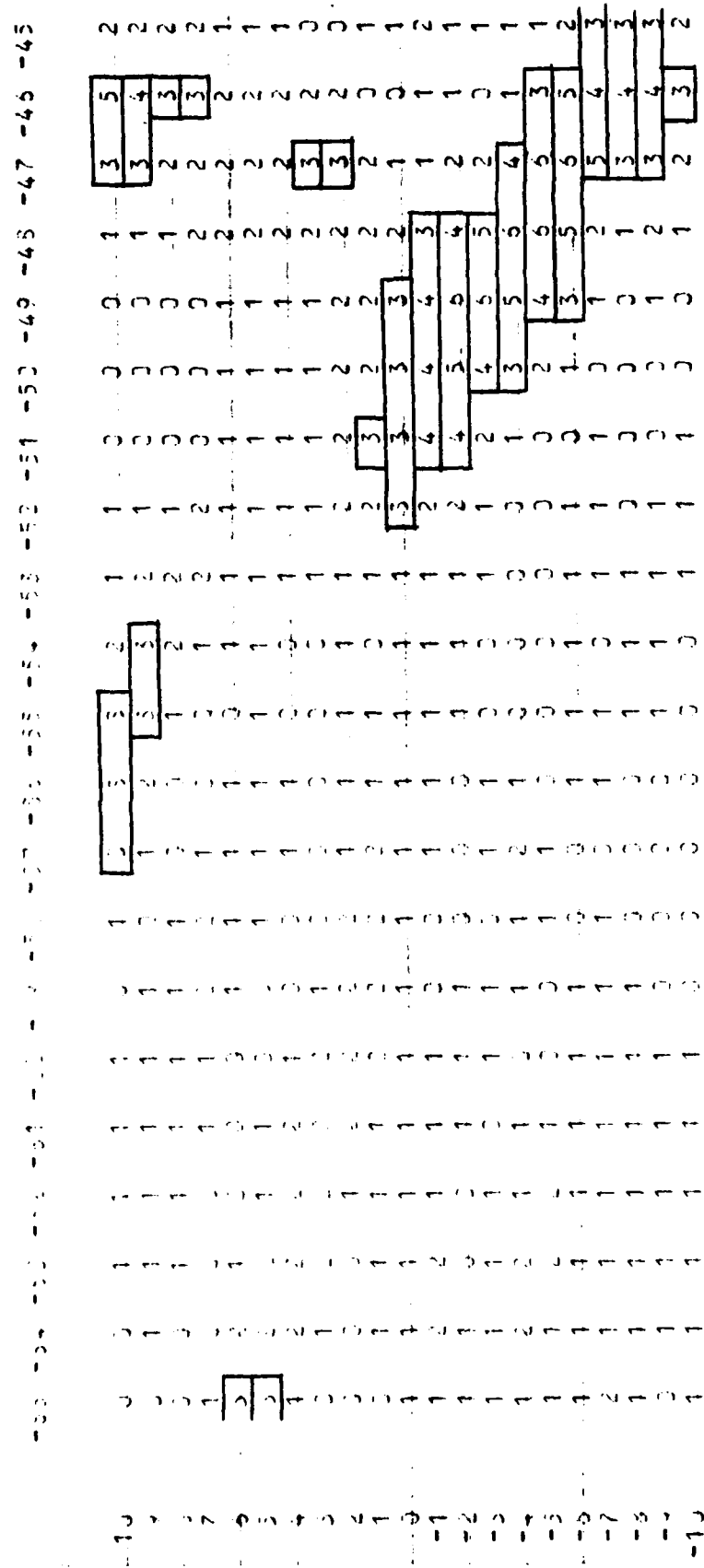
Fig. 29a. Depiction of Total Shear-Weighted Coordinate Algorithm

Across top are distances east of radar (km); on the left are distances north of radar (km); east-west oriented intervals used for "shear-weighted coordinate" computation are outlined.
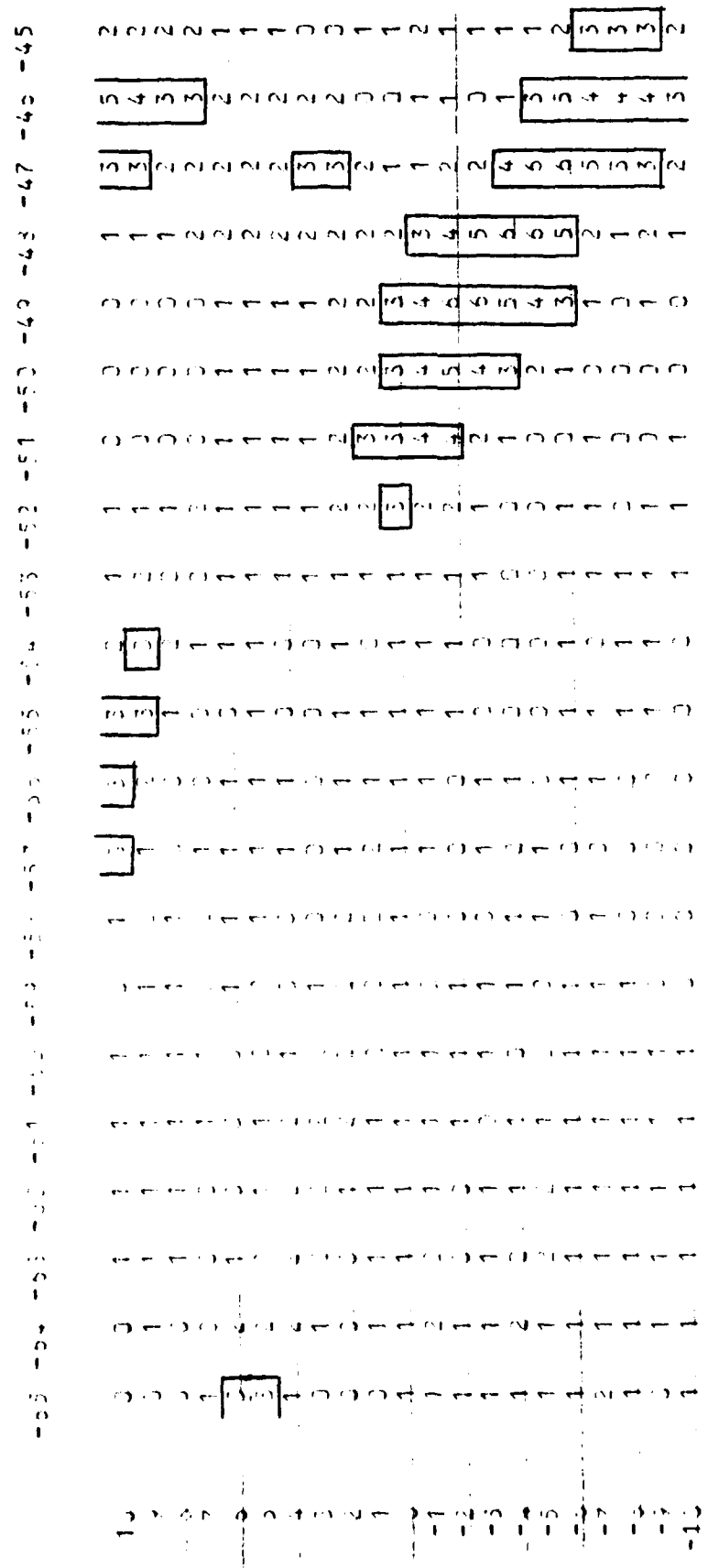
Fig. 29b. As in Fig. 29a, Except North-South Oriented Intervals Are Outlined

(This case has been discussed by Donaldson and Bjerkaas, 1980.[14]) The
data were processed with AFGL equipment. Figs. 30 and 31 show contours of
radial velocity and reflectivity at 1.4° elevation at 2043 local standard
time (LST). We have not applied a power threshold to the velocity data
because, although the signals are weak ahead of the storm (Fig. 31), there
is sufficient coherence for reasonable estimates of the radial velocities.
We want to retain as much velocity information as possible areally, since
gust fronts often occur in regions of very low reflectivity away from the
main storm. Velocities are known to be reliable for signals that are well
below those sufficient for reliable reflectivity estimation if the veloci-
ties are estimated using an autocorrelation technique such as that used by
AFGL.

The gust front is clearly defined in Fig. 30 by the region of
closely spaced contours and has an orientation almost diagonally (southwest
to northeast) across the figure. The front is not marked by a continuous
zero velocity contour, as is most often observed. It has segments that are
aligned both along the radar beam and across the beam. The segments that
are aligned along the beam provide a good test for the "shear-weighted
range."

a. Application of Radial Shear-Weighted Range Algorithm

Fig. 32 depicts shear regions in excess of S_{th} = 2 X $10^{-3}s^{-1}$ at
2043 LST. The contour labelled 20.0 corresponds to 2 X $10^{-3}s^{-1}$ and the
contour interval is 2 X $10^{-3}s^{-1}$. These are radial shears computed accord-
ing to Eq. (1) and Eq. (2) with n = 2, m = 7, and Δr = 150 m. It is obvi-
ous that there are gaps in the shears where the front is oriented along the
beam. A lower S_{th} of $10^{-3}s^{-1}$ (corresponding figure not shown) does not fill
in the gaps but instead makes the shear fields appear much noisier. On the
other hand higher values of S_{th}, such as 3 X $10^{-3}s^{-1}$ (not shown), remove
many of the smaller undesirable features but also remove more of the detec-
ted frontal structure.

Fig. 33 shows R_{sw} locations computed from the shears in Fig. 32.
The minimum number of gates acceptable, k, was set at 5. Each R_{sw} is

---

14. Donaldson, R. J., Jr., and C. Bjerkaas, 1980: Gust front
structure observed by Doppler radar. Preprints, 19th Conference on Radar
Meteorology (Miami Beach), American Meteorological Society, 157-161.
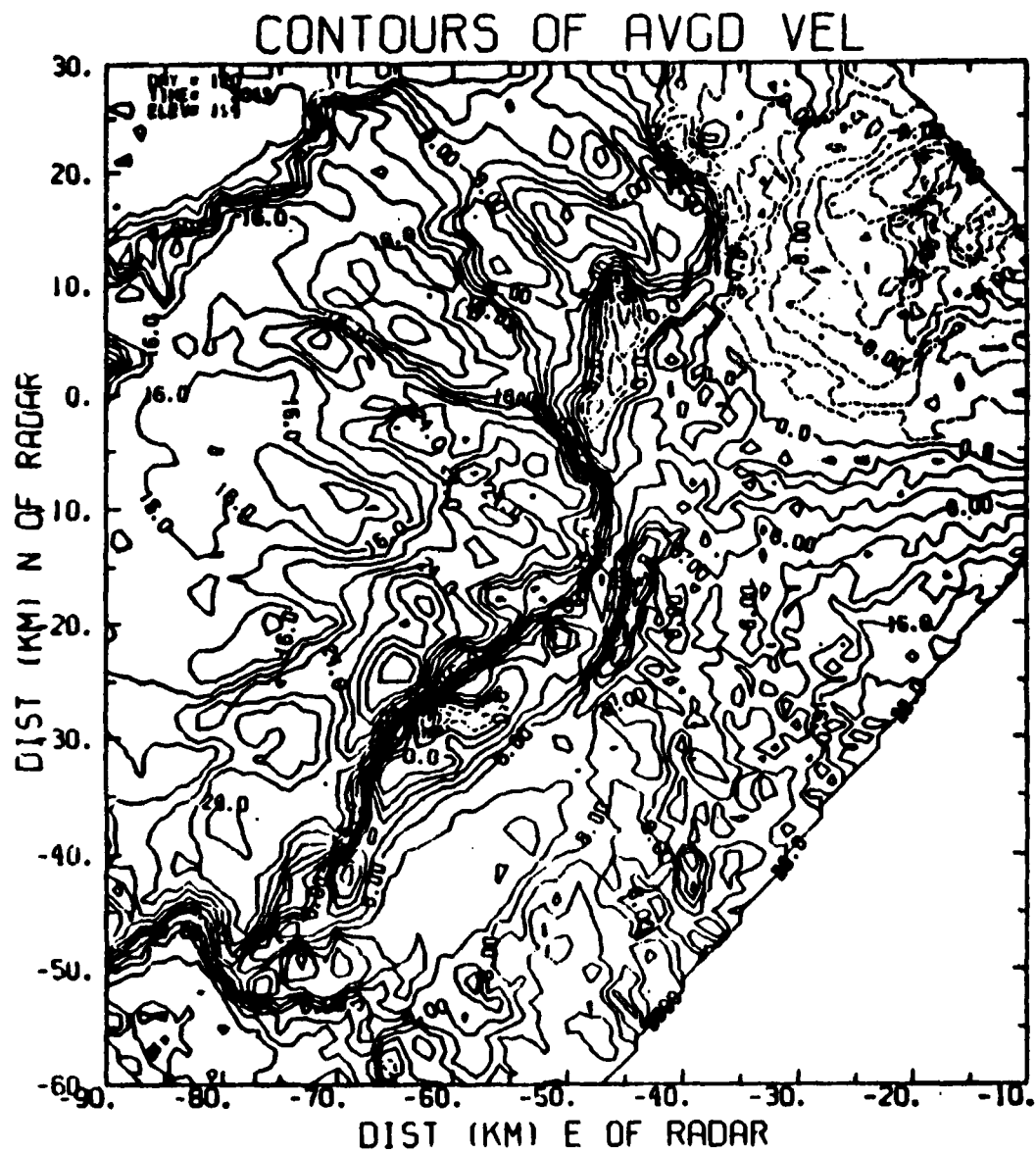
Fig. 30. Average Velocities in ms^{-1} from 30 Apr 78 scan 2043 LST, Elevation 1.4°

CONTOURS OF DBZ
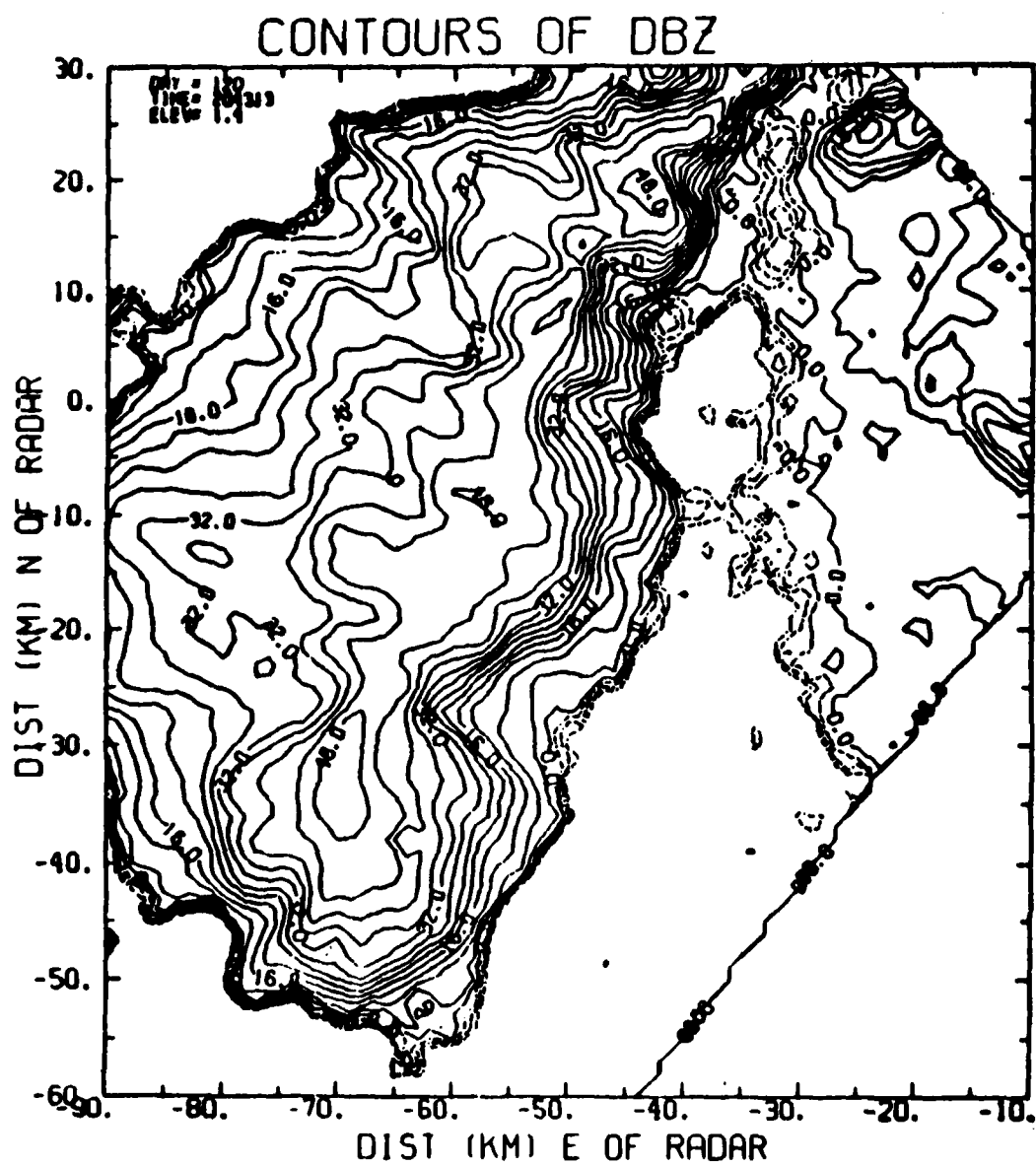
Fig. 31. As in Fig. 30 Except Average Reflectivities in dBZ

CONTOURS OF DIFF VEL
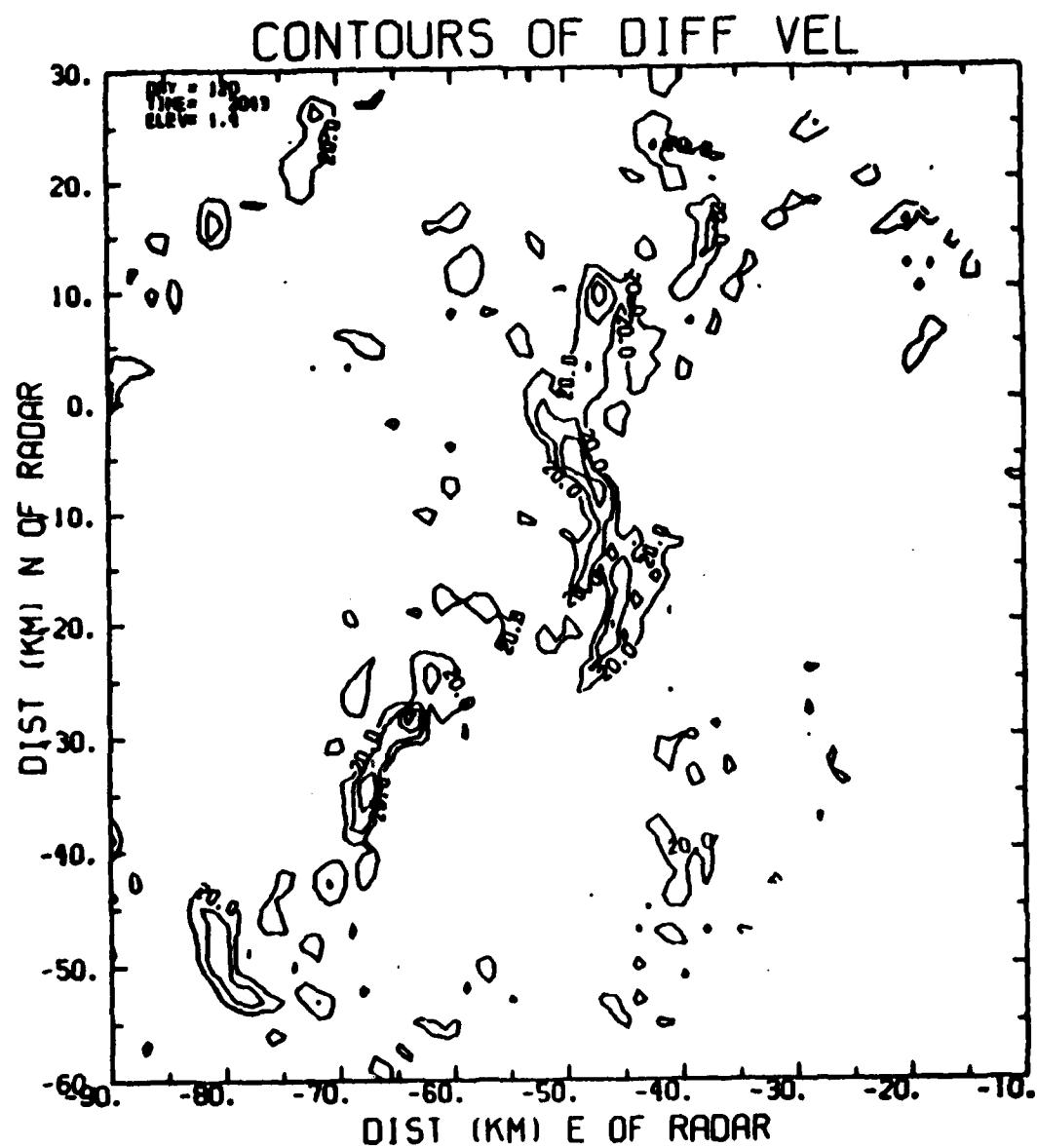
Fig. 32. As in Fig. 30 Except Radial Shears

The 20.0 contour corresponds to shear of $2 \times 10^{-3} s^{-1}$; all contours at $2 \times 10^{-3} s^{-1}$ intervals.
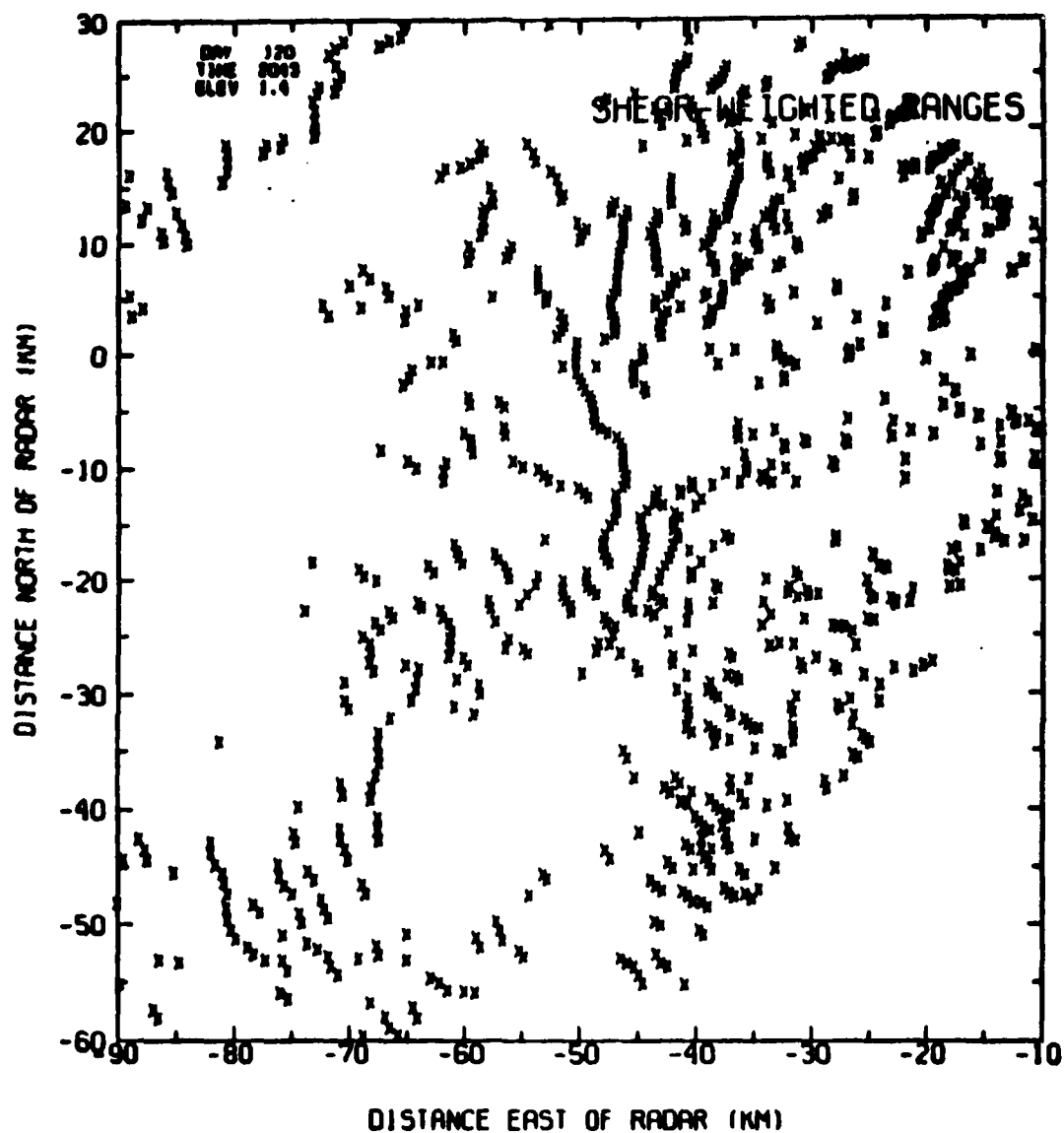
Fig. 33. As in Fig. 30, Except Shear-Weighted Ranges

"X's" mark location of shear-weighted ranges.

represented by an "X." The contours in Fig. 32 result from the application of an exponential interpolation filter with a radius of influence of 1 km that transforms the data to rectangular grid points spaced 1 km apart. This filtering accounts for less noise in Fig. 32 than in Fig. 33. If we compare Fig. 32 with Fig. 33 at (-52,0) km, we see that the line of R_{sw}'s does not follow either branch of strong shears northward, but instead seems to find points midway between the outer edges of the two branches. This can be attributed to the threshold being too low to allow distinction between the two features.

Results of the azimuthal association scheme are shown in Fig. 34. Only those R_{sw}'s that have been found to meet the association criteria mentioned in Section 2 appear. Associated R_{sw}'s are joined by lines. Much of the frontal shear structure remains intact. However, some undesirable artifacts of the technique are present. The feature near (-62, -25) km is not aligned with the front, but instead crosses it. This is due to R_{sw} intervals being oriented along the front.

From the discussion so far in this section, it is quite evident that radial shear alone will not adequately define a gust front. Instead it appears that both tangential and radial shears must be used. We present next a discussion of the results from the second algorithm which does utilize both components.

b. Application of the Total Radial Shear-Weighted Coordinate Algorithm

Fig. 35 depicts total shears computed as described in Section 2 for 2043 LST at 1.4° elevation. The radius r_I is 1.5 km and the threshold S_{Tth} is $2.5 \times 10^{-3} s^{-1}$. The lowest contour in the figure, 25.0, corresponds to S_{Tth} and contour intervals are at $2.5 \times 10^{-3} s^{-1}$. At this threshold the front is a continuous shear feature. The addition of tangential shear has resulted in the gap at (-50, -20) km in Fig. 32 being filled. The structure along the southwestern boundary of the storm now also exhibits some continuity. Much of the noise in the clear air ahead of the front and in the ground clutter that was prevalent in the first algorithm (reference Fig. 33) has been eliminated by averaging tangential and radial shears independently before computing absolute values.

In Fig. 36 "shear-weighted coordinates" are superimposed on total shear contours. The threshold here, was raised to $3 \times 10^{-3} s^{-1}$ in order

73
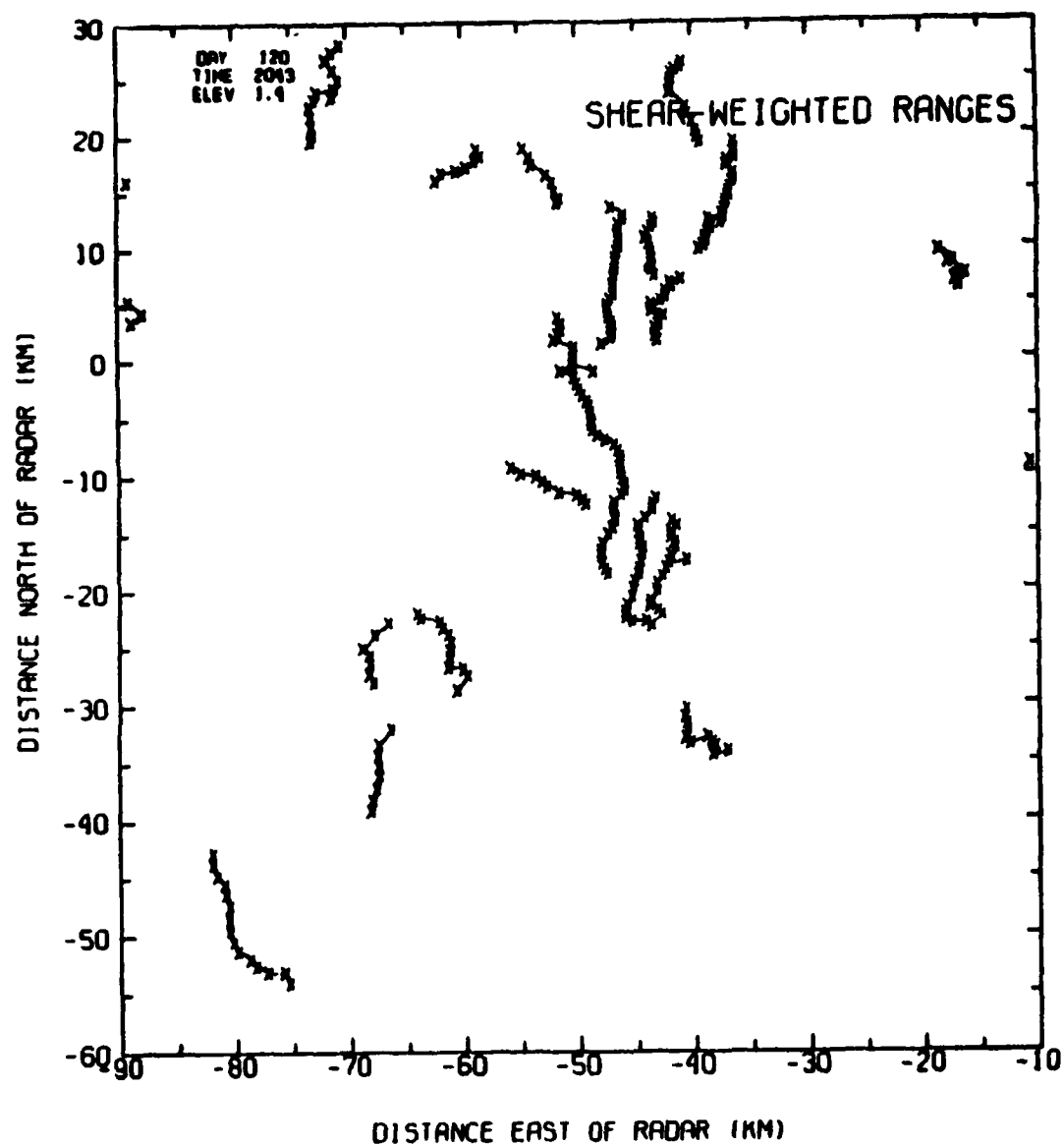
Fig. 34. As in Fig. 33, Except Associated Shear-Weighted Ranges

74

CONTOURS OF TOTL SHR
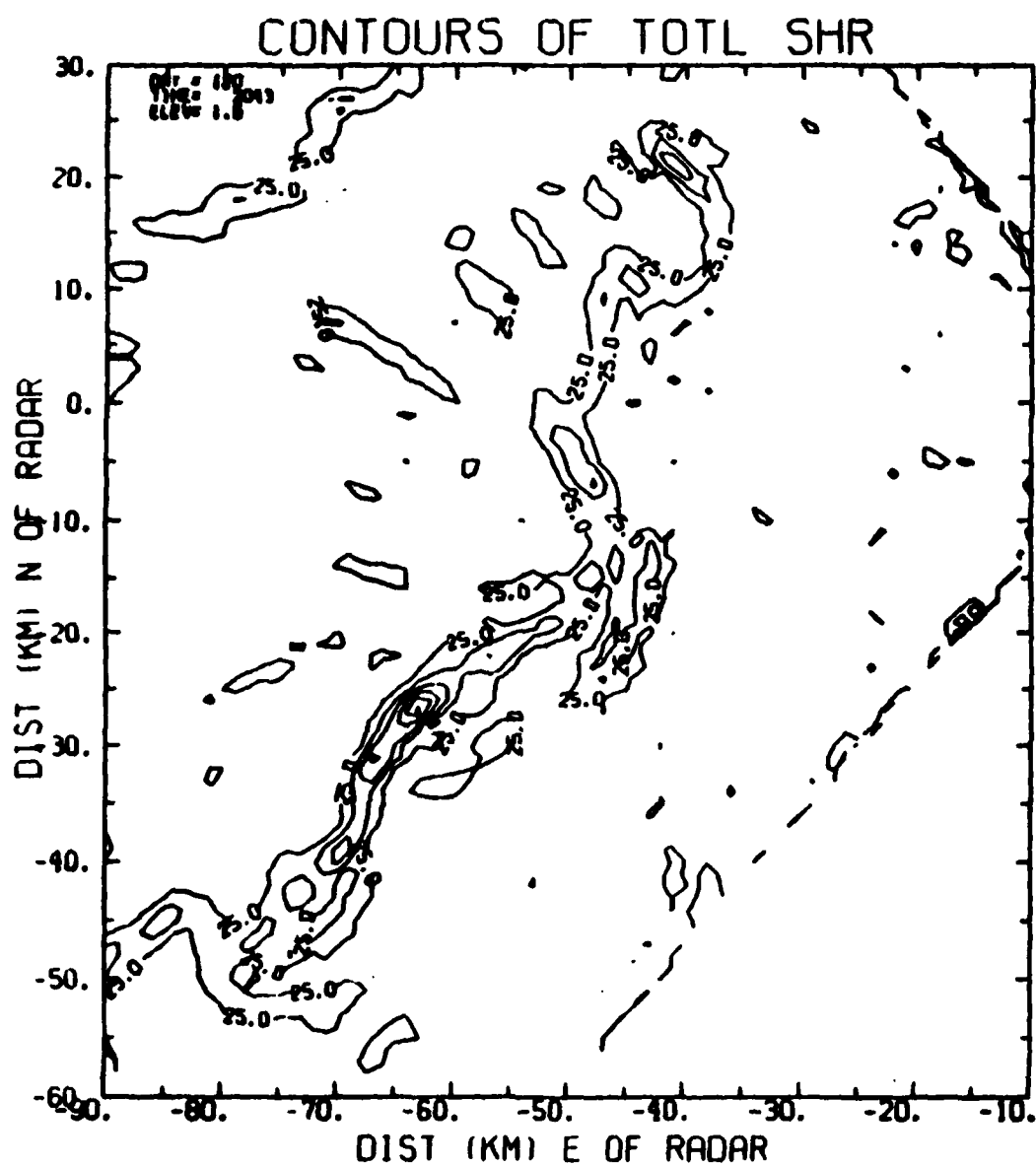
Fig. 35. As in Fig. 30, Except Total Shear

The 25.0 contour corresponds to 2.5 X $10^{-3}s^{-1}$; contours at intervals of 2.5 X $10^{-3}s^{-1}$.
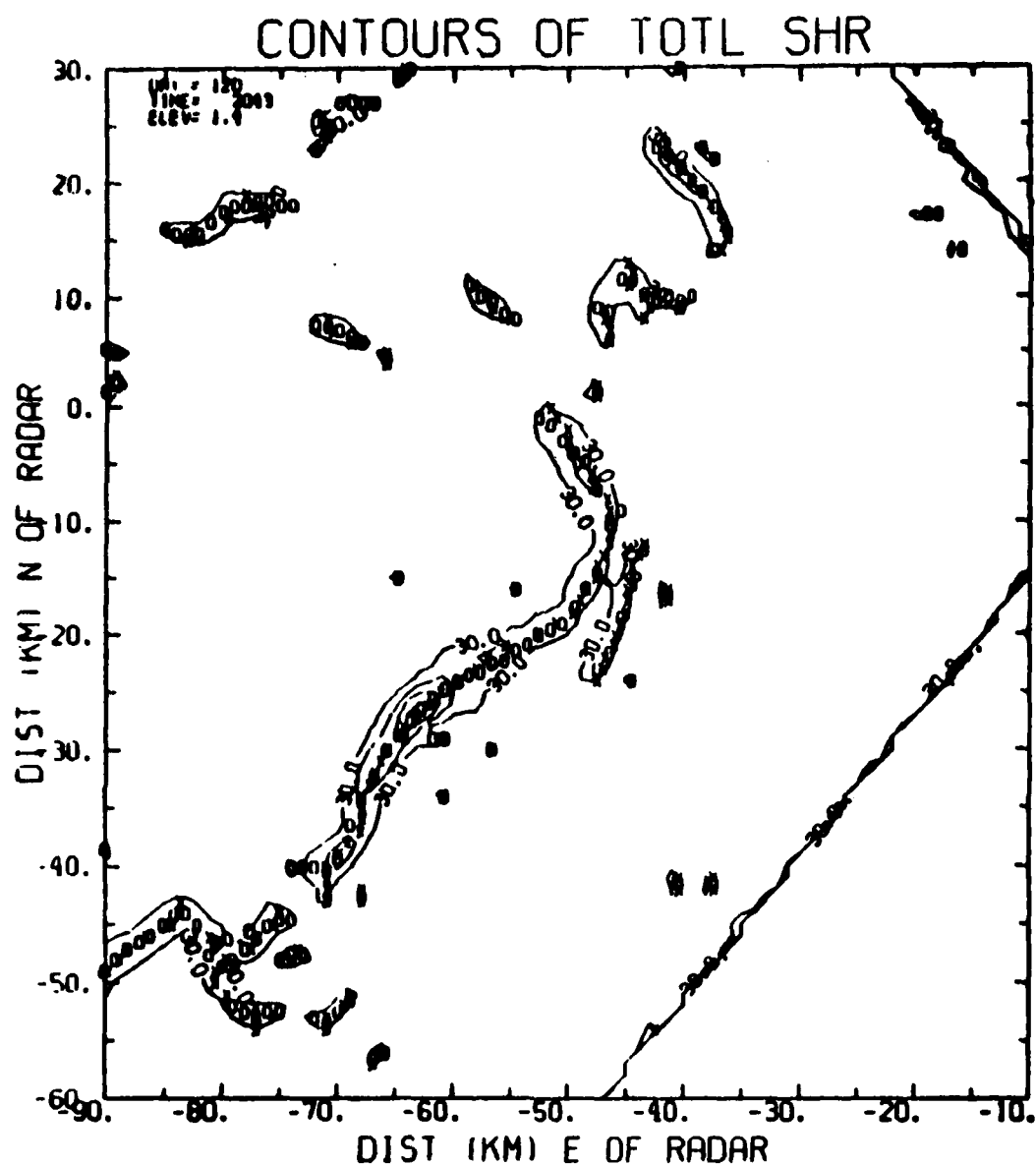
Fig. 36. As in Fig. 30, Except Total Shears and Shear-Weighted Co-
ordinates

The 30.0 contour corresponds to $3 \times 10^{-3}s^{-1}$; "X's" corre-
spond to east-west oriented shear-weighting; "O's" correspond to north-
south oriented shear weighting.

to eliminate most of the extraneous features such as the fingerlike struc-
tures associated with downdrafts within the storm while retaining as much
of the gust front structure as possible. As can be seen, the shear-
weighting performs very well. The X's which result from east-west shear
intervals are in close proximity to the O's which are from intervals ori-
ented north-south. The front is delineated clearly by either the shear
contours or the curve formed by the "shear-weighted coordinates."

4. Summary of Detection Algorithm

An algorithm for detecting gust front shear by radar was presented
in two versions. The first version used only radial shear and performed
reasonably well in detecting segments of gust fronts oriented perpendicular
to the radar beam but could not detect shear regions oriented along the
beam. The second version combined radial and tangential shears and de-
tected shear regions with any orientation most satisfactorily. Further
testing is still required since only one data set was used in this phase of
the study.

5. Discussion of Methods for Tracking Regions of Shear

One important requirement of NEXRAD is to be able to predict the
temporal and spatial evolution of shear regions. Charba (1974)[15] and
others attempted to show that the outflow from a thunderstorm might be a
gravity-density current type of phenomenon. Wakimoto (1982)[16] used the
density current model in conjunction with soundings and Doppler radar mea-
surements to deduce the propagation speed of several gust fronts. These,
however, required knowledge of densities on both sides of the front.
Smythe and Zrnic' (1983)[17] used a correlation technique to deduce

---

15. Charba, J., 1974: Application of gravity current model to
analysis of squall-line gust front. Mon. Wea. Rev., 102, 140-156.

16. Wakimoto, R. M., 1982: The life cycle of thunderstorm gust
fronts as viewed with Doppler radar and rawinsonde data. Mon. Wea. Rev.,
110, 1060-1082.

17. Smythe, G. R., and D. S. Zrnic', 1983: Correlation analysis of
Doppler radar data and retrieval of the horizontal wind. J. Clim. Appl.
Meteor., 22, 297-311.

motions of features in clear air. However, we conducted a cursory examina-
tion of the temporal changes in the velocities and shears associated with
the gust front and found that the features are evolving much too quickly
for correlation to properly identify them in successive scans. We are
unaware of any other attempts in the literature to track shear features
with characteristics similar to gust fronts. Therefore, since these tech-
niques are inappropriate for our data, we seek a method that will enable
determination of motion of shear regions and use it to predict future
motion.

In Fig. 30 we see that just ahead of the front and centered near
(-43,-20) km is a region of high shear. This region is relatively new as
there are much weaker velocity gradients in the previous scan (2037 LST,
not shown). It appears to intensify even further and elongate in the next
successive scans (the scan at 2055 is shown in Fig. 37) and is moving with
a velocity that is more westerly and higher in magnitude than the velocity
of the southern part of the front. This region appears to join with the
northern part of the front and move with a speed in excess of 19 ms^{-1}.
Examination of the reflectivity fields (not shown) at successive scans
indicates that the leading edge of the storm seems to move with the same
velocities as the front. This may be indicative of the line-echo-
wavepattern (LEWP) described by Nolen (1959).[18]

It is obvious that not all points along a gust front move at the
same speed or in the same direction. One of our ideas suggests that these
points may move in the direction normal to the front where it is defined by
a curve connecting the shear-weighted points. If the front does propagate
in this manner, then a line normal to the front can be drawn to determine
if the line intersects a curve in the next scan. The distance between
points divided by the elapsed time would then give an estimate of the prop-
agation speed of a small segment of the front.

This phase of the algorithm is still in the planning stages. This
algorithm and alternatives will be tested and results will be presented in
a future report.

----

18. Nolen, R. H., 1959: A radar pattern associated with torna-
does. Bull. Amer. Meteor. Soc., 40, 277-279.

CONTOURS OF AVGD VEL

DIST (KM) N OF RADAR

DIST (KM) E OF RADAR
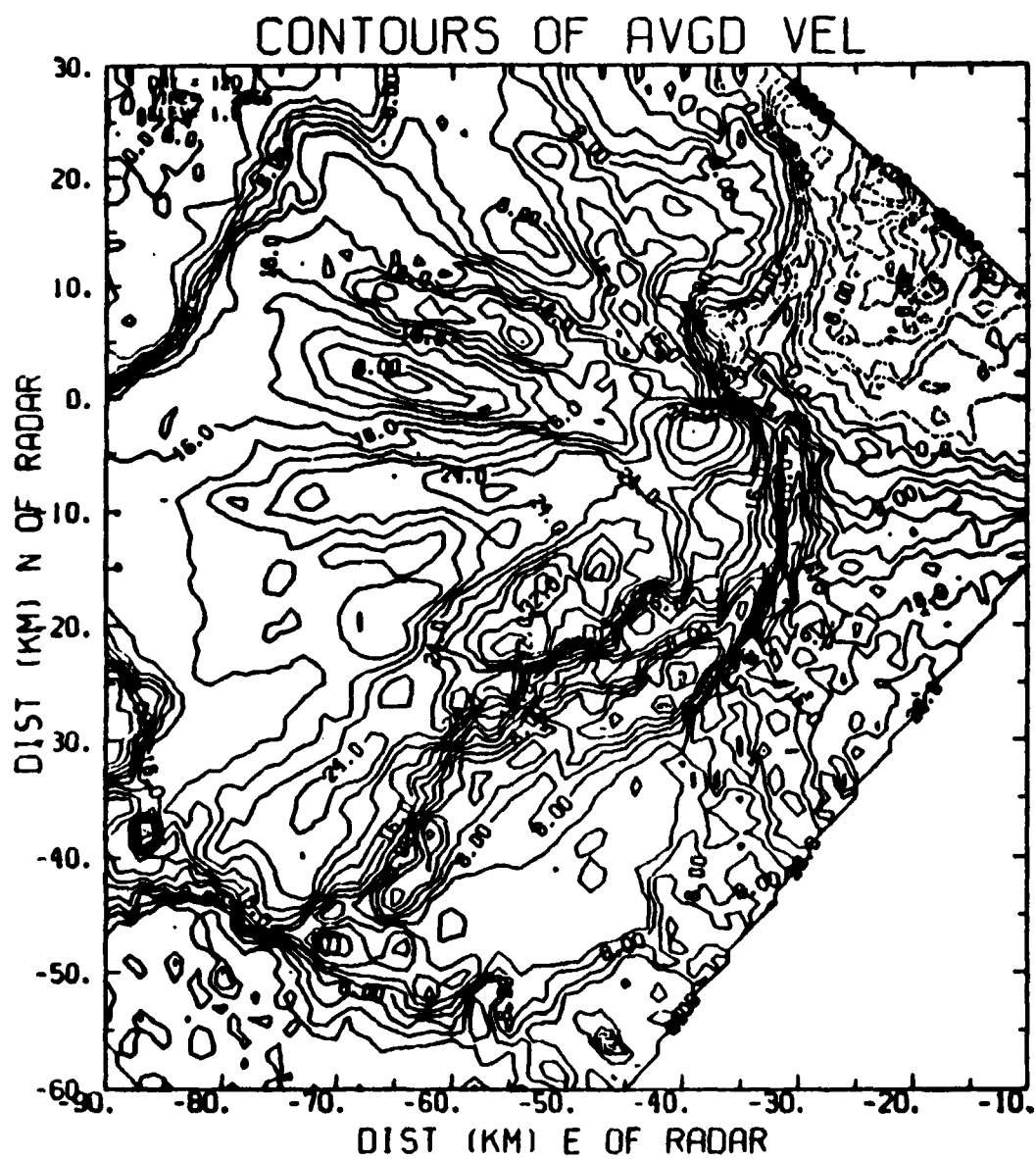
Fig. 37. As in Fig. 30, Except 2055 LST

B. Mesocyclone Detection

Mesocyclones are radar detectable circulations within severe thunderstorms that are often associated with concurrent or potential tornadic activity. In 1984 the mesocyclone detection algorithm described by Wieler and Donaldson (1983)[19] was further developed and integrated into the Modular Radar Analysis Software System (MRASS) (Forsyth et al., 1981).[20] The Mesocyclone/Tornado vortex signature Detection Algorithm (MTDA) is capable of detecting mesocyclones, meso-anticyclones, and cyclonic and anticyclonic tornado vortex signatures. The algorithm is based on resolution-dependent shear and velocity thresholds that enable it to account for the radar beam broadening with range. Thus, the algorithm can identify shear at long ranges without triggering false alarms close to the radar. The MTDA also detects convergent and divergent velocity signatures and their heights, to give a better indication of the severity and the evolutionary stage of the shear features. The algorithm categorizes shear features into eight types: asymmetric shear, convergent, divergent, couplet, mesocyclone, meso-anticyclone, tornado vortex signature, and anticyclonic tornado vortex signature.

The reader is referred to Wieler (1984)[21] for a complete description of the MTDA. The test results from the MTDA are encouraging, as comparisons of the algorithm output with ground truth data are excellent. When compared to other algorithms the MTDA identified features earlier and found them to have greater temporal persistence.

The MTDA was run with favorable results during the Boston Area NEXRAD Demonstration (BAND), and is fully operational within MRASS.

This task has been completed.

---

19. Wieler, J. G., and R. J. Donaldson, Jr., 1983: Mesocyclone detection and classification algorithm. Preprints, 13th Conference on Severe Local Storms, AMS, Boston, 58-61.

20. Forsyth, D. E., C. L. Bjerkaas, and P. Petrocchi, 1981: Modular Radar Analysis Software System (MRASS). Preprints, 20th Conferer on Radar Meteorology, AMS, Boston, 696-699.

21. Wieler, J. G., 1984: Real-time Automated Detection of Mesocyclone and Tornado Vortex Signatures. AFGL-TR-84-0282, Contract F19628-82-C-0023, Systems and Applied Sciences Corporation.

C. Detection of Mesocyclone Precursors

The technique developed by SASC for automatically detecting mesocyclones (see Section B, above) provides as much as 35 minutes lead time for a tornadic event. However, since the storms that produce tornadoes are usually very well developed by the time the mesocyclones are first detected, we believe that there may well be indicators prior to the mesocyclones that would give even greater advance warnings. Donaldson and Snapp (1983)[22] detected convergence and rotation in the motions of radar echoes relative to each other at least 30 min before the mesocyclone, giving on the order of 1 h lead time to a potential tornado touchdown. Since the Donaldson and Snapp study was performed manually, the next step was to attempt to automate their techniques for NEXRAD-type operations. A report of such an effort is contained in Harris and Petrocchi (1984).[23] A brief summary of that report follows.

A peak detection scheme like that of Crane (1976)[24] was developed to monitor the cellular behavior of convective structures. The algorithm was configured so as to be adaptable to a real time operation although there was no attempt to make the software efficient enough to operate truly in real time. Using this algorithm we were able to detect the significant internal cellular structure and to develop two indicators of severe storm development; namely, the number of cells and the average reflectivity mass within the cells as a function of time. Distinct signatures were determined for these parameters for one intense tornadic storm that would

---

22. Donaldson, R. J., Jr., and M. Snapp, 1983: Interstorm motion as a mesocyclone precursor. *Preprints*, 21st Conference on Radar Meteorology, Amer. Meteor. Soc., Boston, MA, pp. 7-10.

23. Harris, F. I., and P. Petrocchi, 1984: *Automated Cell Detection As a Mesocyclone Precursor Tool*. AFGL-TR-84-0266, Air Force Geophysics Laboratory, Hanscom AFB, MA.

24. Crane, R. K., 1976: *Radar Detection of Thunderstorm Hazards for Air Traffic Control, Vol. 1, Storm Detection*. Proj. Rpt. ATC-67-67, Vol. 1, MIT Lincoln Lab, Lexington, MA, FAA-RD-76-52, ADA032732.

have given some additional warning (about 15 to 20 min) over the mesocy-clone detection algorithm (Wieler, 1984).[21] More importantly, there may well be indication in these parameters of the development of a supercell storm and hence the development of an extremely severe storm; in this case, one producing a maxi-tornado and several smaller tornadoes. Data processed for a storm producing only a funnel cloud did not display the same charac-teristics.

Attempts were made at tracking these cells in order to compute con-vergence and vorticity following Donaldson and Snapp.[22] However, during the period of interest there were too many cells and their lifetimes were too short to allow reliable automated tracking.

SASC has terminated its efforts on this endeavor and has turned over to AFGL/LYR an evaluation report and all software. It is recommended that the software be applied to data from other severe storm cases so as to better assess the transferability of the algorithm.

D. Detection of Synoptic-Scale Wind Anomalies

In a widespread field of precipitation Dopper radar data can provide fairly accurate estimates of wind velocity in a horizontal plane. The method requires a scan of an entire circle around the radar at constant elevation angle and constant range. The resultant record of Doppler velo-city as a function of azimuth angle is called a velocity-azimuth display, or VAD. Lhermitte and Atlas (1961)[25] showed that the VAD is a simple sine wave if the wind is uniform everywhere on the scanning circle, with the azimuthal location of the sine wave peak and its magnitude indicating the direction and speed of the wind.

Since variability of the wind in space as well as time, rather than uniformity, is the general rule in the real atmosphere, the VAD pattern in such a wind field deviates somewhat from a simple sine wave. However, it

_____

25. Lhermitte, R. M.., and D. Atlas, 1961: Precipitation motion by pulse Doppler. Proceedings, 9th Weather Radar Conference, Amer. Meteor. Soc., Boston, MA, 218-223.

makes sense to measure a mean value of wind around the radar scanning circle. Browning and Wexler (1968)[26] provide a general analysis technique for the VAD that is valid whether or not the wind is uniform all around the scanning circle. Their technique uses a harmonic analysis of the Doppler pattern, with the amplitude and phase of the first harmonic indicating speed and direction of the mean wind observed by the radar.

Wind information can be obtained at all altitudes populated by suitable tracers, and as frequently as the radar completes a cycle of elevation scans -- generally within 10 min. The best data are available precisely where most needed, in stormy weather. When the NEXRAD system of Doppler radars becomes operational, upper air wind information in precipitation can be acquired with nearly a two order of magnitude refinement in time resolution over the current 12 h updates provided by radiosondes. This improvement should be a significant aid to forecasters for determining trends in the development and motion of synoptic-scale cyclones.

The Doppler VAD pattern indicates not only mean wind velocity, but also higher order anomalies that reveal gradients in wind speed and directional changes expressible as curvature. These higher order features of the wind field should significantly enhance the utility of the mean wind for forecasting storms on the synoptic scale. Also, the evaluation of gradients and curvature offers a means for monitoring off-shore storms of dangerous intensity, such as hurricanes and severe extra-tropical cyclones.

The problem was approached by examination of the Doppler velocity patterns that would be observed in a few simple wind field models. The analysis technique and its results and implications were discussed in detail by Donaldson and Harris (1984)[27] (referred to hereafter as D + H). A brief summary of it follows.

26. Browning, K. A., and R. Wexler, 1968: The determination of kinematic properties of a wind field using Dopper radar. _J. Appl. Meteor._, _7_, 105-113.

27. Donaldson, R. J., Jr., and F. I. Harris, 1984: Detection of wind field curvature and wind speed gradients by a single Doppler radar. _Preprints_, 22nd Conference on Radar Meteorology, Amer. Meteor. Soc., Boston, MA, 514-519.

Two types of wind models were considered: circular flow around a fixed center of curvature with constant speed, and linear flow with constant speed gradients both along and normal to the flow. The gradient along the wind is the stretching deformation and the crosswind gradient is the shearing deformation. In the VAD pattern, the gradient along the wind is easy to recognize and evaluate. It is the difference in magnitude between the downwind maximum and the upwind minimum velocities, divided by the diameter of the VAD scanning circle. If the extrema appear to be contaminated by higher order terms, they may be obtained by splitting the VAD into upwind and downwind halves according to a procedure discussed in D + H.

The VAD patterns for linear flow with a crosswind speed gradient and for circular flow with uniform speed are similar in appearance. The general type of VAD pattern produced by either one of these two wind field models is illustrated in Fig. 38. The figure shows the VAD scanning circle with radius r. The winds are moving generally from left to right, although there are also components normal to this general motion in the case with circular flow. The dotted line indicates the locus of zero Doppler velocity ($V_D = 0$), where wind direction is normal to the radar beam, for all scanning circles with radii intermediate between 0 and r. The dashed line, on the other hand, indicates the locus of the Doppler velocity extrema (conventionally, minimum upwind and maximum downwind) for scanning circles of any radius between 0 and r. If the wind were uniform throughout the scanning circle, the dashed line would be straight and normal to the dotted line, and the two extrema would be opposite, separated by the angle π. In the depicted case, however, the minimum and maximum Doppler velocities are each displaced an angle δ toward the solid arrowhead, so that the angle between the extrema is now $\pi - 2\delta$. For the circular wind field, the solid arrowhead points toward the center of curvature, and in the case with crosswind speed gradient it points in the direction of maximum increase of speed.

Expressions for the Doppler velocities at any point on the radar scanning circle were derived by D + H for the model circular and crosswind gradient flows (stated in their Eqs. (5) and (10), respectively). From these expressions the angular locations of the extrema were found; these indicate the δ angles depicted in Fig. 38 (Eqs. (6) and (11) of D + H).
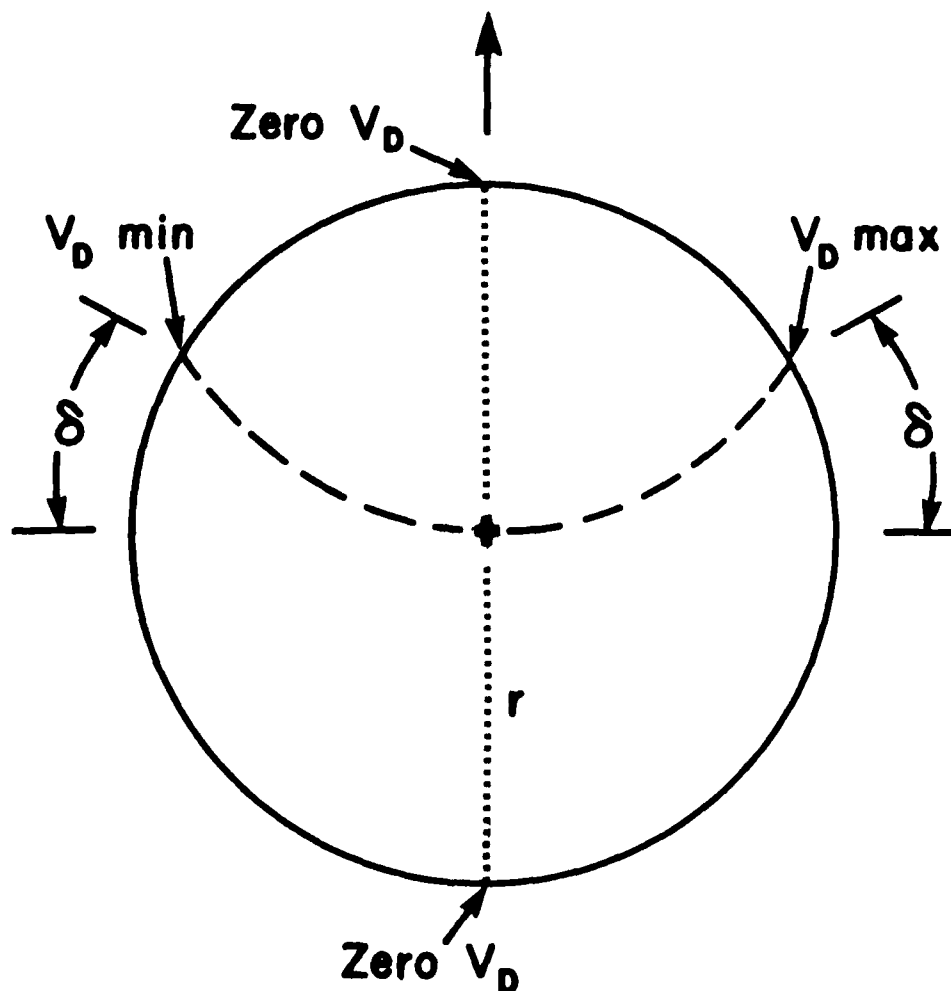
Fig. 38. Key Features of the Velocity-Azimuth Display of an Asymmetric Wind
         Field

       Radius of radar scanning circle is r; for all radii intermediate
between 0 and r, dotted line indicates locus of zero Doppler velocity; dashed
line is locus of Doppler velocity extrema, which are displaced by angle δ in
the direction of arrowhead.

In both model flows, the δ angles are dependent not only on the characteristics of the wind field but also on the radius r of the scanning circle. An increase in wind field curvature or in its cross-flow gradient will be indicated by a larger δ angle, and in a given wind field an increase in r will also increase the δ angle, but with opposite sign of the slope of increase for the two wind field types. Since r is under human control, at least within a range where reflective wind tracers are present, this contrasting behavior of the δ - r function suggests a means for distinguishing the two wind field types from one another. As a practical matter, however, differences are indistinguishable at δ angles less than 10°, although at 20° and beyond the differences are striking.

Another technique, called the Quad Ratio, was investigated as a possible means for identification and apportionment of the two wind field types. The Quad Ratio is the summation of the magnitude of all Doppler velocity measurements in the quadrant centered about the bisector of π - 2δ (the solid arrowhead in Fig. 38), divided by the corresponding summation in the opposite quadrant. There is practically no difference in Quad Ratio for the two wind field models at δ angles less than 10°, but at a δ angle of 20° there is a 23 percent difference which increases rapidly with further increase in δ angle.

There is a more serious difficulty, however, in identification of wind field type: rarely would one be present without the other. In D + H a general model of circular wind field combined with crosswind gradient was analyzed, with resultant Doppler velocity expressed in Eq. (15) and a complex function relating δ, r, and the wind field parameters stated in Eq. (16). With some information from a source outside the capability of a single Doppler radar, for example, satellite observations of curvature around a hurricane, Eq. (16) could be used to estimate the crosswind gradient.

Another approach suggested by D + H is acceptance of the ambiguity between curvature and shear, recognizing that both wind types are indicative of the proximity and intensity of a cyclone. For example, an increase in δ angle, keeping radar parameters fixed, signifies greater curvature of the wind field attending the approach of a cyclone center, as well as increased gradient of wind speed toward the center. In either case, if an off-shore hurricane or intense extra-tropical storm is under radar

surveillance, the magnitude of its δ angle can serve as a threat index, with the direction of the $\pi - 2\delta$ bisector pointing toward the center of the cyclone. A cyclonic intensity indicator was proposed, equal to V_0 sin δ/r, where V_0 is the mean wind speed measured at the radar and r, as before, is the radius of the VAD scanning circle. This indicator is either the vorticity of a circular wind field, or the product of cos 2δ and the crosswind speed gradient of a linear wind field, or more likely a combination of both. In summary, there is a significant operational utility for analysis of the asymmetric component of a VAD pattern, despite its kinematic ambiguity.

Following the preparation of the D + H paper, work on asymmetric VAD patterns continued in an effort to develop an optimal technique to distinguish a circular wind field from a cross-sheared linear wind, and to explore the limits of applicability of this technique. A theoretical distinction between the two wind field types was found. A linear wind field with a constant crosswind gradient has only first and second harmonics. On the other hand, a circularly curved wind field with constant speed has third and higher harmonics, as well as harmonics of first and second order. Accordingly, ratios of third and fourth to second harmonics were calculated as a function of δ angle for the curved wind field.

It was recognized that small-scale perturbations and waves may also contribute to the magnitude of third and higher order harmonics. Accordingly, simple smoothing functions consisting of running means of various lengths were tested but found to be ineffective for suppressing the relative magnitudes of harmonic distortions created by small-scale perturbations. This technique, which seemed initially promising, proved to be disappointing.

Nevertheless, the fundamental difference in the presence of higher harmonics in the two model wind fields encouraged further investigation. Therefore, a different approach was tried: subtraction of zeroth, first, and second harmonics from the VAD pattern eliminates deformation and leaves only third and higher harmonics which are due to curvature and perturbations. Calculation of the Quad Ratio of this remainder may suppress most of the perturbational effects and enable an estimate of the contribution of curvature to the originally observed VAD pattern. The averaging required in the Quad Ratio would tend to average out third and higher order

87

harmonics not related to the asymmetry inherent in wind field curvature.

In principle, a linear wind field with variable cross-flow shear could have a Doppler VAD pattern which exactly mimics the pattern for circularly-curved flow. A numerical solution was found for this circularly-mimic shear. Varying as a function of azimuth angle, this shear has four sign reversals and two infinite poles, and hence is highly implausible from a meteorological viewpoint. Therefore, efforts to discriminate and apportion curvature from shear in asymmetric VAD patterns are validated. Refinement of the most promising technique is planned. Also, these theoretical results will be applied to observational data and tested whenever possible.

E. Icing Detection

1. Introduction

The accumulation of ice on an aircraft in flight can have dire consequences. Icing may drastically alter aircraft performance and has caused numerous fatal accidents (National Transportation Safety Board, 1981).[28] While icing poses a minor threat to high-altitude flights and de-icer equipped aircraft, it is a critical factor during takeoffs and landings for any aircraft, and poses a major threat to those aircraft restricted to lower altitudes (i.e., below 7 km). These are generally fixed-wing propeller driven aircraft and helicopters without de-icing capability. Additionally, U. S. Air Force aircraft frequently fly at low levels to prevent detection.

Aircraft icing is caused by two basic conditions: 1) the surface temperature of the aircraft is below 0° C, and 2) super-cooled water droplets are present. Water droplets will generally freeze at temperatures between -10° C to -40° C; thus super-cooled water may be present in the atmosphere anywhere between 0° C to -40° C, although the bulk of it will exist at a temperature between 0° C and -10° C.

Currently aircraft icing prediction is based on objective forecasts derived from radiosonde information taken every 12 hours. These objective

---

28. National Transportation Safety Board, 1981: _Safety Report: Aircraft Icing Avoidance and Protection_. NTSB-SR-81-1, National Transportation Safety Board, Washington, D.C., 12pp.

forecasts are usually updated and amended as pilots report icing episodes. Given the frequently severe consequences of icing and the limited spatial and temporal resolution of the radiosonde soundings, it is not surprising that the regions of possible icing are overforecast. SASC is currently investigating the incorporation of radar data in the icing forecast process for inclusion in the NEXRAD program.

Two important icing parameters that can be provided by radar data are the intensity and phase change of the precipitation. It is a well known fact that a layer of melting precipitation in stratiform storm situations produces an associated enhancement of the reflectivity (Ryde, 1946),[29] called the bright band. The reasons for the increase of reflectivity with decreasing height in the bright band are the enhanced growth of the precipitation at temperatures warmer than $-10°$ C and the change of the complex index of refraction of the hydrometeors from that of ice to water at temperatures above $0°$ C. Calculations have shown that this latter effect produces a 6.74 dB increase of reflectivity and should occur by the time one-third of the hydrometeor has melted (Ekpenyong and Srivastava, 1970).[30] Observations show, however, that this increase of reflectivity is generally greater than 7dB, with the additional increase attributable to the enhanced growth of the precipitation alluded to above.

The main process contributing to the decrease of reflectivity below the bright band is the increase of terminal fall velocity of the hydrometeors. Typically, the ratio of fall velocities between a snowflake and

---

29. Ryde, J. W., 1946: The Attenuation and Radar Echoes Produced at Centimetre Wavelengths by Various Meteorological Phenomena. Report of a conference on meteorological factors in radio wave propagation held on 8 April 1946 at The Royal Institution, London. Published by the Physical Society.

30. Ekpenyong, B., and R. Srivastava, 1970: Radar Characteristics of the Melting Layer - A Theoretical Study. University of Chicago, Department of Geophysical Science, and Illinois Institute of Technology, Department of Electrical Engineering, Technical Report No. 16, Laboratory for Atmospheric Probing, Chicago, IL.

a raindrop is about one to five. One can expect an equivalent decrease in
the raindrop concentration. This effect will generally result in a 7 dB
decrease in echo intensity below the peak reflectivity. An additional
decrease in reflectivity can be attributed to the change in size of the
scatterers, since wet snowflakes present much larger cross-sections than
equivalent mass raindrops, and breakup can also be an important process
during the melting stage (e.g., Ohtake, 1981).[31]

As currently proposed, the algorithm may be broken down into five
steps:

    (1)   Input radar reflectivity data;

    (2)   Detect bright bands;

    (3)   Estimate regions of possible icing conditions;

    (4)   Estimate equivalent liquid water content of precipitation
          occurring in possible icing regions;

    (5)   Output estimated icing potential.

2. Algorithm Description

    (1)   Input radar reflectivity data

The algorithm operates on vertical reflectivity profiles; cur-
rently two types of profiles are generated. Both make use of a series of
radials at different elevation angles at constant azimuth. In one method
data corresponding to constant horizontal range are used from each eleva-
tion angle. It is called the single range profile (SRP). The second
method makes use of a series of range cells for each elevation angle that
are horizontally averaged, thus increasing the vertical resolution of the
profile. This profile is called a horizontally averaged profile (HAP). A
distance of 20 km is arbitrarily selected for the horizontal averaging. It
is planned to use a fast Fourier transform to determine the optimum dis-
tance for averaging based on the scale of the features of interest.

---

31. Ohtake, T., 1981: Observations of size distributions of
hydrometeors through the melting layer. J. Atmos. Sci., 26, 545-557.

(2) Detect bright bands

The reflectivity profiles are examined for the presence of a
bright band. A bright band will be indicated if there is a reflectivity
peak at least 7 dB higher than that above and below the peak and the
thickness of this enhanced layer is less than 3 km.

(3) Estimate regions of possible icing

From the bright band reflectivity profile three points are
singled out. First, the algorithm finds the height of the peak reflec-
tivity and then looks for the height above the peak where the reflectivity
is 7 dB lower. This height should give a lower boundary on the possible
height of the 0° C isotherm since 7 dB is the minimum increase of reflec-
tivity one would expect to see once the snowflake has started to melt at
about the 0° C level. Another significant point on the curve is the in-
flection point of the curve above the bright band. This is likely to be
caused by the emergence of aggregation and/or accretion as the primary mode
of growth of the snowflakes that were previously growing by deposition.
This region of enhanced growth usually begins once the temperature in-
creases to about -10° C to -12° C, which may also delineate the region of
more serious icing episodes.

(4) Estimate equivalent liquid water content occurring in possible
     icing regions

Since the algorithm uses the information from the previous step
to find areas that satisfy the first condition for icing, this step esti-
mates the amount of equivalent liquid water content of the precipitation
with the radar. This will be accomplished through the use of one of the
existing radar reflectivity-equivalent liquid water content relationships
for snow, such as that found by Herzegh and Hobbs (1980).[32] The selec-
tion of the optimum relationship to be used requires further testing.

_____

32. Herzegh, P. H., and P. V. Hobbs, 1980: The mesoscale and
microscale structure and organization of clouds and precipitation in
midlatitude cyclones. II. Warm frontal clouds. J. Atmos. Sci., 37,
597-611.

(5) Output estimated icing potential

          Based on information obtained from the reflectivity profile,
including bright band characteristics and liquid water content values, an
icing potential is derived.

3. Analysis

          Radar data collected by the AFGL 10 cm Doppler radar on 5 Apr 84
were used as a case study to do preliminary analysis and testing of the
first three steps of the algorithm. The synoptic situation was dominated
by a warm front to the south of the radar site moving northward with
associated overrunning precipitation. An examination of the 0700 EST
radiosonde observations of that day from Portland, ME, Chatham, MA, and
Albany, NY indicated that the 0° C isotherm was at about 2.4 km. The
algorithm processed data at the 200° azimuth at 1425 EST. The height of
the 0° C isotherm would be expected to change between the time of the
sounding and radar observation due to evaporative cooling from precipita-
tion and warm air advection from the south. Visual observations of the
reflectivity patterns indicated that a bright band did exist and was
particularly pronounced in the southern quadrant.

          Fig. 39 shows the reflectivity profiles generated at 1425 EST with
points of interest noted. The peak reflectivity occurs at 2.1 km. The
height above the peak where the reflectivity is 7 dB less than the peak is
2.39, which compares well with the estimated 0° C height based on the 0700
EST radiosonde soundings. The point of inflection above the peak in the
profile is 2.77 km. This is expected to correspond to the -10° C level;
however, according to the 0700 EST sounding the -10° C isotherm is higher,
approximately 3 - 4 km. Overall, the results from the single range pro-
files show a high degree of variability while the horizontally averaged
profiles are much more consistent with each other.

          The minimum peak detection criteria for the identification of a
bright band are also tested. For the specific case study the criterion
that there must to be a 7 dB decrease in reflectivity below the bright band
appears to be too stringent, as it was met by only two of the twelve single
profile cases and one of the three horizontally averaged profiles. The
other criteria appear to work satisfactorily, although some testing should
be done to determine their validity.
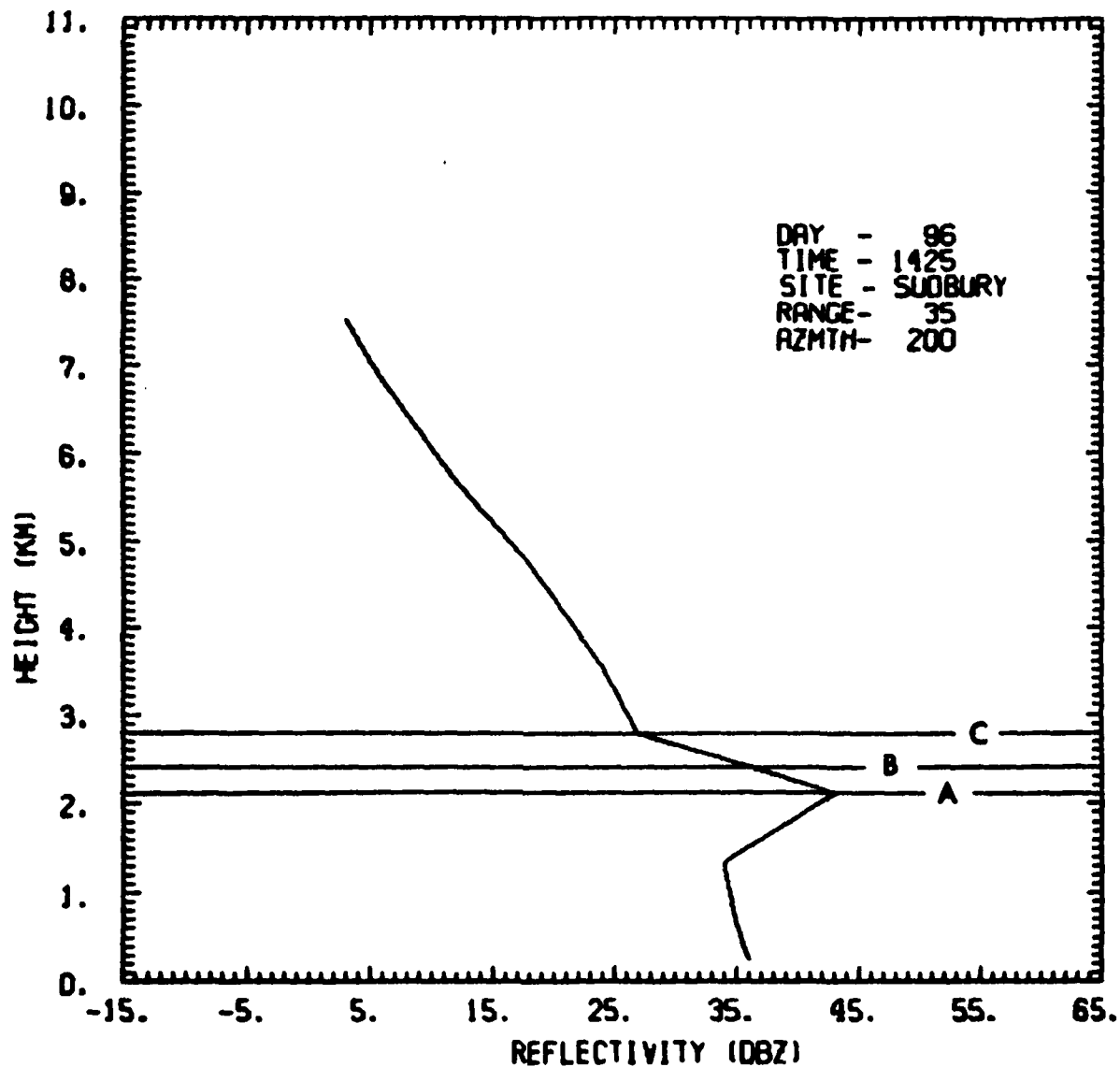
Fig. 39. Reflectivity Profile for 5 Apr 1984

Line A represents height of the bright band peak; line B represents height at which reflectivity is 7 dB less than it was at peak; line C is height of inflection point of curve.

4. Future Work

After all the steps have been implemented and tested, the total algorithm will be fine tuned and tested on data to be collected with the AFGL Doppler radar. Extensive use will be made of pilot reports of icing intensity, cloud base and top heights, precipitation types, and temperature, as ground truth for comparison with the algorithm results.

F. CO_2 Doppler Lidar

1. Introduction

SASC assisted AFGL in the development of a mobile coherent pulsed Doppler CO_2 lidar system designed to evaluate techniques for the acquisition and real time interpretation of atmospheric wind field structure, as well as for aerosol attenuation and concentrations over long path lengths. SASC participation was terminated at end-FY84.

2. Trailer Preparation

Trailer preparations for installation of the laser and data processing systems were nearly completed. Installation of the RFI shielding for the partition separating the laser and data processing sections of the trailer was finished.

Installation of the SASC designed shock mounted electronic rack slides to the trailer floor was completed by AFGL/SUT according to drawings prepared by SASC. The slides will allow the laser control and data processing electronics racks to be easily pulled away from the trailer walls for servicing while also providing protection from severe shock and vibrations during transport to field locations.

Installation of all wiring raceways, air ducts, and lighting by the AFGL shops was completed under SASC surveillance.

AFGL electricians began final installation of the interior power cabling according to plans submitted by SASC.

3. CO_2 Laser System

Assembly of the local oscillator and injection low pressure CO_2 lasers was completed and operational testing was begun. The output power of the lasers was within predicted levels, and all wavelengths in the 9 and

10 micron bands were accessible. Changes in the grating mounts and inser-
tion of intra-cavity apertures helped to reduce output power fluctuations.
In addition, assembly and testing of the dual pyroelectric detector unit
for the frequency control of the lasers was completed.

Engineering plans for the manifold distribution system of the heat
exchanger as well as wiring plans for the flowswitch interlocks were
finished.

The TEA laser control electronics modifications were completed and
preparations were begun for a final check of the system prior to the begin-
ning of operational tests in the laboratory.

V. SATELLITE METEOROLOGY

A. Satellite-Manually Digitized Radar Feasibility Study

A combined SASC/AFGL study was undertaken to determine the feasibility of estimating Manually Digitized Radar[33] (MDR) indices from geosynchronous satellite imagery for cases of moderate to deep convection (M/DC) and MDR grid-scale dimensions.

The approach to data handling was viewed as a two-phase process. Phase one, described in Gerlach (1982),[34] identified and archived the MDR, visible, and infrared (IR) data sets for days and regions of M/DC. Visible and IR digital data from the GOES-East satellite were obtained from the cassette archive of McIDAS. The MDR data extracted from the high speed FAA WB604 line were decoded and stored by McIDAS. Phase two was to process cases selected from the archive. The initial processing procedure under phase two, detailed in Gerlach (1983),[4] stored and managed cases in a three-dimensional frequency distribution, derived frequency fields based on individual (maximum) value and area-averaging techniques, provided the capability to compress (i.e., combine brightness and IR temperature categories) the frequency distributions to facilitate analysis and interpretation, and computed exceedence probabilities for display as a two-dimensional distribution. This report covers the final processing effort under phase two and outlines the follow-on analysis.

Analysis of the echo/no echo probability distributions computed from the six compressed frequency distribution files revealed that non-zero MDR values were mainly confined to a smaller subset of brightness and IR values. To eliminate data void areas additional software was developed as a

---

33. Anon., 1979: National Weather Service Radar Code Users Guide. National Weather Service, National Oceanic and Atmospheric Administration, U. S. Department of Commerce, Silver Spring, MD.

34. Gerlach, A. M., ed., 1982: Objective Analysis and Prediction Techniques. AFGL-TR-82-0394, Contract F19628-82-C-0023, Systems and Applied Sciences Corporation, pp. 217-226, ADA131465.

new option to FRQDIS to combine brightness and IR temperature categories that define these areas, and reduce the distribution size from 20 X 84 to 6 X 7. Fig. 40 is a listing of the frequency distribution for MDR plane coordinate 2 (D/VIP level 1) and individual pixel data as a result of compression. The brightness categories of 17-20 have been separately retained while categories 15-16 and 1-14 are combined. IR temperatures have been merged into 10° C bins ranging between -5° C and -55° C with extrema categories at each end of the distribution. This second step in distribution compression was applied to all six disk files. Frequency and percent relative frequency listings of individual MDR planes were produced with the PSQ option of PRBDIS and occurrence values from selected visible-IR intersections were verified from hand calculations using 20 X 84 distribution data.

A new option was also written for PRBDIS to compute exceedence probabilities for each compressed visible-IR intersection representing the echo/no echo probability, and probabilities of successively higher echo intensities, to produce a listing of the exceedence probability distribution formatted for a single printout page. Fig. 41 is the exceedence probability distribution for the individual pixel data. Note that for each compressed visible-IR intersection, the exceedence probabilities increasing D/VIP thresholds are presented in compact format. For example, the probability of MDR values at the intersection V = 17 and IR = 25.0° C to -34.9° C is: 1 or greater, 78 percent; 2 or greater, 44 percent; 3 or greater, 13 percent; 4 or greater, 4 percent; and 5 or greater, 2 percent. The a posteriori exceedence probability distribution for the developmental sample (computed from the distribution of processed cases) is: 1 or greater, 77 percent; 2 or greater, 5 percent; 3 or greater, 20 percent; 4 or greater, 10 percent; and 5 or greater, 3 percent. The category labeled "Night Only" depicts the probability distribution of MDR values based solely on IR temperature. It represents the potential use of geosynchronous satellite imagery for nightime applications when visible imagery is not available.

The data sample used in this study yielded the exceedence probability distribution mentioned above. In the absence of satellite data that distribution would represent the a posteriori basis of MDR occurrence during conditions favorable to M/DC. In evaluating the information available in satellite IR temperature measurements, the full sample distribution was

SATELLITE BRIGHTNESS CATEGORY

IR TEMPERATURE	1 - 14 (0 - .70)	15,16 (.71 - .80)	17 (.81 - .85)	18 (.86 - .90)	19 (.91 - .95)	20 (.96 - 1.0)
>-5.0	10	10	7	2	2	1
-5.0 TO -14.9	6	11	6	10	18	15
-15.0 TO -24.9	5	16	15	25	29	29
-25.0 TO -34.9	5	27	15	24	25	31
-35.0 TO -44.9	14	60	41	51	77	57
-45.0 TO -54.9	0	25	41	63	86	91
< -54.9	0	1	7	6	29	61

Fig. 40. Compressed Frequency Distribution as a Function of Satellite Brightness and IR Temperature Categories

98

SATELLITE BRIGHTNESS CATEGORY

IR TEMP	1 - 14 (0-.70)	15,16 (.71 -.80)	17 (.81-.85)	18 (.86-.90)	19 (.91-.95)	20 (.96-1.0)	NIGHT ONLY
> -5.0	53 43 17 / 6 2	54 43 22 / 6 1	71 56 27 / 15 2	38 29 5 / 5 0	65 53 29 / 18 0	44 33 11 / 0 0	56 44 20 / 8 1
-5.0 TO -14.9	48 19 10 / 5 0	57 34 11 / 2 0	60 43 17 / 3 3	74 47 13 / 5 0	76 29 13 / 0 0	69 38 13 / 6 0	65 36 13 / 4 0
-15.0 TO -24.9	47 32 6 / 3 0	36 48 19 / 10 5	80 51 18 / 8 2	79 35 16 / 9 2	81 26 11 / 6 0	78 48 13 / 1 0	77 41 14 / 5 1
-25.0 TO -34.9	61 45 24 / 6 3	69 37 15 / 10 3	78 44 13 / 4 2	77 42 14 / 4 1	76 44 12 / 1 1	88 55 11 / 2 0	76 45 14 / 5 2
-35.0 TO -44.9	69 33 10 / 3 0	73 27 10 / 5 2	78 37 17 / 5 1	77 44 9 / 4 1	85 42 10 / 6 2	77 49 19 / 12 2	78 41 13 / 7 1
-45.0 TO -54.9	59 59 41 / 24 0	66 38 22 / 7 3	85 45 13 / 6 2	86 50 15 / 6 1	82 52 13 / 4 1	83 59 21 / 10 2	81 52 18 / 7 2
< -54.9	20 20 20 / 20 0	64 55 27 / 18 0	81 54 23 / 12 4	67 56 22 / 11 2	75 60 27 / 14 6	82 74 39 / 24 10	80 69 35 / 21 8

Fig. 41. Compressed Percent Probability Distribution as a Function of Satellite Brightness and IR Temperature Categories

Percentages represent exceedence probabilities for MDR D/VIP Level 1 or higher (top left value), Level 2 or higher (top middle value), ..., Level 5 or higher (bottom right value).

used as the basis of comparison. Plots of the MDR exceedence probability distribution (based on the categories of IR temperature shown in Fig. 41) were generated for individual pixel data, and 5 percent, 15 percent, and 25 percent area-averaged pixel data. Examining these plots revealed that the main effect of area-averaging on the probability distributions is to increase the discrimination between the significant MDR events (D/VIP level 3 or higher) and less significant events for the two coldest IR categories. The overall effect of area-averaging is shown in Fig. 42. The cumulative departures from the full sample distribution (in percentage points) are shown as a function of IR temperature categories. That is, the percentage value is computed by summing the differences between the appropriate IR category distribution and full sample distribution at each D/VIP threshold. The data in Fig. 42 suggest that 15 percent area-averaging, which corresponds to cloud masses of 22 km equivalent cloud diameter, yielded the maximum discrimination. In other words, it increased the exceedence probability distribution for the coldest IR temperatures and decreased the probability distribution for the warmer IR temperatures more than the other methods.

In large-scale weather systems favoring M/DC, cloud covered regions with IR temperatures colder than $-45°$ C have a considerably greater probability of precipitation intensity corresponding to D/VIP levels 1 and greater than do similar regions with IR temperatures warmer than $-45°$ C. In cloud covered areas with IR temperatures warmer than $-45°$ C, the visible channel would have to be considered in order to deviate from the a posteriori exceedence probability distribution.

The next step in the analysis, based on the conclusions reached above, was to determine the additive value of visible imagery under daytime conditions. The analysis focused on 15 percent area-averaged pixel data. Within each IR temperature category the sample distribution was used as the basis for determining the increase in information due to the visible data. Again plots of the MDR exceedence probability distribution (based on visible and IR categories in Fig. 41 and stratified according to IR category) were produced for analysis. In those cases of IR temperatures warmer than $-15°$ C the visible data did not enhance discrimination, so that departures from the "Night Only" distribution were generally inconsistent with what would be expected. That is, the brighter the cloud mass, the greater
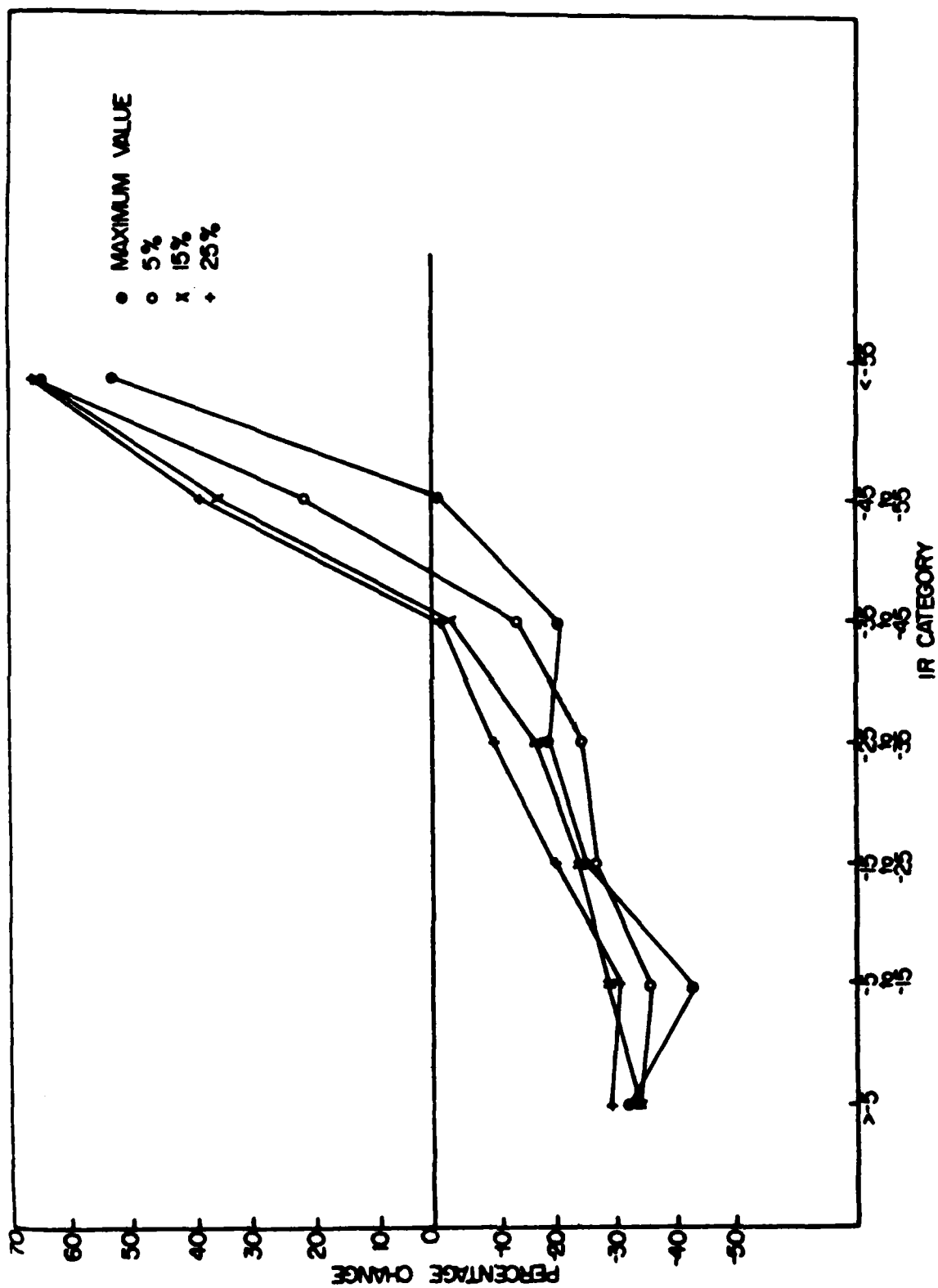
Fig. 42. Cumulative Departure from the A Posteriori Exceedence Probability Distribution for Each Processing Method, as a Function of IR Temperature Categories

the probability of higher MDR events for a given range of IR temperature. Cole and Kantor (1978)[35] found that during summer months over temperate land masses, convective cloud-top temperatures warmer than -15° C are typically found in the 4 to 7 km altitude range. Thus, cases found at these visible and IR temperature categories define convective clouds in early stages of development that are reaching varying levels of internal development as deduced from radar reflectivity.

For IR temperatures colder than -15° C, discrimination of significant MDR events from lesser events becomes more pronounced, peaking at IR temperatures between -35° C and -55° C. Fig. 43 shows the overall discrimination effect in which the cumulative departures from the "Night Only" distributions are depicted as a function of visible brightness categories for the five coldest IR categories. The coldest IR category (IR < -55° C) deviates from the warmer IR categories in degrading the discrimination at the higher end of brightness categories. This is most likely due to the formation of optically-thick thunderstorm anvils that have penetrated the tropopause and spread (due to vertical wind shear factors) into MDR boxes just downwind of the precipitation-generating cells.[36] In the warmer IR categories, the probability of significant MDR events increases substantially in areas where cloud-top brightness values are larger. It is this range of visible brightness and IR temperature values that typically represents the active regions of convective systems to be located where precipitation is most pronounced.

Results of the analysis indicate that the use of only IR data improved specification of precipitation probability (corresponding to MDR D/VIP levels 1 and above) over the a posteriori exceedence probability for IR temperatures colder than -45° C. The addition of visible brightness data contributed to improved specification of precipitation probability above and beyond specification based on IR temperature alone, primarily in

---

35. Cole, A. E., and A. J. Kantor, 1978: Air Force Reference Atmospheres. AFGL-TR-78-0051, Air Force Geophysics Laboratory, Hanscom AFB, MA, ADA058505.

36. Scofield, R. A., and V. J. Oliver, 1977: A Scheme for Estimating Convective Rainfall from Satellite Imagery. NOAA Tech. Memo. NESS No. 86, NTIS PB-270 762/861.
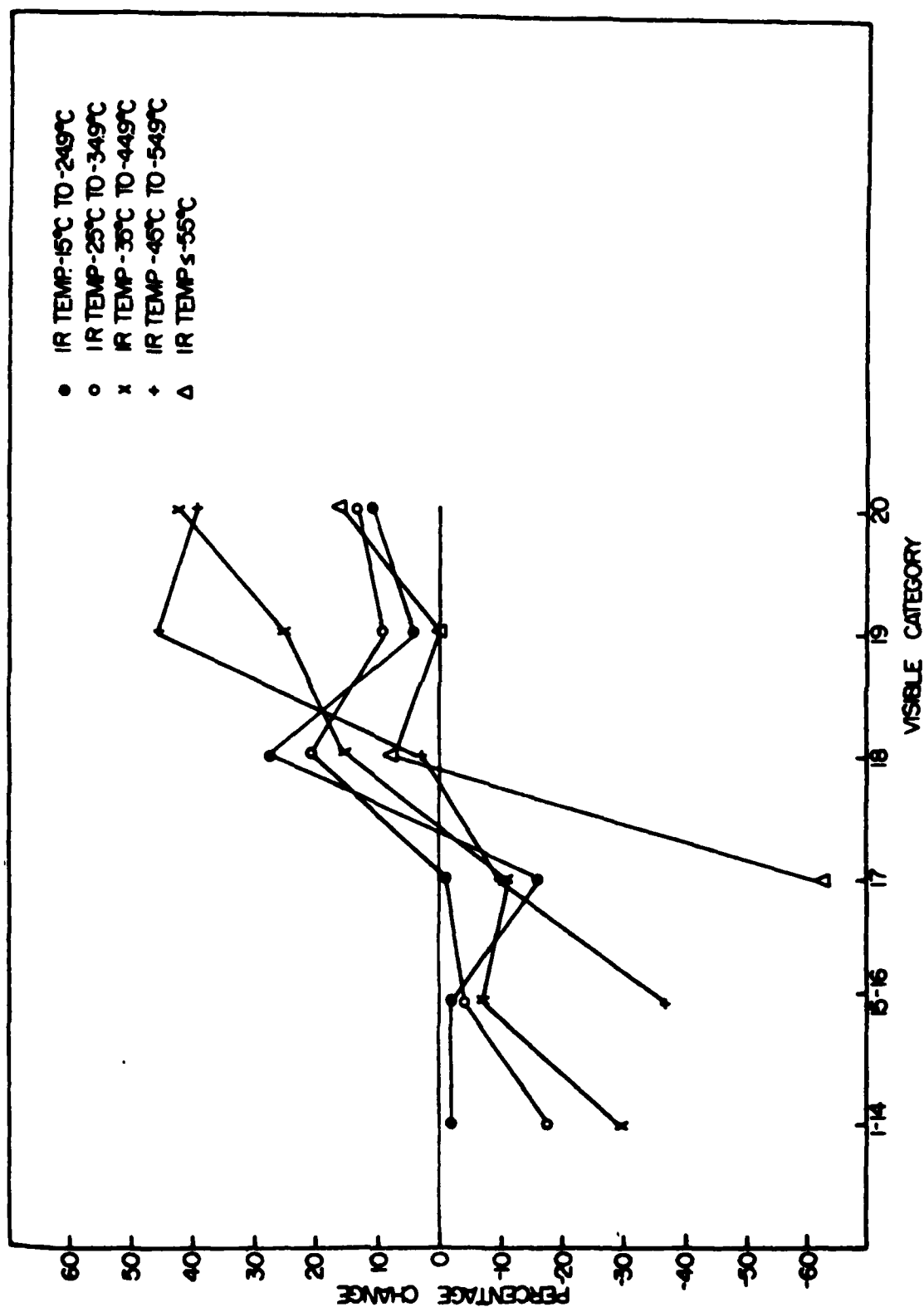
Fig. 43. Cumulative Departure from the Overall Distribution of the Specified IR Temperature Category for the Fifteen Percent Area-Averaging Method, as a Function of Brightness Categories

regions with IR cloud-top temperatures colder than -15° C. At colder IR temperatures increased probabilities could only be shown for corresponding brightness values of 18 or greater (reflectivity > 0.85); values below 18 yielded probabilities lower than the "Night Only" distribution. The analysis suggests that there is valuable information concerning MDR precipitation characteristics that can be inferred from area-averaged geosynchronous satellite imagery. This information could prove useful for a number of applications concerned with precipitation-bearing cloud systems associated with M/DC for geographical areas comparable in size to the grid dimensions used in this study.

B. Microprocessor-Based Satellite Data Ingest System

1. Introduction

Under a contractual agreement between the National Oceanic and Atmospheric Administration and AFGL, a redundant data path in the AFGL GOES mode A ground station is being made available to a consortium of users known as the Northeast Area Remote Sensing System (NEARSS). Included in the agreement is a requirement to develop a central processing facility to ingest, store, and transmit over a dedicated communication network subsets of the GOES imagery transmission. To satisfy this requirement an Intel 8086-based microprocessor with fixed disk mass storage was purchased and assembled. AFGL personnel developed software for the task and configured the central processor. SASC software engineers participated in various phases of the software system specification and development as described in Gerlach (1983)[4] and completed development and coding of individual tasks.

This report details the work accomplished as a coordinated SASC/AFGL effort including extensive testing of developed applications software under a number of iRMX 86 operating system configurations, specification of the NEARSS communication network format, development of a communication network manager, and development of system software in support of hardware component configuration and integration.

2. Software Testing

The Intel In-Circuit-Emulator (ICE) was evaluated during early stages of software testing to determine its utility in simulating the

operating environment of the microprocessor-based ingest system. The ICE, which emulates an 8086 CPU, is designed to aid in the debugging process by providing commands for controlled instruction execution, setting of execution break points, and examination of registers, memory locations, and programmer-defined variables at any point during execution. This allows for line by line testing of routines for logic and programming errors. Several subroutines were tested in this manner, showing the ICE to be valuable for non-real time simulations but of little value in debugging techniques for intertask communication, memory management, and interrupt handling, all of which are critical to the process of data ingest. Testing of these techniques required the configuration of a test system including an operating system debugger. Consequently, a limited configuration of iRMX86 consisting of the operating system nucleus containing the routines for intertask communication, interrupt handling, and memory management; the operating system extension for a terminal handler and debugger; and a single user job incorporating the most important system calls used by the ingest software was decided upon for the test system. Configuration is a multi-step process of selecting the required portions of the iRMX86 operating system, specifying the parameters defining the hardware environment, assembling system routines and data files, linking these assembled routines with library routines, and locating the linked routines in memory.

The first test systems configured with the Intel Interactive Configuration Utility (ICU), an interactive screen-based configuration tool, consisted of simple tasks to accept typed input from a terminal keyboard and output messages to the terminal CRT. These routines were then replaced by the formal terminal processing modules TTYTTY and THOUTPUT, which are designed to execute in the operating environment of the target system. Configuration of these modules into the test system permitted testing of intertask and interjob communication and initiation of directed tasks. A concurrently executing scheduler routine was later included to increase system complexity and to allow one to examine the operating system's priority-based multitasking capability. Configurations were normally down-loaded from development system memory and initiated with the iSBC 957B iAPX 86,88 Interface and Execution Package, vendor-supplied firmware consisting of a loader to perform memory to memory transfers and a monitor that supports interactive commands for memory management. Fatal errors

incurred during execution of the test system were monitored by the iRMX 86 Debugger, a diagnostic software tool containing its own terminal handler and providing error type and location information. Because the Debugger is sensitive to the data structures of the nucleus and allows one to monitor system activity without interfering in execution, the test system could be debugged in a multitasking and intertask communication environment. These features also allow one to verify at run-time that the logic assumptions made in the use of operating system primitives are correct.

3. Network Communications and Management

The primary function of the microprocessor-based ingest system is to provide NEARSS members and users with GOES mode A satellite data on a near real time basis. For this reason it was decided in the design phase that regardless of future enhancements to the network, GOES imagery transmissions would take priority. Based on the geographical coverage desired by NEARSS, the way in which the GOES satellite senses the data, and the prototype receiver site hardware specifications, it was decided to provide visible and infrared imagery with a resolution of 8 km per picture element (pixel) and an image size of 480 X 480 pixels or approximately .25 megabytes (MB) of 8-bit data. Initially there will be 0.25 MB infrared and visible imagery available from AFGL every half hour during daylight hours and infrared data only at night. The design of GOES ingest software will allow for higher resolution visible imagery and more extensive geographical coverage if NEARSS requirements should change. With a 9600 bit/sec transmission rate, it will take approximately 7 min to transmit an infrared and visible pair if uninterrupted. Higher resolution visible data and/or extended geographical coverage could increase transmission time considerably.

In order to transfer imagery data effectively from one electronic data processor to another, a set of defined procedures known as protocols needs to be specified and then accepted among users of the network as a set of rules governing all network communications. The NEARSS protocol has been defined as an asynchronous bit-oriented protocol (BOP). It will be transmitted synchronously over a leased, conditioned carrier line using a modem in full duplex. The protocol is labelled asynchronous because it allows the central site to broadcast data at random times without prior notification to the receiving sites. Taking into consideration the 8-bit

106

radiance measurement precision of the GOES infrared sensor and the 8-bit maximum character length for synchronous transmission, the BOP structure was adopted to insure that the full dynamic range of the infrared sensor would be available. (The BOP does not require use of a partioned character set to effect the orderly operation of the data link, but attains control through structuring inherent in the protocol. Byte control protocols (BCP's) limit the range of data in sub-fields because they require control characters as part of the data link.) Fig. 44 illustrates the general format of the NEARSS protocol. Based upon the volume of GOES data that will be transmitted over the network, it was decided that synchronous vs. asynchronous transmission was more suitable (synchronous transmissions are approximately 20 percent more efficient because they do not require start and stop bits to synchronize the transmitter and receiver).

Because of the flexibility of the protocol, design steps were taken to implement inter-user communication among various user sites in the initial system. Protocol formats and procedures were defined early on that would allow users on the network to exchange text and data but no software existed to maintain network integrity. To meet this need a network manager was developed to direct the flow of traffic over the network by exercising its ability to transmit and receive both control and data/text protocols to and from the network. This software is designed to maximize throughput on the network and maintain a transparent existence to all users. Users gain access to the network via a polling procedure controlled and conducted by the manager.

To verify control and data protocol construction by the manager as a response to received protocols, a test system was developed to software simulate a primitive network environment. Existing modules controlling operator communications through the terminal CRT (user site) were modified to accept and decode typed ASCII protocols. Additional software was written to encode binary formatted protocols transferred from the manager (central site) via intertask and interjob communication (network link) prior to display of the generated protocol at the terminal CRT.

SOH	PROTOCOL TYPE	INFO TYPE	SITE ID	BYTE	COUNT	BCED	INFO SECTION	BCED	ISED	EOT
byte	byte	byte	byte	word		byte	byte(s)	byte	byte	byte	byte

where,

SOH — Start of protocol transmission (byte).

PROTOCOL TYPE — Distinguishes between control and data (or test) protocol (byte).

PROTOCOL TYPE	SIGNIFICANCE
2	Text, GOES mode A or non-GOES data protocols.
5	Control protocols.

INFO TYPE — Defines the type of information (if any) in the INFO SECTION (byte).

SITE ID — Identification number (ID) of a NEARSS user site (byte).

BYTE COUNT — Number of bytes in the INFO SECTION (word). First byte is high order byte while second byte is low order byte of the BYTE COUNT word.

BCED — Byte count error detection, checksum (byte).

INFO SECTION — Information section of the protocol (byte(s)). It is of variable length and contains text or data.

ISED — Reserved for INFO section error detection (byte).

EOT — End of protocol transmission (byte).

Fig. 44.   General Format of the NEARSS Protocol

108

4. Software Support to Hardware

a. Serial Port Initialization

The Zendex Z-86 SBC was chosen over the Intel 86/30 as the target
computer to take advantage of its more flexible design and its ability to
support two serial ports for terminal and network communications currently
required by NEARSS. Nevertheless, the 86/30 SBC does meet the minimum
requirements of supporting network communications and was judged to be use-
ful under the network testing phase and possibly under the operational
phase if a hardware emergency situation arose. In support of the 86/30,
device drivers to handle the serial port for network communications were
written and debugged. A set of routines written in ASM86, the 8086 assem-
bly language, was developed to handle the initialization of and control
data transfers to/from the 8251A Universal Synchronous Asynchronous Re-
ceiver Transmitter (USART) and the initialization of the timing generator,
the 8253 Programmable Interval Timer (PIT). Initial testing of the USART/
PIT was conducted using polled, asynchronous communications with a CRT
terminal configured for a baud rate of 9600. Subsequent tests involved
using a pair of 1200 baud modems between the CPU and CRT to test the remote
communications aspects critical to the network manager software. Success-
ful testing of the USART/PIT software resulted in its integration into a
version of the network manager for this hardware configuration.

b. Device Drivers

The Intel 215/218 Winchester/Flexible Disk Controller is currently
used as the interface to both the Priam Winchester Hard Disk and Shugart SA
810/860 Diskette Storage Drives. This hardware configuration may be con-
sidered an interim specification if NEARSS requires a more extensive imag-
ery archive that logically would exist on magnetic tape. A Cipher F880
Magnetic Tape Transport, Rimfire 38A Winchester Disk/Tape Controller, and
Central Data Corporation Double-Density Floppy Disk Controller were all
purchased to meet this potential requirement although neither controller is
directly configurable under iRMX86. As a result, efforts have begun to de-
velop device drivers under iRMX86 to support these devices.

With the floppy disk controller, routines to initialize the Western Digital FD1791 controller chip, command it to position the drive head on a desired track, and initiate a read from disk or a write to disk instruction were written and tested under an interim operating system designed to maximize operator control and monitoring. A routine to write pertinent timing, track, and sector identification fields on a blank diskette was also developed as a necessary precursor to all I/O operations. A method of latching the controller's bus buffers and selection circuitry to off-board memory locations to permit Direct Memory Access (DMA) transfers was devised and implemented to free the main processor, the 8086, from the extra task of controlling disk I/O. Successful implementation of these routines led to development of the interrupt handler and I/O start routine required for complete integration of this controller into the iRMX 86 Basic I/O System. Initial testing of the hard disk/tape controller was completed with a routine written in PLM86 to initialize the controller, configure it under the operating specifications of the hard disk, and perform a disk load sequence. Module execution was monitored under the iSBC 957B iAPX 86,88 Interface and Execution Package in order to minimize the time required for software development and implementation.

c. Target System Configuration

During initial test system configurations it became apparent that the development system being used, an Intel MDS800, could not support releases of the assembler, linker, and locater necessary to design an iRMX86 system. To support these utilities the development system was upgraded to an Intel Series III, employing a 16-bit 8086 CPU while retaining the MDS800 8-bit 8080/8085 CPU for I/O operations and supporting communications to a target system via an 8-bit parallel interface. Unfortunately, the development system upgrade did not include the addition of Winchester technology fixed disk mass storage, but instead retained the limited mass storage capabilities of floppy disk used with the MDS800. With the introduction of the ICU, a software package designed to automate many of the steps of configuration and thus reduce configuration time, the need for additional disk space became critical because the ICU requires a substantial amount of disk space not only to access existing files but also to generate temporary and permanent files during the configuration

process. To resolve the problem, the work effort was shifted to provide
the target system, supporting a fixed disk, with a stand-alone development
capability. To achieve that capability three steps were identified. The
first was to introduce a preconfigured operating system capable of pro-
viding an environment conducive to software development. The second step
was to develop and implement in firmware a bootstrap loader essentially to
read-in the operating system from a mass storage device and induce execu-
tion. The third step was to incorporate resources necessary for develop-
ment.

Erasable Programmable Read Only Memory (EPROM) chips were program-
med, installed, tested, and implemented as the iSBC 957B iAPX 88,86 Inter-
face and Execution Package supporting a bootstrap loader. The bootstrap
loader software was programmed on the Universal Prom Programmer using the
Universal Prom Mapper, Intel system software through which all ROM program-
ming functions are initiated. After installation of the EPROM's, the boot-
strap operation was tested with a vendor-supplied floppy diskette contain-
ing a preconfigured iRMX86 boot-ready file. The preconfigured operating
system is a fully-layered version of iRMX86, designed to support a variety
of applications programming and configuration tools in a software develop-
ment environment. This version also contains a number of interactive pro-
grams that perform volume and file management, system management, and
general utility functions. Backup copies of the preconfigured operating
system were generated on both floppy and hard disk. Language translators,
programming utilities, and system configuration utilities were added to the
system from diskettes purchased from Intel and in some cases from existing
files previously used on the development system.

d. Summary

Operator communications and automated scheduling software were sub-
jected to extensive testing under various configurations of the iRMX86
operating system. The specifications for a communication network were com-
pleted; based on those specifications, a network manager was developed and
subjected to initial testing. Finally, system software was developed and
implemented in support of hardware component configuration and integra-
tion.

C. Experimental Cloud Analysis Program

1. Introduction

AFGL is involved in a research effort to improve the Air Force automated nephanalysis model known as RTNEPH (see Gerlach, 1982[34] and 1983[4]). An integral part of the RTNEPH is an IR thresholding cloud detection algorithm. Primary inputs to the cloud algorithm are measurements, from polar orbiting meteorological satellites, of upwelling infrared radiant flux converted to equivalent blackbody brightness temperatures. Brightness temperature values are compared to coincident surface skin temperature estimates that are primarily derived from ground based shelter temperature measurements. Clouds are assumed to exist in regions where satellite observed temperatures are colder than surface temperatures by an amount greater than an empirical threshold. The accuracy of this technique depends to a large degree on the accuracy of the satellite brightness temperatures. As a part of the cloud analysis project SASC participated in a study undertaken to determine if a bias, related to satellite viewing angle, exists in the IR data used by the RTNEPH, and, if a bias does exist, to determine if it is also evident in the resulting cloud amount estimates.

2. Background

Infrared data used in the RTNEPH are collected by two polar orbiting satellite systems, the DMSP OLS sensor in the range 10.2 to 12.8 μm and the NOAA/TIROS-N AVHRR sensor at 10.3 to 11.3 μm. Both sensors collect data in a region of the IR spectrum where the atmosphere is relatively transparent to terrestrial radiation. This is why brightness temperatures computed from these measurements can be compared directly to surface observed temperatures. However, the transmissivity of the atmosphere at these wavelengths is reduced by particulate scattering and absorption by water vapor. Normally these effects are negligible or can be adjusted for theoretically. However, when the pathlength through the atmosphere is exceptionally long, as in the case of an oblique satellite viewing angle, the amount of energy measured at the top of the atmosphere can be significantly reduced. The effect on computed brightness temperatures is to make the scene appear colder, which could result in the RTNEPH overestimating cloud amount.

Two corrections are currently being made in the RTNEPH to compensate for atmospheric attenuation. The first is a temperature correction added to brightness temperatures from moist tropical regions where absorption by water vapor is likely to be greatest. The second is to account for increased pathlength at viewing angles greater than about 40° and consists of a single grayshade correction to the IR data in the satellite global data base (SGDB) generated at the Air Force Global Weather Central (GWC).

3. Results

The first issue to be addressed was whether a scan angle bias exists in the IR grayshade data after the GWC correction has been applied. Data were collected from GWC data saves of the SGDB and other fields made for the AFGL effort for three case study days: 11 Aug 83, 7 Dec 83, and 12 Apr 84. IR grayshade counts for 24 RTNEPH grid boxes (~3000 km square) from each day were first stratified by background type, either land or water surface. The data were then converted to equivalent brightness temperatures and quantized into 5° viewing angle bins. An average brightness temperature was computed for each bin along with a confidence measure based on the number of points and the variance about the mean. Fig. 45 is a plot of average brightness temperature as a function of viewing angle for the 7 Dec 83 case. For a viewing angle range of from 5° to 65° the average brightness temperature dropped 8° K over land backgrounds and 7° K over water. Similar results were found for the other two case days. Thus a significant bias appears to remain in the IR data after the GWC correction. The relative magnitude of the grayshade correction can be seen in the relaxation of the downward trend in the curves of Fig. 45 at around 40°, most particularly in the water curve.

Given evidence of a 7 to 8° K bias in the brightness temperature data the more important problem was to ascertain if it was enough to cause a bias in the RTNEPH results. Because of problems with McIDAS, it was not possible to process any of the selected case study days through the cloud detection algorithm; so a previously processed data set from 11 June 82 was selected for analysis. The most important difference between the three case study days and the June data set is that all the June data are from a single NOAA satellite whereas the other days are from both NOAA and DMSP satellites.

RTNEPH INFRARED TEMPERATURES
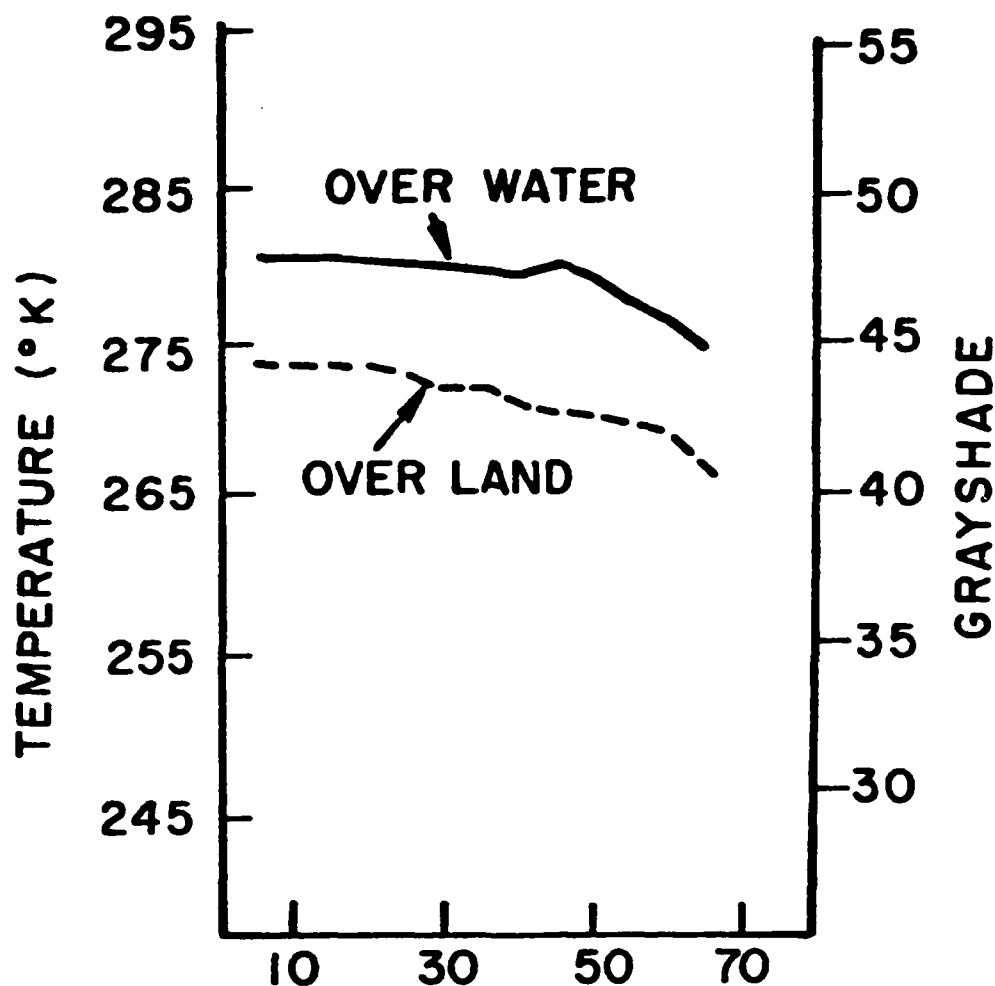
Fig. 45. Plot of Average Brightness Temperature as a Function of Viewing Angle for 7 Dec 83 Case

The cloud amount data were quantified into 5° viewing angle bins in the same way as the IR data, with average cloud amount computed for each bin. Results for 24 predominantly water background grid boxes are plotted in Fig. 46; a view angle bias of 20 to 25 percent exists for viewing angles from 5° off the satellite subpoint out to 70°. Negative view angles in Fig. 46 represent a viewing geometry to the left of the subtrack and positive angles are to the right. Due to the way data are mapped into the SGDB more data are available to the right of the subtrack. Again a relaxation in the trends around 40° can be seen to have been carried through from the GWC grayshade correction.

A different result was obtained from the analysis of 17 mostly land filled grid boxes as is illustrated in Fig. 47. No view angle bias was evident in this data set, although there are relatively large local variations from bin to bin due most likely to the limited sample size. Data for only 17 grid boxes were available because of limitations in the data base for this day. The reason no bias exists in the cloud amount estimates over land lies in the large thermal contrast between land surfaces and clouds during the summer season. The NOAA satellite used to collect the 11 June 82 data flies in a sun synchronous mid-afternoon orbit. At mid-afternoon in the summer, land surfaces in the northern hemisphere can be expected to be relatively warm compared to ocean surfaces. While cloud top temperatures over adjacent land and water surfaces can be expected to be approximately equal, the cloud to surface temperature difference will be considerably larger over the land surface. Since it is precisely this temperature difference that the cloud detection algorithm requires, cloud thresholds will be correspondingly smaller over the water surfaces so as not to miss low clouds. Therefore a small cooling of a satellite sensed clear ocean scene, due to IR attenuation, could result in a misinterpretation of the scene as low cloud.

4. Conclusions

A scan angle bias does exist in both the IR data used by the RTNEPH and in the cloud amount estimates produced by the threshold algorithm for scenes over water. A scan angle bias correction is applied to the IR grayshade data in the SGDB; however, it is not sufficient to compensate for the actual bias, nor is it sensitive to small changes in temperature. A better

115
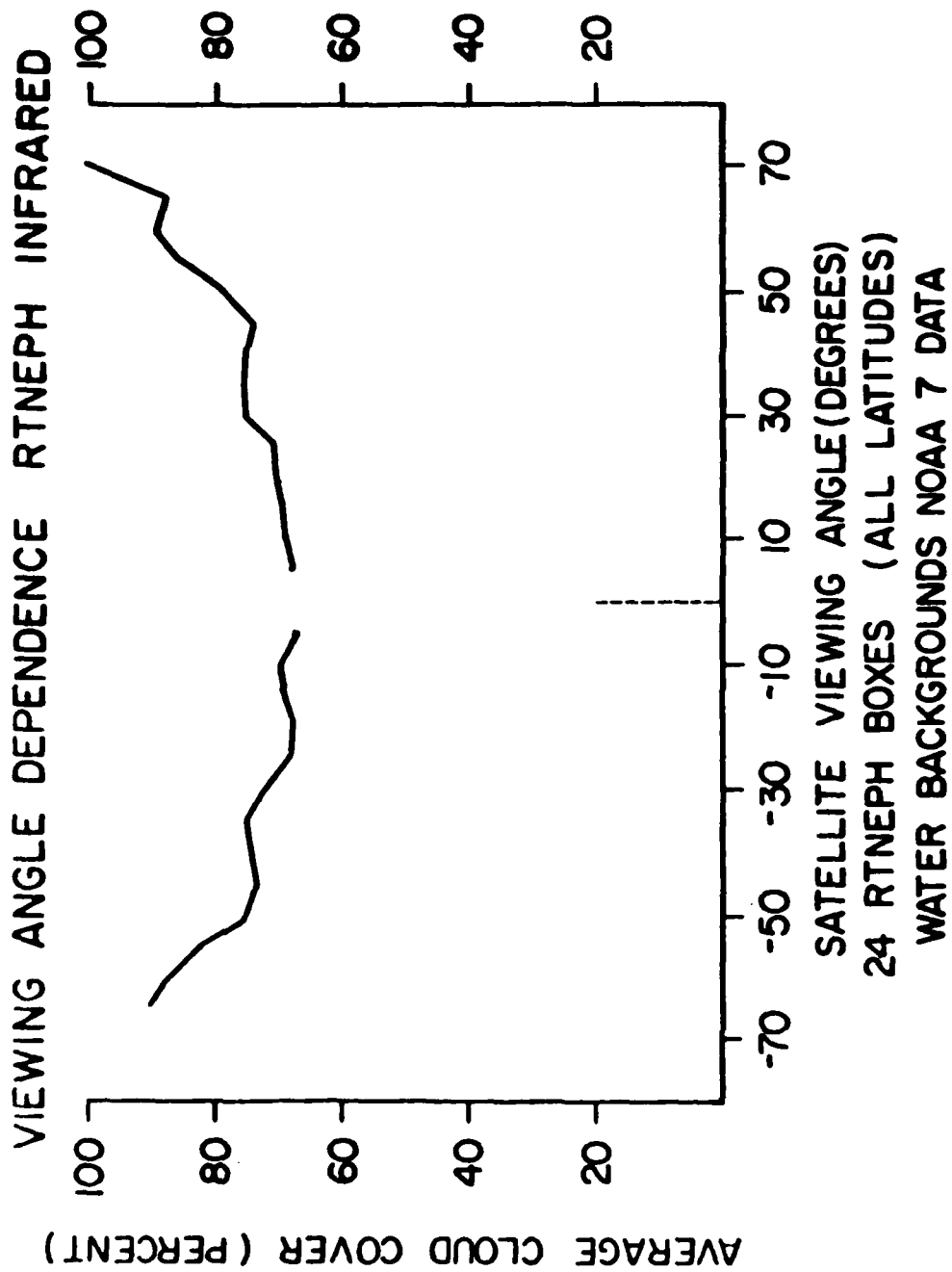
Fig. 46. Results for 24 Predominantly Water Background Grid Boxes
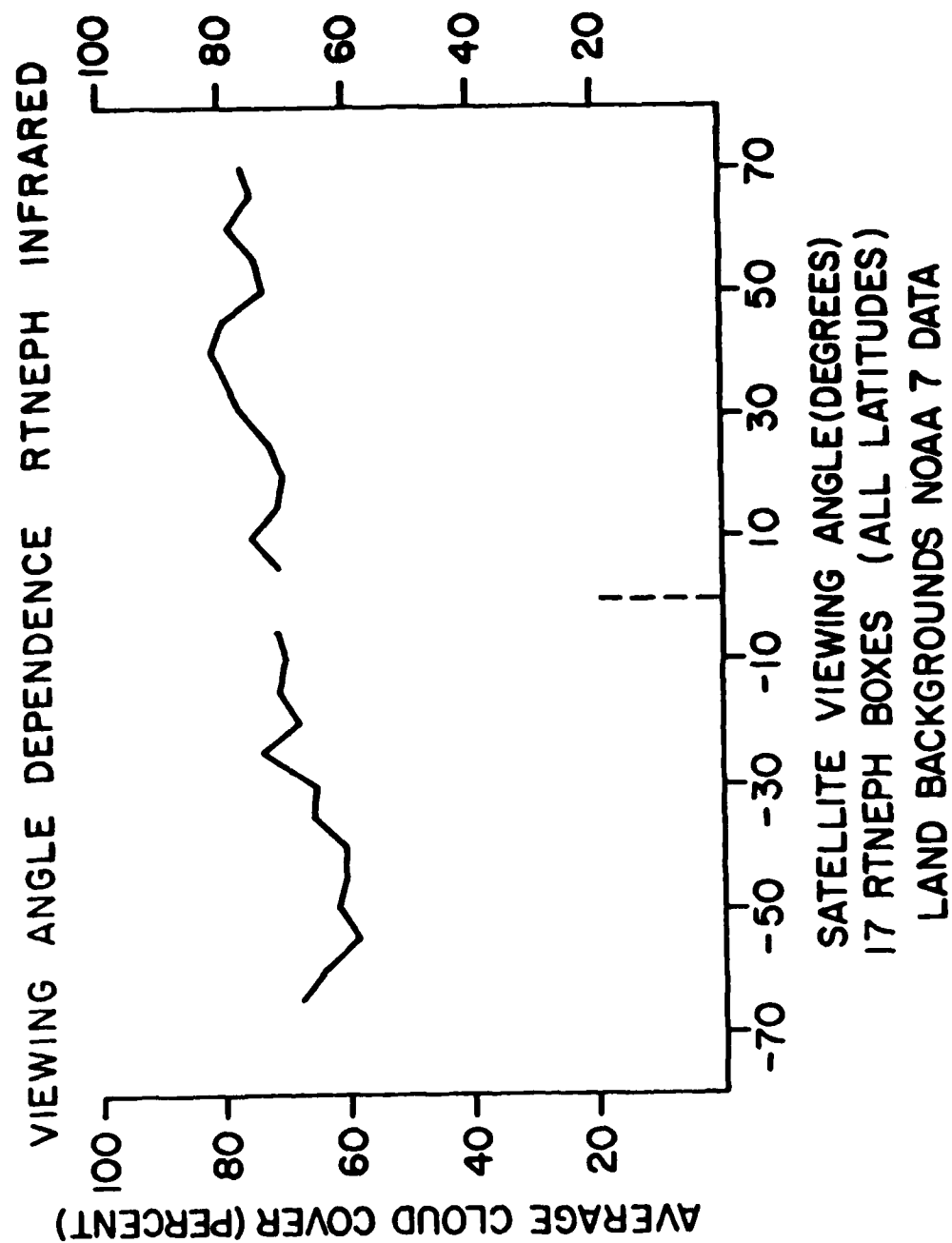
Fig. 47. Results for 17 Mostly Land Filled Grid Boxes

correction would be one applied to the brightness temperatures, at a resolution of 0.1° K, that are used in the cloud detection algorithm. It is still not clear that the IR bias will be carried through to the cloud amount estimates in all cases. It appears from the limited data set used here that at least for cases over warm land backgrounds, no viewing angle bias exists in cloud amount. Future studies should analyze more than 24 RTNEPH grid boxes at a time; at a minimum a full hemisphere (60 grid boxes) should be used. In addition it is necessary to stratify data further by season, latitude, satellite time of day, and sensor, as well as background type.

D. McIDAS Upgrade

1. Introduction

The man-computer interactive data access system known as McIDAS was purchased by AFGL from the University of Wisconsin in 1976 to provide a geostationary satellite capability. Since that time many modifications and additions have been made to both the hardware and the processing software. In 1983 it was determined that the existing system could no longer perform all the functions that were being required of it and the process of replacement was begun. On-site SASC scientists and engineers have been involved from the start in both the hardware specification and the system requirements phases of the upgrade.

Initially a Gould SEL 32/27 minicomputer was purchased to replace the original Harris 6024/5. A subsequent evaluation of system requirements made clear that a single computer was not the best solution to the needs of AFGL. The concept of a network of distributed processors, each functionally unique, was evolved as the best approach to the problem. However, such a configuration significantly increased the complexity of the system design. SASC contracted with Technology Systems Inc. (TSI) to provide assistance in performing a comprehensive system evaluation and design specification for the new system. A key feature of the design is the data base management system (DBMS).

2. System Requirements

The first step in generating a system design is to determine the system requirements. SASC and TSI reviewed existing AFGL requirements and

projected future requirements, analyzing system functionality according to six groupings:

(1) Data Ingest: The system must have the capability to accept data from at least three sources:

* Satellite data from a GOES via the existing ground station at AFGL and, in the future, from a VAS ground station that will become part of the system.

* FAA circuit data (surface and upper air reports and LFM output) over a low speed land-line and digital radar data from the AFGL Ground Based Remote Sensing Branch (LYR) via a medium speed data link.

* Taped data from other sources that will include polar orbiting satellite data, meteorological data, and data types that may become available in the future.

(2) Data Storage and Retrieval: On a distributed system considerable care must be taken in performing the data base management function. Twenty data types were identified that will reside on the new system including the offline data archive (Fig. 48). Each data type may reside at a different node on the network and may be acted on by more than one function. The system must have the capability automatically to maintain and update data dictionaries on each data file, including the file location and status. Mass storage requirements vary widely from node to node depending on whether or not large imagery files are to be stored there. Over 2,000 Gbyte/yr will enter the system, with a minimum of 1 Gbyte online at any one time. File transfers will occur between nodes on the network. The network architecture must take into consideration the size of the image files as the limiting factor in determining the speed at which these transfers will occur. A minimum aggregate transfer rate of 1 Mbit/sec is considered satisfactory for data files of 1 to 2 Mbytes.

(3) Output Products and User Interface: Standard data products consist of plotted data displays, contour analysis, and imagery. Three types of user workstations will be required to handle products:

Code	Description	Throughput MBytes/Yr	Online Time	Total Online MB
A	GOES-VISSR/VIS Data	1953480	1hr	446
B	GOES-VISSR/IR Data	122640	1hr	14
C	GOES-VAS Data	122640	1hr	14
D	DMSP-SSMI Data	200	90days	50
E	DMSP-OLS Data	912	90days	228
F	NOAA-AVHRR Data	320	90days	80
G	NOAA-HIRS Data	16	90days	4
H	NOAA-AMTS	16	90days	4
I	Conventional Surface			
J	Conventional Upper Air			
K	Conventional Fous 1	100	1yr	100
L	Conventional Fous 2			
M	Conventional Fous 3			
N	Gridded Data			
O	Radar			10
P	Online Data Dictionary			
Q	Historical Data Dictionary			10
R	Online Product Dictionary			
S				
T				
U				
V				
W				
X				
Y	Online Products Data			183
Z	Historical Archive			-
	TOTALS	2,200,224		1143

Fig. 48.   Data Type and Data Storage Requirement

* Standard text only terminals to be used for programming and
  text listing.

* Graphics terminals for program development and debugging and
  for use as graphics only workstations.

* Image processing workstations consisting of large areas of
  video memory, color lookup tables, overlay capability,
  programmable cursors, and high resolution RGB monitors.

Applications programs should be designed for execution in more than
one mode, selection depending on the limitations of the workstation in
use. User interface characteristics will depend on the needs of the indi-
vidual user. Users unfamiliar with the characteristics of the system will
have menu-driven routines capable of illustrating all possible processing
options of a particular program. Sophisticated users will use keyword di-
rected input for program flow control, allowing interaction with the mini-
mum possible number of keystrokes. An intermediate method will use program
directed user prompts.

(4) Interactive Display and Objective Analysis: A key feature of
the existing McIDAS to be carried over into the new system is the capa-
bility to analyze objectively and display any gridded data base. Analysis
routines vary from a two-pass Cressman for a fast analysis over a large
area to a rigorous five-pass Barnes technique for contouring over mesoscale
regions. Interpretation of data or analysis techniques is facilitated by
the ability of the user to interact directly with the data being dis-
played. Minimum requirements are to provide user interaction through a
programmable cursor on the display screen in combination with functions to
display raw data, modify data, select areas of interest, reposition/
reorient image display, and rescale data. Similar interactive functions
will be available to operate on imagery type data with additions such as
warping or stretching of imagery, remapping to one of a menu of projec-
tions, color/contrast enhancement, editing of bad data points, time series
looping, and overlay gridding.

(5) System Maintenance and Application Development: With a dis-
tributed system, system maintenance includes data base management and con-
figuration integrity. Organization of the data base manager must consider

121

the multiple hierarchy structure of the system with regard to the distributed nature of the processors, the large number of data types, and the variety of user interface options available. Future data types must be assimilated into the system with the understanding that most will be operated on by existing analysis routines. The DBM structure must reflect these needs. Data integrity must be maintained throughout the network, even if a node becomes inoperative for a period (including the DBM host). This requires that individual processors have the capability to maintain and update their local data dictionaries and to broadcast any changes around the network once communication is re-established. Applications programs must have a standard data base interface structure. The introduction of a new data base should not require modifications to existing programs in order for those programs to operate on the data. The applications development environment should be as standardized as possible given the different operating systems and language environments on each processor. Programs written on one machine should be portable to another machine with a minimum of rewriting. This requires that all DBM functions have a common interface structure on all nodes.

(6) Architecture and Distribution of Data and Products: Since each node on the LAN will be defined functionally, each will have different data storage and retrieval requirements. The physical architectur~ must be flexible enough to provide for transfer of commands and files of a few bytes up to image files consisting of megabytes. Local storage requirements will be dictated by the largest data files to be stored; in the McIDAS, the largest files will always consist of imagery. Each node requiring imagery data must be specified to maintain large mass storage devices (i.e., 1 Gbyte). A significant portion of the overall data base will be products generated by various applications programs. Some of these product files will be of the order of imagery files in size.

3. Proposed System

A system design specification has been produced in an effort to satisfy the requirements stated above. The design attempts to utilize state of the art capabilities in distributed processing, data base management, image processing, and mass storage. The design calls for a system of distributed processors linked by a local area network (LAN) as shown in

Fig. 49. The rationale behind a distributed system is to provide a sepa-
rate environment for each identifiable function of the system. In this
case each function will be performed on a dedicated processor that is a
node on the LAN. Three unique functions have been identified for the pro-
posed system:

* Data Ingest: Satellite and circuit data will be automati-
cally received at this node. The node processor will be the
Harris 6024/5 computer that is currently the McIDAS host.
Local storage will provide an online archive for GOES im-
agery, surface and upper air reports, and LFM forecast model
station output.

* Image Processing: Image processing and display functions
will be performed at this node. The configuration will
consist of a Gould 32/27 minicomputer front end processor
(FEP) that will drive a video storage and display system.
Interactive control will be maintained through a co-located
CRT terminal and an asynchronous control device such as a
joystick, trackball, or graphics tablet. Current plans call
for two workstations to be controlled by the same FEP.

* Batch Processing: Large number crunching routines (such as
the RDNEPH model) and intra-network communication to AFGL/
LYR and the AFGL central VAX 11/780 will be performed at
this node. In addition all system wide network and DBMS
functions will be maintained here. A VAX 11/750
minicomputer has been selected as the host processor for
this node.

All processors of the LAN will also be connected to the AFGL broad-
band network for terminal sharing via a virtual terminal capability. This
will enable any authorized user to access any of the three LYS computers
from any terminal in the laboratory that is connected to the AFGL network.
In addition, all local programming terminals will also be linked to the
AFGL network in order to minimize the number required for program develop-
ment needs.

A direct data link between the Ground Based Remote Sensing Branch
(LYR) VAX 11/750 and the LYS VAX 11/750 will be established for exchange of

123
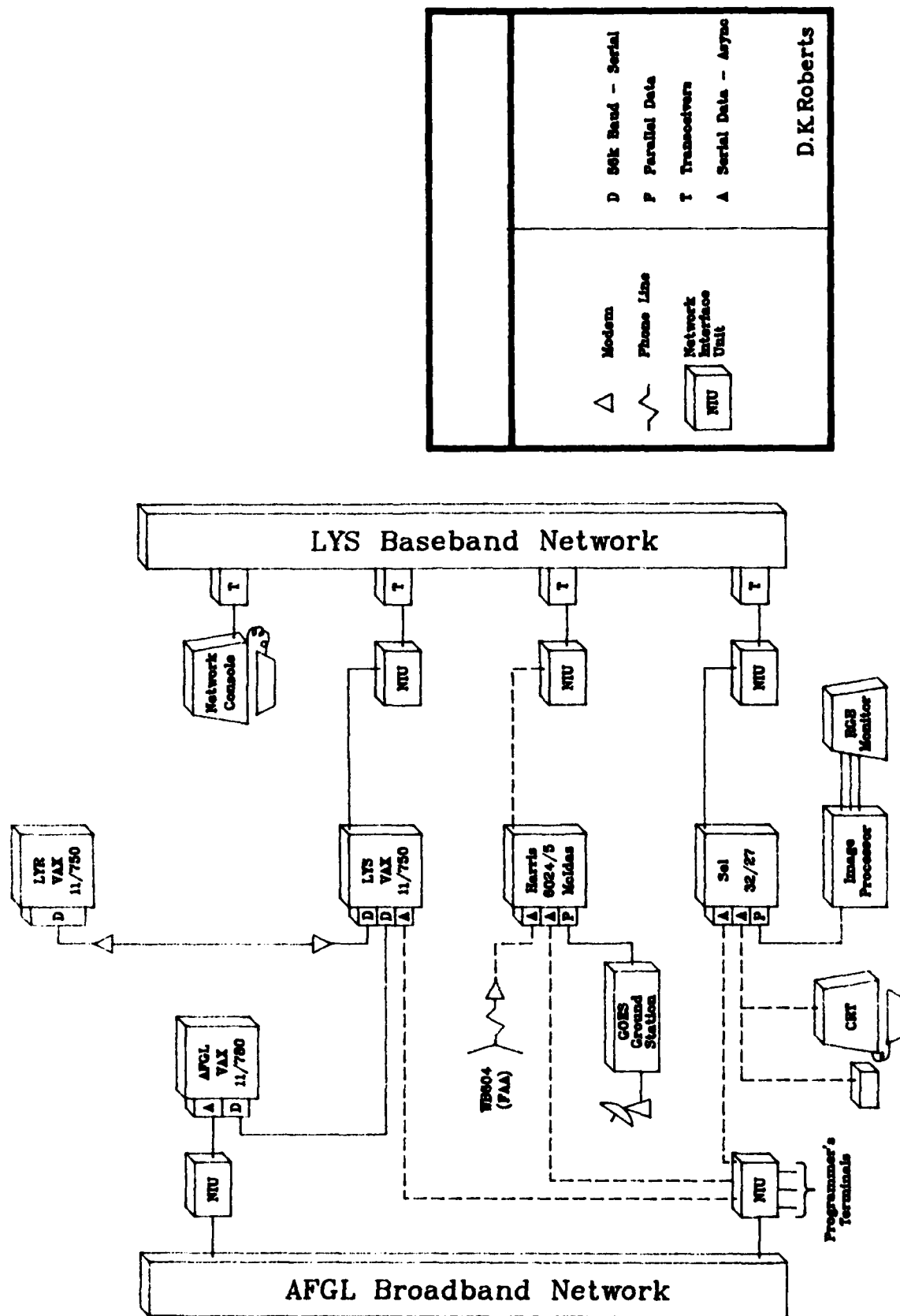
Fig. 49. Proposed System Configuration

digital satellite and radar data. Physically the link will consist of a conditioned voice-grade telephone line and modems capable of data transmission at a rate of 9600 kb/s. Remote communication with LYR will be managed by Decnet protocol and software running on the two VAX computers.

a. Layered Software

In addition to applications programs that users interact with, each node on the network must perform functions that are transparent to the user. For example, each node must maintain and update its own local data directory and perform network I/O transactions. The complexity of these functions on each node motivated a layered approach to software design. A layer is a functionally related set of routines designed in a hierarchical structure such that the most applications dependent layers are at the top and the most hardware dependent layers are at the bottom. Applications routines in the top layer are independent of the computer they operate on; they call machine dependent routines in lower layers in order to perform operations such as data base and network transactions. Fig. 50 is a schematic representation of the layer hierarchy of the system design. Design and implementation of software are from the bottom up; that is, lower level routines are implemented first. For example, the data base manager will not be designed until the network management layer has been fully implemented. In this way all I/O requirements of the DBM can be satisfied by calls to the existing network management layer. This procedure greatly simplifies the entire implementation process since each routine can be designed and tested in isolation, thereby eliminating uncertainty as to where possible errors lie.

Normally routines on a given level will interface only with routines on adjacent levels; however, there may be cases where several layers are crossed. For example, a user may need to access network routines directly, as in the case of a failure of the DBM host system, in order to locate data on another node.

b. Local Area Network

The local area network consists of the physical transmission medium (i.e., coax cable), network interface units (NIU) to each physical node, and network software to manage communication over the network. Several

125

USER

```
[- - - - - - - - - - - - - - -]

[        APPLICATION          ]

[- - - - - - - - - - - - - - -]

[    DATA BASE MANAGEMENT      ]

[- - - - - - - - - - - - - - -]

[    NETWORK MANAGEMENT        ]

[- - - - - - - - - - - - - - -]

[    PHYSICAL INTERFACE        ]

[- - - - - - - - - - - - - - -]

[        NETWORK              ]

[- - - - - - - - - - - - - - -]
```
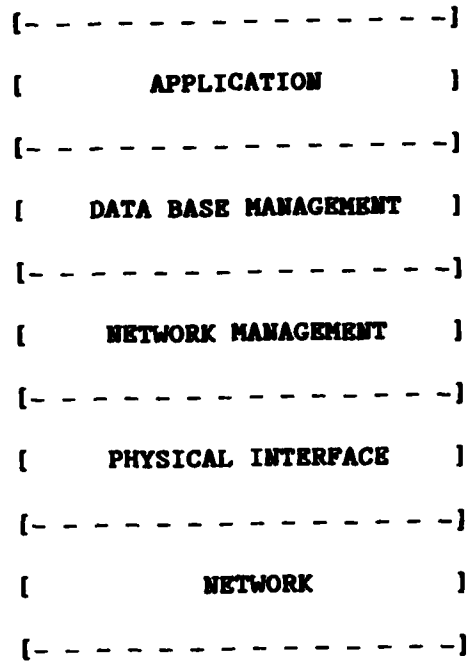
DATA LINK

Fig. 50. Layered Structure

different protocols are available to transfer data over a LAN. For large file transfer operations (> 1 Mbyte) the most common is datagram. A datagram is a logical entity composed of two parts, a data packet and a command string. Data packets are blocks of data that are of known length, measured in bytes. Command strings preceed data packets and contain information about the data, such as the address of the destination node, address of the sending node, length of the data packet, a process identification number, and a sequence number. Typically datagrams can carry data packets that vary in length from 600 to 2500 bytes. In order to transfer a large file, a series of datagrams must be transmitted over the network. Network software handles the transfer of datagrams from one node to another through a protocol known as Carrier Sense Multiple Access with Collision Detection (CSMA/CD). To send a datagram, network management routines at the sending node check the transmission line to determine if any transactions are currently in progress (carrier sense). If the line is clear, the datagram is transmitted. However, all nodes on the network have unrestricted access to the line (multiple access) and a second node could transmit a datagram at the same time as the first; in this event a collision occurs. Network overview routines detect the collision event (collision detection) and send a retransmit command to each node. After waiting a random time interval, the node then retransmits the datagram. This procedure continues until all datagrams have been transmitted and received.

c. Physical Interface

Each physical node on the network connects to the network at a NIU. The link between the computer and the NIU can be established in one of several different ways (e.g., parallel DMA or serial asynchronous). A device driver routine on the processor controls I/O operations through the selected interface. Generally the computer manufacturer will provide device driver software as a part of the operating system.

d. Network Manager

The network management function is to provide the environment for I/O operations on a network wide scale. Requirements include data routing, error checking, synchronization between nodes, file transfer, command transfer, and error recovery. Four functional areas have been identified for the network manager:

127

* Configuration Control: Changes in the logical structure of
  the network are handled by functions such as connect and
  disconnect, initialize, reset, and check network status.

* Send Data and Commands: Network data transmission require-
  ments include functions to format and transmit data, handle
  requests in a logical order, and optionally await acknowl-
  edgement from the receiving node.

* Receive Data and Commands: Data received at a node must be
  buffered, checked for errors, unpacked and routed to the
  correct location in memory. In the event of transmission
  errors or missing data, a retransmit message is sent to the
  sending node. Optionally a receipt acknowledge message will
  be sent to the sending node.

* Acknowledge Transmit/Receipt: A condition code will be sent
  in response to an inquiry request for transaction status or
  node availability status.

e. Data Base Manager Structure

The data base management function for a distributed system can be
one of several different logical structures. Since each physical node on
the network will have different files and data types stored locally and yet
have access to data anywhere on the network, the DBM must provide both a
local and a global directory and data access capability. Two logical
configurations for the DBM are under consideration, star and ring.

A star configuration specifies a single node on the network as the
DBM host. The host node contains a global data dictionary with entries for
every file on the entire system. In addition each local node (including
the host) has a separate local data dictionary containing entries for only
those files stored locally. The advantage of a star system is that all
data requests can be processed at a central location by a single set of
routines. In addition all global requests for data, that is, all requests
for data not available at the requesting node, can be satisfied without
polling each individual node but rather by a single request to the host.
The major disadvantage of the star configuration is that when the host is
unavailable (i.e., network or system failure) a backup system is required
for any global or network transactions. Such a backup might be a manual

128

poll and search procedure for checking the local dictionaries of individual nodes.

A ring configuration of the DBM specifies local data dictionaries and redundant DBM software at each node. In this configuration each node is responsible for satisfying global data requests on its own because there is no central system wide data dictionary. This would be done by a broadcast request to all nodes for data on the network. Individual nodes would in turn search their local data dictionaries for the requested data and return an acknowledgement to the requesting node. A second request would then go out from the requesting node to a selected node to transmit the data. The advantage to the ring logical configuration is that all network transactions can continue in the event that any one or more nodes becomes unavailable. The disadvantage is that duplicate software for global polling and searches has to be implemented at each node and no single node has system management responsibilities.

Data files will be cataloged into multiple link-list data dictionaries that collectively describe the contents and attributes of each file. DBM software will operate on the dictionaries, rather than on the actual data files, when performing functions such as search and delete. Individual dictionaries contain information on a single attribute of a data file. Within a descriptor string there will be pointers to entries in other dictionaries that contain different information on the file. Thus the data dictionary files are themselves a relational data base. Each entry in one dictionary points to collaborative entries in others. Fig. 51 is a schematic representation of a proposed configuration for the data dictionary scheme. Four categories of data dictionaries have been identified, each containing different descriptor information on the data files:

* System Configuration Dictionary: Since the data base is to be distributed over the network, system configuration and file location information must be stored. This dictionary will contain logical node descriptors including location address, hardware and software characteristics, and data type restrictions (i.e., file size).

DATA DESCRIPTOR

```
           +-------------------+
           | data type         |
       --> | file formats      | <--
           | valid time        |
           | earth location    |
           | projection        |
           | ...               |
           +-------------------+
```

ONLINE DATA

```
+-----------------+
| data type       | <--
| data name       |
| location        | <--
| filename        |
| access code     |
| ...             |
+-----------------+
```

ARCHIVE DATA

```
                              +-----------------+
                          --> | data type       |
                              | data name       |
                          --> | location        |
                              | volume/file     |
                              | user/owner      |
                              | ...             |
                              +-----------------+
```

SYSTEM
CONFIGURATION

```
           +-------------------+
       --> | location          | <--
           | node name         |
           | node address      |
           | node type         |
           | word size         |
           | ...               |
           +-------------------+
```
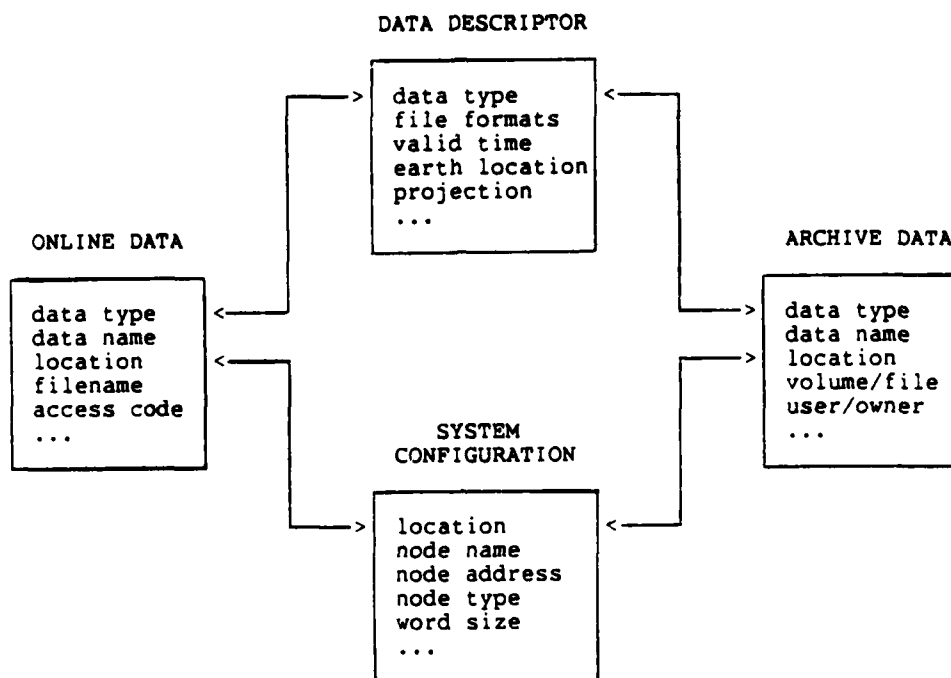
Fig. 51. Data Dictionary Structure and Configuration

130

* Online Data Dictionary: Each data file on the system will
  have one entry containing DBM access and management informa-
  tion. Multiple copies of the same data file will each have
  an entry in this dictionary, all pointing to the same entry
  in the data descriptor dictionary.

* Data Descriptor Dictionary: Each data type will have one
  entry (including multiple copies of the same data type) de-
  scribing the physical characteristics of that data. Any
  data type that is modified through editing or processing
  procedures will be designated as a new data type and given a
  separate entry in this dictionary.

* Archive Dictionary: In addition to whatever data are stored
  on the network, an offline archive data base is maintained.
  Each data file in the archive is cataloged into this dic-
  tionary at the time it is removed from the system. In ad-
  dition to the owner, access, and data descriptor informa-
  tion, there are volume ID (i.e., tape or disk) and file num-
  ber to locate the data in the archive storage area. Data
  descriptor information is kept in the online data descriptor
  dictionary so that it is available whenever an archive pro-
  duct is restored.

DBM software will handle data requests where the data are specified
by any combination of attributes listed in the data dictionaries. For
example, a data file could be specified by, say, data type, valid time,
earth location, and location on the system. The same data file could also
be specified by creation date, owner name, access rights, and file name.
Users and applications programs are free to specify the file in whatever
form best suits their needs and the DBM software will handle the request
through a standard interface.

f. Applications Programs

All applications software will interface with the DBM or lower level
routines through standardized interface formats. DBM functions will be
performed in a device independent manner and will be transparent to the
applications routine. In this way all higher level routines can be brought
up on any system throughout the network and operate regardless of the I/O

131

hardware present on that particular node. Applications environments, including the operating system and development language (i.e., FORTRAN), should be as common as possible. This means that any device dependent routines or extensions should be avoided. DBM functions will reside in libraries that are directly callable from within the applications programs. Other libraries that will support applications routines include graphics, mathematics, image processing, and so on. Within the applications layer, modular programming practices will minimize the amount of redundant programming that is required and will streamline the debugging process.

E. McIDAS Enhancement, Operation, and Maintenance

As part of the McIDAS upgrade (see section D, above) the following equipments were received:

(1) Gould Concept 32/27 computer, including 1 Mbyte of on board memory, and 160 Mbyte CDC disk, Pertec 45 IPS tape transport, and 8-port EIA/RS232 asynchronous interface. The Gould computer is a 32-bit high speed digital system designed for scientific, data acquisition, and real time services.

(2) Texas Instrument Model 810 printer, to be used with the Gould system until the faster 300 LPM Data Products printer can be released from the current McIDAS configuration.

To provide additional terminals required by the two systems in parallel, SASC leased two terminals (a Lear Siegler Model ADM 24 and a Digital VT 240) from Continental Resources Inc. of Bedford, MA.

An EIA/RS232 asynchronous switching box was fabricated to allow the LA-36 Decwriter terminal to be switched between the Gould system and the McIDAS system. The box also contains an LED display to show what lines are active and a toggle switch to reverse the transmit and receive lines if needed.

McIDAS downtime during 1984 was limited to a four-day period when the system main storage disk experienced a head crash. The long downtime was due to the non-availability locally of the head assemblies. Work on the disk was performed by Harris field service division under contract with SASC.

The following major items required maintenance during the year. The end item is listed followed by the components that were replaced to bring the equipment back to operating condition:

(1) Harris Laserfax Photo Recorder Model 530 - Processor motor and rollers; low voltage power supply; modification of the recorder to operate with 8 1/2" width paper instead of 11" width paper.

(2) Leonessa System 140B Signal Processor - Operational amplifier LM 301H located on card 1481.

(3) Sony Archive System - ± 12 v power supply in record electronics drawer number 2.

(4) Digital Interface - I.C. N8263 (digital multiplexer chip) in drawer number 3.

(5) Televidio Terminal Model 910 - New keyboard.

(6) Harris Laserfax Photo Recorder Model 850 - Capacitors C61 (500 µf) and C31 (250 µf).

(7) Harris Line Printer Model 4110 - Ribbon advance gear and motor; static eliminator; drum drive motor; two hammer drive boards; logic board.

(8) Hazeltine Executive 80 Terminal - New keyboard.

(9) EMR PCM Bit Synchronizer Model 720-02 - Capacitor C59 and diode CR15 located in the loop filter card.

(10) Sony Archive System - All drive belts in recorders and players.

(11) Conrac RGB Monitor Model 5711 - Transistor Q4 (2N3643) on the input board.

F. CLOUDS Study

1. Introduction

AFGL is participating with the Air Force Weapons Laboratory (AFWL) and Scripps Institution of Oceanography in a study for the AFWL Strategic Defense Laser Program (SDLP) to determine the impact clouds will have on the SDLP. This study is known as Cloud Logic to Optimize the Use of Defense Systems (CLOUDS). A whole sky E/O imager (WSI) system was developed and constructed as part of the project and used for a four-week demonstration period during the August-September 1984 field test at White Sands Missile Range, New Mexico. Work efforts are directed to developing techniques

to determine cloud-free arc (CFA) statistics, compare WSI statistics to a sample of 35 mm digitized film images, and develop a model to estimate the probabilities of CFA from surface and satellite cloud climatologies.

The objective of the satellite portion of the study is to devise techniques for extracting cloud information from geostationary satellites and retrieve and analyze visible and infrared (IR) data from the four-week demonstration period. The McIDAS facility was viewed as the logical source for data collection and archive capabilities and also for use as an analysis tool. During the four-week demonstration period full resolution visible and IR data from GOES-6 were collected hourly from 14 GMT to 00 GMT over the White Sands area. The entire data collection and archive process was automated on McIDAS through development and implementation of macro program CLD to ingest hourly navigation and imagery, TV load the imagery for subjective quality checks, and save the imagery on magnetic tape. In all, visible and IR data were taken for some 308 separate hours of GOES-6 satellite data availability. AFGL meteorologists are taking steps to devise an optimum method for generating background reflectivity fields, stratified according to a specified range of solar elevation angle. Once generated, the background fields will be used as the threshold for the cloud/no cloud determination in the objective analysis of the data. SASC is currently providing software support on McIDAS through development and implementation of programs for data processing, analysis, and navigational corrections.

2. Data Processing and Analysis

The unfortunate early failure of GOES-East prompted a decision to maneuver the western satellite, GOES-6, to a subpoint position nominally 98° W above the equator to provide continuous coverage of the southern Atlantic for the hurricane season. This maneuver brought the satellite to a longitude within 10° of the White Sands area and consequently provided this study with near optimum spatial resolution visible and IR imagery (approximately 1 km and 8 km respectively). Direct image comparison techniques to be employed in this study require that compared pixels represent the same geographic area to within bounds determined by navigational accuracy. To meet that requirement it was decided to remap the imagery to a fixed Mercator projection of a latitude-longitude based grid. Initial grid

dimensions were defined as 200 km by 200 km with a grid spacing (resolution) of nearly 1 km. However, due to memory limitations imposed by the Harris minicomputer, the area had to be reduced to one-fourth the original size (100 km by 100 km). Fig. 52 is a full resolution visible satellite image taken from the archive showing the general area of interest centered on the field test site. The white box is a graphic overlay outlining the approximate geographic bounds (in the satellite projection) of the 100 km by 100 km grid also centered on the field test site. The White Sands area at the top center of the box appears bright (white) relative to its immediate surroundings. Fig. 52 also shows the distribution of stations (three-letter station identifiers) that report hourly surface observations for the area as part of the synoptic network. Note that all but one station have been eliminated from the grid area as a result of reducing grid size from 200 to 100 km on a side. Although it is expected that observation data from the field test site will become available in the near future, the existence of only one station for the grid will impact verification of applied techniques against ground based observations that are readily obtainable on McIDAS.

A successive differencing technique has been devised as one method to generate background reflectivity fields. An analyst selects an image subjectively determined to be free of cloud and processes (remaps) the image as a first approximation to the background field. Succeeding images are then examined for excessive cloud and shadow and if found acceptable, are compared to the background field pixel by pixel. Values in the background field are updated (replaced) by values from the image if the image value is numerically lower (lower brightness value) and the difference in values does not exceed a predefined constant. Although processing intensive, this technique can produce reasonable background fields when applied over the entire visible data archive. In this technique, background fields are considered for three categories of ranges of solar elevation angle, as shown in Table 2. Angles greater than 80° are estimated to be associated with nighttime conditions when visible data are not available and are therefore omitted.
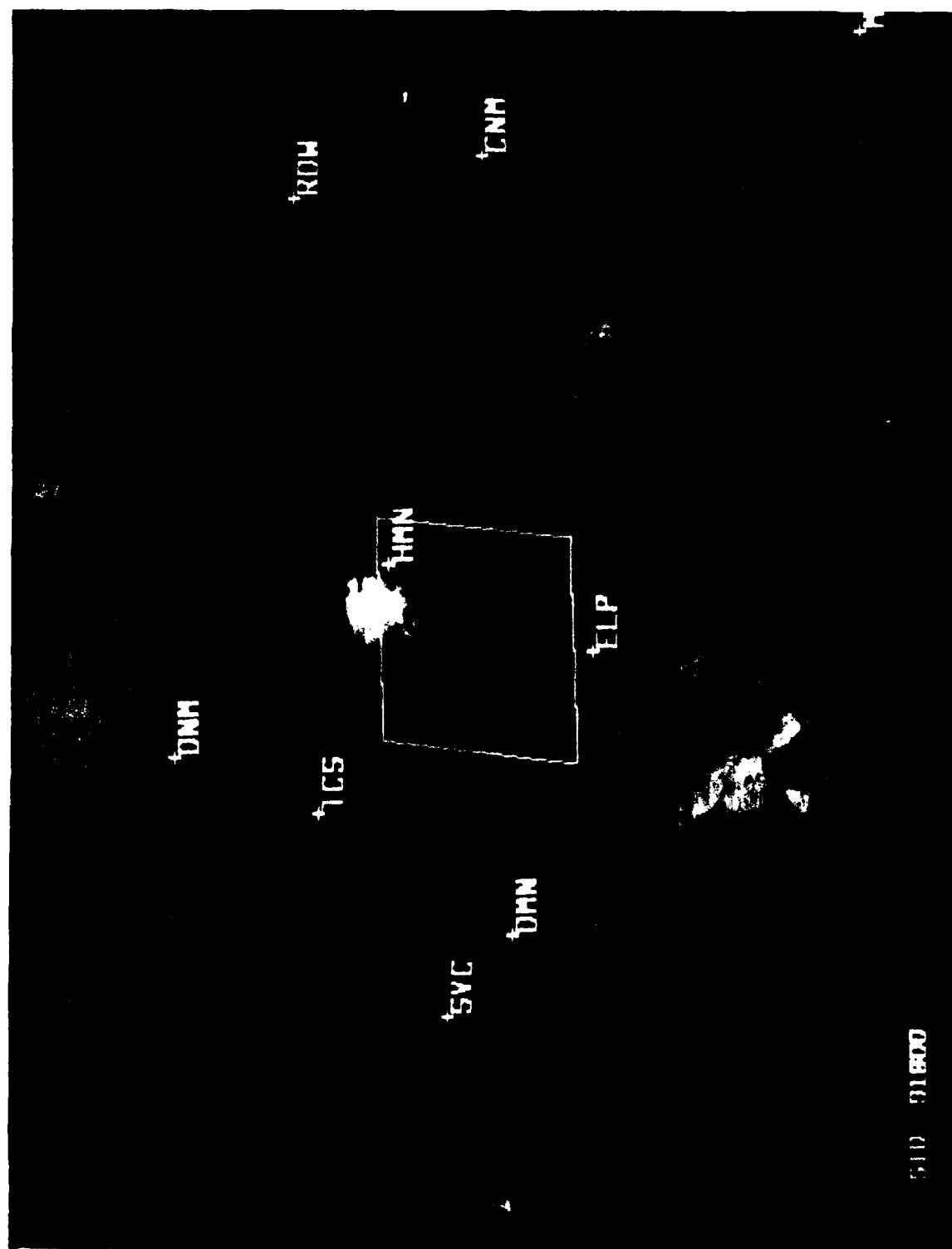
Fig. 52. Full Resolution Visible Satellite Image with Graphic Overlay of Grid Bounds and Surface Observation Station Identifiers

TABLE 2. CATEGORY RANGES OF SOLAR ELEVATION ANGLE

Category	Data Range
--	> 80°
1	60° - 80°
2	35° - 60°
3	< 35°

To satisfy initial data processing and analysis requirements for the satellite portion of this study, program CLOUDS was developed as an interactive routine to run on McIDAS. Its primary task is to remap the imagery according to the guidelines mentioned above. It is designed to facilitate a step-through procedure in implementing the above technique for generating background fields together with existing grid utility software to perform data base management functions. Once the background fields are generated, the CLD option of CLOUDS can be used to select automatically the appropriate background grid to be used with an analyst-chosen cloudy grid to compute pixel area, number of pixels determined to contain cloud, and total cloud amount as a percentage of pixel area. Due to memory restrictions on the Harris minicomputer, the maximum area available for use in generating these statistics during a single session is limited to one-fourth the area represented by the grid. As a result, the analyst must specify one of four quadrants to define an area of interest when invoking this option. In addition, the CLD option produces a line printer plot in grid array format depicting the resultant cloud/no cloud analysis for the selected quadrant. The plot appears together with a printout of the statistics on a single printout page in compact format to facilitate analysis and interpretation and to allow one to monitor thresholding techniques applied to suppress artificially induced cloud. Fig. 53 is an example of line printer output produced by the CLD option of CLOUDS. Initial visual comparisons have been made of plots generated with this option with corresponding cloudy images displayed on McIDAS.

QUADRANT 1
IMIN 1   JMIN 1
IMAX 50   JMAX 50
THRESHOLD 8
AT TIME 1900   JULIAN DATE 262
OVER AREA 2500
NUMBER OF CLOUDY PIXELS 554
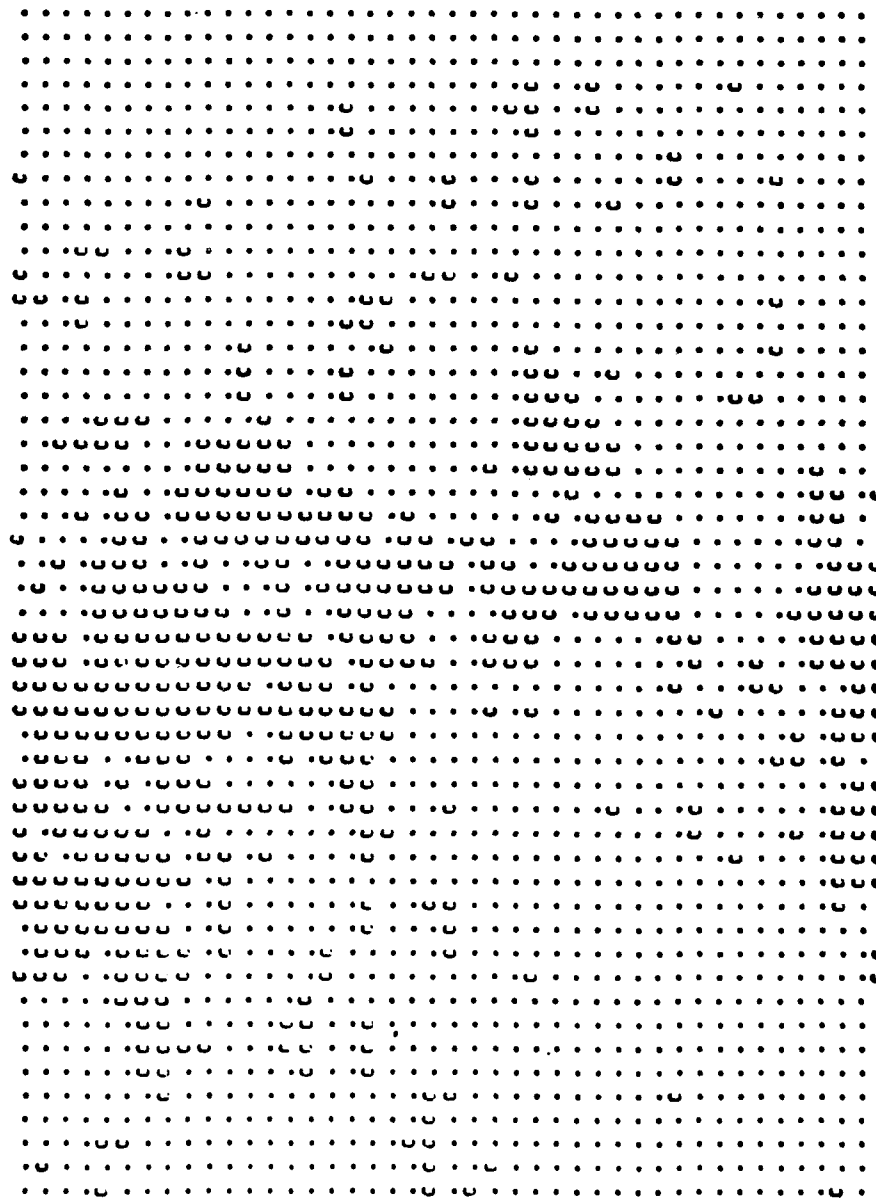A PERCENTAGE CLOUD AMOUNT OF 22.16

Fig. 53.   Line Printer Plot of Cloud/No Cloud Analysis Produced by CLD Option
           of CLOUDS

3. Navigational Corrections

Repositioning of the western satellite to 98° W longitude after failure of the GOES-East VISSR caused large navigational errors in the imagery being collected for the archive. To correct for these errors and in general, provide a limited, semi-automated navigational correction capability on McIDAS in anticipation of future errors of such magnitude, an interactive routine was developed and implemented. Program LOCLMK redefines the origin, in satellite coordinate space, for each image based on seven landmarks identified in the area of interest. Fig. 54 is a full resolution visible satellite image showing the general area of interest for this study. The three-letter identifiers in the graphic overlay indicate the seven landmarks chosen for the renavigation procedure. Although the correction is linear and the satellite projection is curvilinear, this type of correction was judged to be adequate over the relatively small area of the image (approximately 500 km by 500 km). After a short learning period, an observer can renavigate all 11 images collected for a single day in 15 to 30 min depending on cloud obscuration of landmarks.

LOCLMK was also developed with a number of options to perform utility functions as well. Landmarks that are user-defined by a three-letter identifier and whose earth coordinates (latitude-longitude) are known to an accuracy greater than or equal to the resolution of the visible sensor can be added/deleted from a list file (with entries for 100 landmarks) that is maintained and manipulated by the program. This list is available for viewing via the local terminal CRT or as line printer output as shown in Fig. 55. All visible and IR imagery comprising the archive were eventually renavigated using program LOCLMK.

Fig. 54. Full Resolution Visible Satellite Image with Overlay of Landmark Identifiers Produced by LOCLMK

```
        ***       A F G L   M C I D A S      ***      PROGRAM:  LOCLMK
  1   ID  =  NLB    334923   -1055625
  2   ID  =  SLR    331534   -1061808
  3   ID  =  FRR    330828   -1071055
  4   ID  =  LBD    320345   -1070113
  5   ID  =  LSR    323537   -1042049
  6   ID  =  SMI    310607   -1065519
  7   ID  =  RBL    315409   -1035532
  8   ID  =  FAR    364300   -1081300
  9   ID  =  SHP    364700   -1084330
 10   ID  =  SLN    411200   -1120800
 11   ID  =  XL     150000    -630000
 12   ID  =  GRE    411300   -1093230
 13   ID  =  SAN    374030   -1054330
 14   ID  =  SMI    372400   -1053200
```

Fig. 55.   Sample Listing of Defined Landmarks Proposed by PLT Option of LOCLMK

VI. CLIMATOLOGY

A. Military Standard 210 Revision

1. Introduction

Military Standard (MIL-STD) 210 in its current form provides statistically derived global extremes of the vertical atmosphere as envelopes of 1 and 10 percent cold/warm temperatures and high/low densities for the worst month and location at each altitude. Values at various levels on these envelope curves can provide questionable results compared to structures of realistic atmospheres. Therefore a study was undertaken by AFGL to determine consistent vertical profiles of temperature and density that would occur with 1 and 10 percent extremes at specified altitudes. This report describes the data processing activities for that study. Final results will be included in a revision of the current standard.

2. Specification

SASC's involvement in the revision of MIL-STD 210 was to devise and implement programming and data processing techniques responsive to these specifications:

* From a uniform period of ten or more years of upper air radiosonde and rocketsonde measurements over many locations (excluding Antarctica), derive monthly statistics of temperatures and densities at 5, 10, 20, 30, and 40 km levels for each location.

* At each of the five specified levels, produce cumulative probability plots and tabulations for stations and months possessing statistically the most extreme 1 and 10 percent high and low temperature-density values.

* Allow editing of any suspicious data that may be detected from subjective interpretation of graphically displayed cumulative probability distributions.

* Determine dates and times of all individual profiles for the stations and months containing most extreme values only. Plot and tabulate temperature profiles thus determined for further subjective analysis.

142

*   From subjectively chosen temperature profiles of the most ex-
        treme cases, assemble temperature and lapse rate data input to
        a program developed to compute final hydrostatically consis-
        tent profiles from the surface to 80 km.

The steps taken to accomplish these tasks are presented in the fol-
lowing sections. Fig. 56 is a guide to the flow of the data processing
steps involved, where portion (a) relates to discussion of data sources,
(b) to formatting and data compression, and (c) to applications software.

3. Source Data

Meteorological Rocket Network (MRN) upper air observations contained
on fourteen magnetic tapes together with documentation (Reference Manual,
1970)[37] were made available (labeled L tapes in portion (a) of Fig. 56),
providing vertical measurements of the atmosphere between approximately 20
and 80 km for the period 1969 - 1982 at 19 stations listed in Table 3(a).
Temperatures and densities are recorded at meter levels normally once a day
within plus or minus six hours of conventional rawinsonde (radiosonde) ob-
servations.

Seven C tapes were later received containing conventional radio-
sonde data from Canadian stations. Four of these tapes contained upper air
observations at standard pressure levels and the other three tapes con-
tained associated measurements at significant levels. Data and format
documentation were also made available.[38,39] This data set is for the
period 1969 through mid-1980 and contains radiosonde observations twice

---

37. Reference Manual, 1970: Tape Deck 5850 Rocketsonde Observa-
tions. Environmental Data Service, National Climatic Center, National
Oceanic and Atmospheric Administration, U. S. Department of Commerce.

38. Department of Transportation - Meteorological Branch - Canada,
1965: Card 5 Type Card Format Documentation. Climatology Division,
Toronto, Canada.

39. Department of Transportation - Meteorological Branch - Canada,
1970: Card Type 18 Card Format Documentation. Climatology Division,
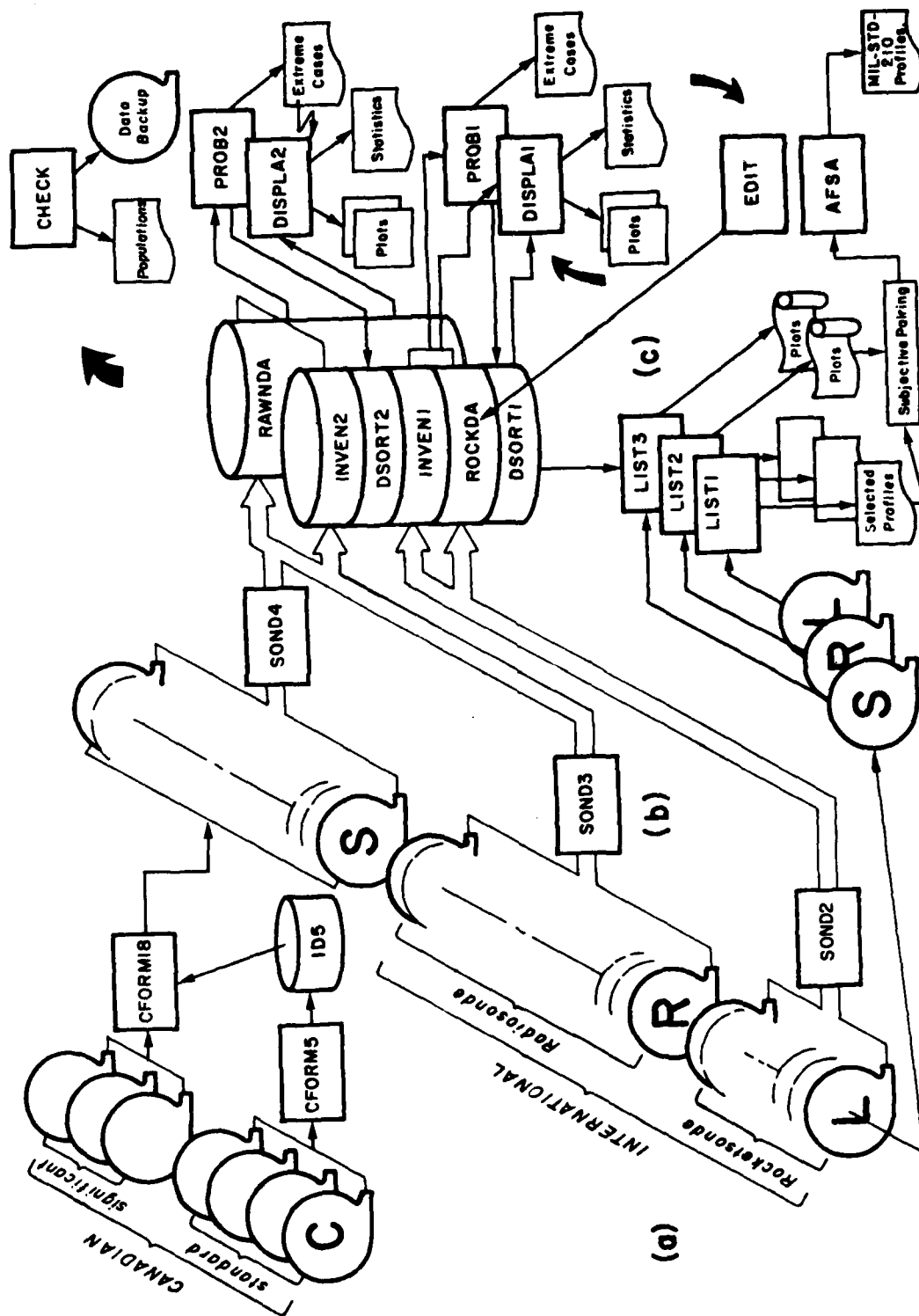Toronto, Canada.

Fig. 56. Data Processing Configuration for MIL-STD 210 Revision and Expansion

144

TABLE 3. MRN AND CANADIAN STATION NAMES PROVIDING DATA ON L AND C TAPES
RESPECTIVELY

(a)			(b)	
WMO STATION NUMBER	STATION NAME		WBAN STATION NUMBER	STATION NAME
78861	Antigua, B.W.I.		15045	Ocean Weather Ship P
08384	El Arenosillo, Spain		15601	Goose
61902	Ascension Island, AFB		14503	Stephenville
91162	Barking Sands, Hawaii		14531	St. John's
74979	Cape Kennedy, FL		82512	Shelburne
72913	Fort Churchill, Canada		14642	Sable Island
70266	Fort Greely, Alaska		25223	Port Hardy
78783	Fort Sherman, Canal Zone		25206	Prince George
72477	Green River, Utah		25152	Vernon
91366	Kwajalein, Marshall Islands		25218	Fort Nelson
87689	Mar Chiquita, Argentina		26316	Whitehorse
82599	Natal, Brazil		26107	Coppermine
74124	Primrose Lake, Canada		27001	Isachsen
72391	Point Mugu, Calif.		26118	Fort Smith
04202	Thule AB, Greenland		26323	Inurik
72402	Wallops Island, VA		26202	Norman Wells
72269	White Sands, NM		16903	Baker Lake
47513	Ryori, Japan		16801	Coral Harbour
70414	Shemya, Alaska		18601	Alert
			18801	Eureka
Total Stations = 19			16603	Frobisher Bay
			16895	Hall Beach
			17901	Resolute
			26005	Cambridge Bay
			27101	Mould Bay
			27201	Sachs Harbour
			04734	Maniwaki
			25145	Edmonton Stong Plain
			25004	The Pas
			15901	Churchill
			15806	Trout Lake
			15803	Moosonee
			71912	Sept-Iles
			15703	Nitchequon
			15704	Inukjuak
			15605	Fort Chimo

Total Stations = 36

a day at 00 GMT and 12 GMT from the 36 Canadian stations listed in Table 3(b).

The Canadian data being mixed (standard pressure levels, significant levels) necessitated development of two programs to combine standard pressure level observations on one tape with the appropriate significant levels observed for the same station, date, and time on a second tape. For example, program CFORM5 was designed to decode card 5 type format from selected stations on a standard level C tape, the results of which were stored on disk file ID5. Program CFORM18 was then implemented to decode and combine all significant levels for a particular station, date, and time with the corresponding standard level data on file ID5. Completed coherent radiosondes resulting from this merging process were saved on thirteen S tapes reformatted for further processing.

Later, a relatively large data set of radiosonde observations (called R tapes) from domestic and foreign sources from mid-1969 through 1981 became available. These data were in standard tape format TDF56 defined in accompanying documentation (Reference Manual, 1971).[40] The upper air observations were for 00 and 12 GMT, but unlike the Canadian data, standard and significant levels were combined, defining a single coherent profile for each observation. Table 4 lists the 138 participating stations contained in this data ensemble.

Another source of data, not shown in Fig. 56, was catalogs of tabulated MRN rocketsonde observations from World Data Center A for the period 1969 through 1976.[41] Use of these data will be discussed in later sections.

_____

40.   Reference Manual, 1971: TDF56 Standard Tape Form and U. S. Standard Atmosphere. Environmental Data Service, National Climatic Center, National Oceanic and Atmospheric Administration, U. S. Department of Commerce.

41.   World Data Center A, Data Report, 1969-1976: High Altitude Meteorological Data. National Climatic Center, NOAA, U. S. Department of Commerce.

TABLE 4. INTERNATIONAL STATION NAMES PROVIDING DATA ON R TAPES

WBAN No.	Station Name	WBAN No.	Station Name
03131	San Diego	03879	Salem, IL
03160	Desert Rock	03946	Monett
23154	Ely	13985	Dodge City
23160	Tucson	13996	Topeka
23194	Winslow	14826	Flint
23230	Oakland	14842	Peoria
24127	Salt Lake City	14847	Sault Ste. Marie
24128	Winnemucca	14898	Green Bay
24131	Boise	14918	International Falls
24143	Great Falls	14926	Saint Cloud
24157	Spokane	14936	Huron
24225	Medford	23062	Denver
24232	Salem, OR	23066	Grand Junction
26411	Fairbanks	24011	Bismarck
26510	McGrath	24021	Lander
26615	Bethel	24023	North Platte
26616	Kotzebue	24090	Rapid City
26617	Nome	25308	Annette
27401	Barter Island	25309	Yakutat
27502	Barrow	25501	Kodiak
94008	Glasgow	25503	King Salmon
94240	Quillayute	25624	Cold Bay
51701	Lima, Peru	25713	Saint Paul Island
52701	Antofagasta, Chile	26409	Anchorage
53701	Quintero, Chile	94918	Omaha
54702	Puerto Montt, Chile	21001	Manzanillo, MX
55701	Punta Arenas, Chile	21101	Socorro Island, MX
62001	Easter Island	22007	Chihuahua, MX
93104	China Lake	22009	Mazatlan, MX
93111	Point Mugu	22012	Monterrey, MX
93116	San Nicholas, CA	22105	Guadalupe Island, MX
03158	San Nicholas, CA	22013	Guadalajara, MX
11501	Barbados	22701	Midway
11903	Mexico City, MX	25704	Adak
22104	Empalme, MX	03881	Centreville
10717	Bogota, Colombia	03937	Lake Charles
10809	San Jose, Costa Rica	03940	Jackson
03133	San Diego	03951	Longview
11641	San Juan, PR	03860	Huntington
11813	Grand Cayman	13723	Greensboro
12717	Nassau	13840	Dayton
12832	Apalachicola	13880	Charleston
12842	Tampa Bay	14607	Caribou
12844	West Palm Beach	14684	Chatham

Continued

TABLE 4. INTERNATIONAL STATION NAMES PROVIDING DATA ON R TAPES (CONTINUED)

WBAN No.	Station Name	WBAN No.	Station Name
12850	Key West	14733	Buffalo
12884	Boothville	14735	Albany
12912	Victoria	14764	Portland
12919	Brownsville	21504	Hilo
13861	Waycross	21603	Johnston Island
13873	Athens	22536	Lihue
13897	Nashville	40308	Yap
13901	Stephenville	40309	Koror
13963	North Little Rock	40504	Ponape
13967	Okalahoma City	40505	Truk
22010	Del Rio	40710	Majuro
23023	Midland	41415	Guam
23044	El Paso	41606	Wake Island
23047	Amarillo	61705	Pago Pago
23050	Albuquerque	93729	Cape Hatteras
11715	Kingston, Jamaica	93734	Washington
11814	San Andres, Colombia	93739	Wallops Island
11817	Tegucigalpa, Honduras	94823	Pittsburgh
11901	Guatemala City, GM	11629	Santo Domingo, D.R.
11904	Veracruz, MX	11634	Trinidad, N. Antilles
12878	Merida, MX	11643	Curacao
70701	Diego Garcia	11645	Saint Maarten
11816	Coluteca, Honduras	11706	Guantanamo, Cuba
11818	Belize	13601	St. George, Bermuda
		16201	Keflavik, Iceland
		93755	Atlantic City

Total Stations = 138

4. Formatting and Data Compression

Three programs shown in portion (b) of Fig. 56 were designed separately to decode the three uncommon formats in which the upper air data were stored on L, R, and S tapes. The first step was to devise a dynamic storage system, common to all three decoding modules, to handle the large quantity of data and insure permanent accommodation space availability on multiuser public and private disk storage media.

The storage system devised relied on random access disk storage methods where record addressing via station identification was supported by inventory files continually updated during the storage process. One record consisting of 5208 60-bit words was designed to handle 14 years of data from one station. Elements within records were addressable through an indexing sequence of 31 days X 12 months X 14 years, or 5208 60-bit words. Each addressable 60-bit word was packed so that for MRN data, right justified bits 1 thru 40 contained four 10-bit bytes representing integer values of density and temperature at 40 and 30 km respectively. A typical 60-bit word for radiosonde data contained six 10-bit bytes representing values of density and temperature at 20, 10, and 5 km respectively. The storage system was initialized to handle 600 (300 stations X 2 observations/day) such records. This amount of storage capacity turned out to be more than ample since the total number of source data stations finally received totaled 367.

Since MRN data on L tapes available at the outset of this study involved a relatively small amount, program SOND2 was designed first and utilized to check out the dynamic storage system that would become common to the other two decoding modules. As implied in Fig. 56, routing of data from MRN L tapes to a public disk file ROCKDA is accomplished by the SOND2 program. File INVEN1 was updated during the routing process to keep track of the addresses of records associated with stations involved.

Programs SOND3 and SOND4 route the larger quantities of data on R and S tapes to RAWNDA file residing on a single private disk and associated inventory information to INVEN2 residing on public disk. The private disk was necessary because the amount of data potentially stored could have exceeded 1.8 million words, which is far in excess of allowable public disk storage. Spooling out the packed data and inventory files on disk to tape

for permanent retention was made possible through program CHECK. During the spooling process, tabulations describing data capture statistics for each station processed were produced for verification.

5. Applications Software

At this point, source data have been packed and stored in two discrete areas; namely, MRN data in file ROCKDA reflecting values of temperature and density at 30 and 40 km levels, and radiosonde data in File RAWNDA containing temperature and density values at 20, 10, and 5 km for each station twice a day. This leads to portion (c) of Fig. 56 which depicts the flow of the applications software developed to derive products that satisfy the given specifications.

Program PROB1 uses INVEN1 and ROCKDA files to determine, for each MRN station available, frequencies of occurrence of temperature and density values recorded at the 40 and 30 km levels. Monthly cumulative probability values of temperature and density occurring at 1, 10, 90, and 99 percentile thresholds were then extracted and retained for each station. On completion of this process, the program searches through the ROCKDA file a second time to locate the dates and times of original soundings having the most extreme values within the four percentiles specified. Resulting stations, dates, times, and values were printed out for examination and stored on file DSORT1.

Program DISPLA1, using DSORT1 as input, was designed to plot and tabulate cumulative probabilities of frequency distributions associated with the most extreme cases at 30 and 40 km. These cumulative probability distributions when displayed graphically often conveniently portrayed areas of suspicious data. For example, values describing cumulative probability distributions on probability graphs normally appear along straight lines; abnormal values can deviate noticeably from the slopes of these lines, visually indicating areas containing suspect values. Subjective interpretation of the graphs produced here revealed several cases where data values on the limbs of some of the distributions deviated significantly from normal events along a line. These particular cases were scrutinized to determine whether or not certain data should be edited out of the analysis. Program EDIT was implemented to eliminate from the data sets on disk

either entire periods of record or individual observations. However, since elimination of data from statistical procedures such as those used here can significantly change results, whenever editing occurred complete reprocessing to derive new results was necessary as indicated by the arrows surrounding EDIT in Fig. 56.

Descriptions of the functions of programs PROB1 and DISPLA1 above apply to programs PROB2 and DISPLA2 as well. The only differences between the two are that dimensions in both programs PROB2 and DISPLA2 had to be increased to handle the more abundant quantities of data available from radiosondes and, of course, access to data had to be from INVEN2 and the large RAWNDA files. Also, data observed at 00 GMT were processed separately from 12 GMT data by programs PROB2 and DISPLA2 to separate diurnal effects (if any) from the resulting statistics. File DSORT2 held the resulting stations, dates, and times of extreme cases for 30, 20 and 10 km levels. In the final analysis, however, this file was ignored and input to DISPLA2 was made via remote terminal in order to provide graphics of statistics for a more selective assortment of stations and months. Editing procedures explained above were also applied to this section of the data processing.

A typical cumulative probability distribution product from the DISPLA programs is reproduced in Fig. 57. It shows the distribution, when matched with several others, possessing the highest (warmest) observed temperatures less than or equal to one percent (cumulative probability greater than or equal to 99 percent) at 5 km. Two out of 193 observations in July months at 12 GMT over Point Mugu, CA recorded the one percent extreme highs.

Programs LIST1, LIST2, and LIST3 are by-products of the decoding sections of programs SOND2, 3, and 4. Their primary function was to locate in original source data tapes, selected individual upper air observations and to print out pressure, temperature, and density at every level recorded. DSORT1 and 2 files were used as input to assist the LIST software in locating the proper most extreme profiles to display. Printed MRN's were hand plotted but selected radiosonde data were plotted using computerized color graphics techniques to exhibit several temperature profiles
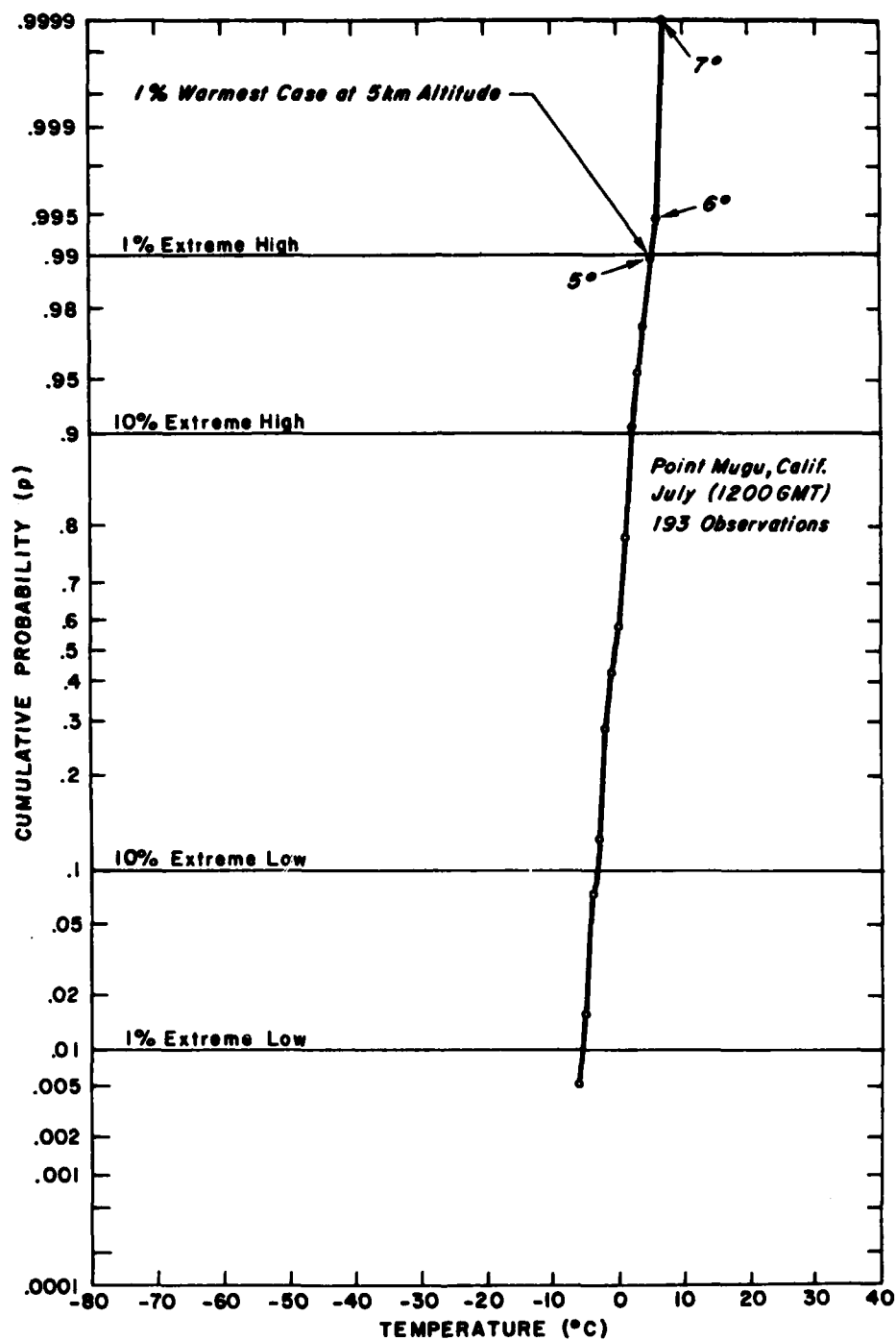
Fig. 57. Typical Cumulative Probability Display Product from DISPLAY Programs

Distribution shown describes the actual 1 percent warmest case at 5 km altitude having a temperature of approximately 5.2° C.

on a single frame, thereby minimizing the number of frames required. Some additional MRN profiles that were needed to pair with radiosonde profiles were hand plotted using data published in High Altitude Meteorological Data catalogs issued by World Data Center A.[41]

Utilizing all products provided by the software discussed thus far, subjective pairing of MRN temperature profiles with lower altitude radiosonde profiles was undertaken. The pairing processes will be described using the "worst" extreme 99 percent highest temperature case at 5 km. Having discovered by elimination techniques the highest temperature case at 5 km using the distribution in Fig. 57, the two temperature profiles taken at Point Mugu on the dates stored in the DSORT2 file that exhibited the phenomenon were extracted from the appropriate R tape and displayed by LIST2 as shown in Fig. 58. The MRN rocketsonde from the same station on 30 July 79 at 1551 GMT residing on a selected L tape was printed out by the LIST1 program and hand plotted for pairing with the two lower level radiosondes, thus extending temperature information from 36 to 60 km. These profiles were used as guides to determine subjectively a single profile (dashed line) that will show realistic vertical structure of a typical atmosphere for the given extreme condition. Resulting temperatures in degrees Kelvin and associated lapse rates between levels (right side of Fig. 58) were extracted for input to further refinement described below.

Input from the pairing process for 40 cases (5 altitude levels X 2 parameters X 4 percentiles) was stepped into the computer in a format suitable for program AFSA (Atmospheric Formulas for Supplemental Atmospheres). Hydrostatically consistent results were produced in tables showing temperature, pressure, and density values at selected geometric as well as geocentric altitudes from the surface to 80 km for each of the 40 cases involved. Further discussion and final results of this study are presented in Profiles of Temperature and Density Based on 1 and 10 Percent Extremes in the Stratosphere and Troposphere.[42]

---

42. Kantor, A. J., and P. Tattelman, 1984: Profiles of Temperature and Density Based on 1 and 10 Percent Extremes in the Stratosphere and Troposphere. AFGL-TR-84-0336, Air Force Geophysics Laboratory, Hanscom AFB, MA.
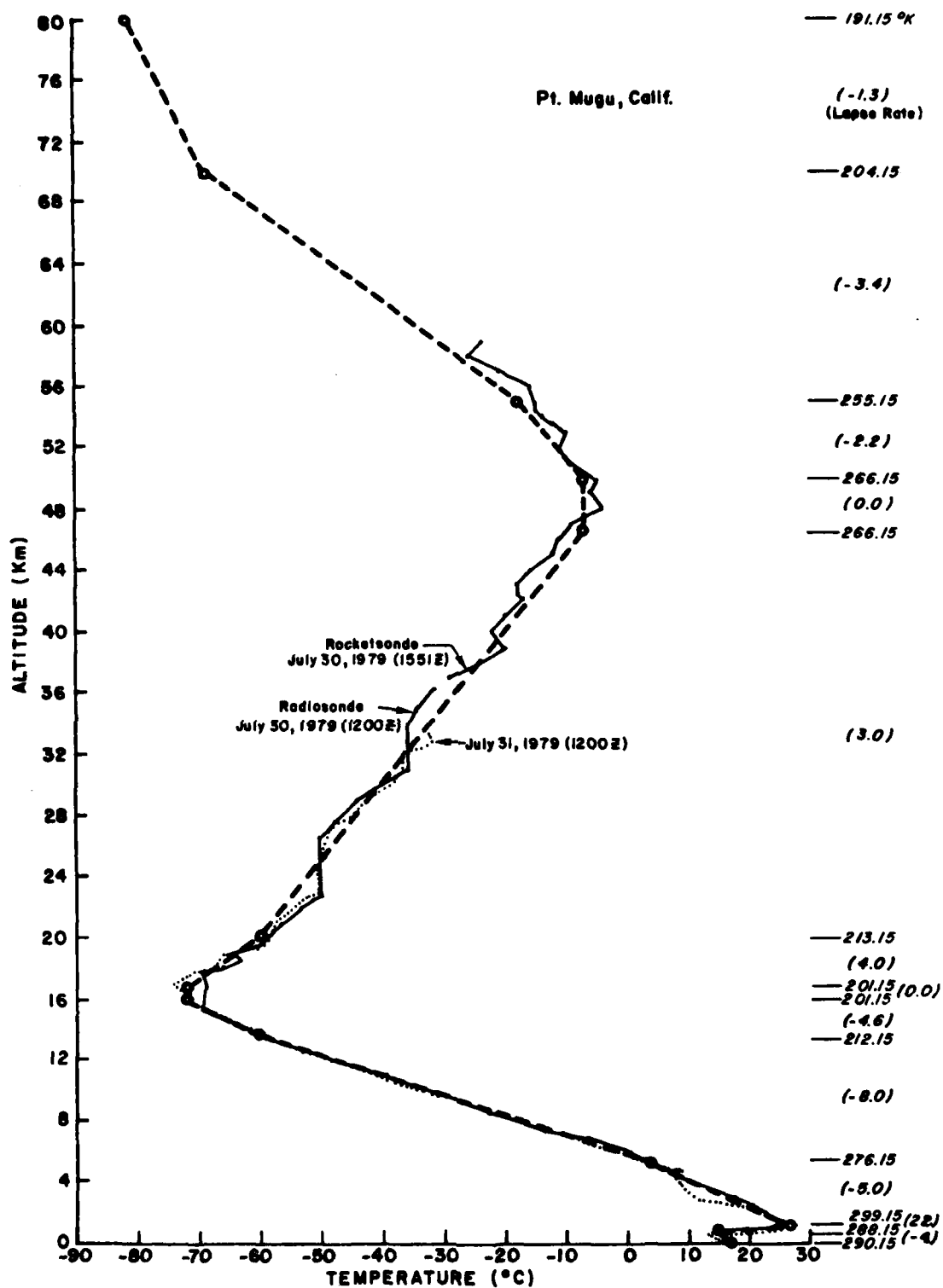
Fig. 58. Radiosonde-MRN Pairing for Input to Program AFSA

B. Cloud Amounts over Small Cumulus Cloud Fields

1. Introduction

Sensor field of view can be of concern in the accurate detection of clouds for deriving cloud amounts from earth viewing satellites. For example, clouds that do not fill the field of view of a low resolution sensor may go undetected. To investigate very high resolution sensor capability for more accurate cloud detection, especially over small cumulus cloud fields, an ensemble of LANDSAT-2 data providing nominal 80 m X 80 m resolution observations from multispectral scanner (MSS) sensors was acquired. The computer processing and display products provided by SASC for that investigation are discussed in this section.

2. Specification

Specifications for LANDSAT-2 MSS data processing support for this study are:

* From LANDSAT-2 data tapes on hand, make copies for distribution to others needing data.
* Provide full images of the data using the visible channel (band 4).
* Provide images of selected subsections of the data at full resolution for any of the bandwidths provided.
* Investigate the usefulness of an interactive color graphics processor for displaying satellite data.
* Support technique development for determining cloud amounts over areas of varying cumulus cloud sizes within given nautical mile grid squares.

These specifications may change and new ones may emerge as this study progresses.

3. Data Sources

LANDSAT-2 MSS data from the EROS Data Center (EDC), Sioux Falls, SD were received on eighteen tapes containing coded radiance values from four band widths (4, 5, 6, and 7) at wavelengths of 0.5 - 0.6, 0.6 - 0.7, 0.7 - 0.8, and 0.8 - 1.1 microns respectively. Associated documentation was also

155

provided (Holkenbrink, 1978).[43] The nominal 80 m X 80 m resolution data within an imaged ground area of approximately 185 km across track by 170 km on track covered nine selected regions, mostly over the Bahamas. One full scene over each selected area requires two tapes. Actual dates, assigned tape numbers, and center latitude-longitude for the data are listed in Table 5.

TABLE 5. LANDSAT-2 MSS DATA AVAILABILITY AT AFGL

Observation Date	AFGL Assigned Tape No.	Center Latitude (°N)	Longitude (°W)
10/31/80	T0001, T0002	26.0	79.5
12/05/80	T0003, T0004	24.5	78.0
09/24/80	T0005, T0006	24.5	78.0
09/24/80	T0007, T0008	23.0	78.5
09/25/80	T0009, T0010	24.5	79.5
09/08/80	T0011, T0012	24.5	81.0
12/08/80	T0013, T0014	26.0	82.0
10/31/80	T0015, T0016	24.5	79.5
11/18/80	T0017, T0018	24.5	79.5

4. Software Development

Fig. 59 depicts the software and various products thus far produced for processing the LANDSAT-2 MSS data. The mainframe computer at AFGL was utilized for reducing the large amounts of data to sizes acceptable to smaller computer systems, such as McIDAS, and to restricted storage allocation allowances for public disk storage.

Program LTAPES was designed to copy the LANDSAT-2 data onto additional tapes for distribution to others involved in cloud morphology studies. The program allows direct copying of a full scene onto two tapes recorded at 1600 B.P.I. or, as a second option, a full scene to a single tape recorded at 6250 B.P.I. Copied tapes differ slightly from originals

---

43. Holkenbrink, P. F., 1978: Manual on Characteristics of Landsat Computer-Compatible Tapes Produced by the EROS Data Center Digital Image Processing System. Rev., United States Geological Survey.
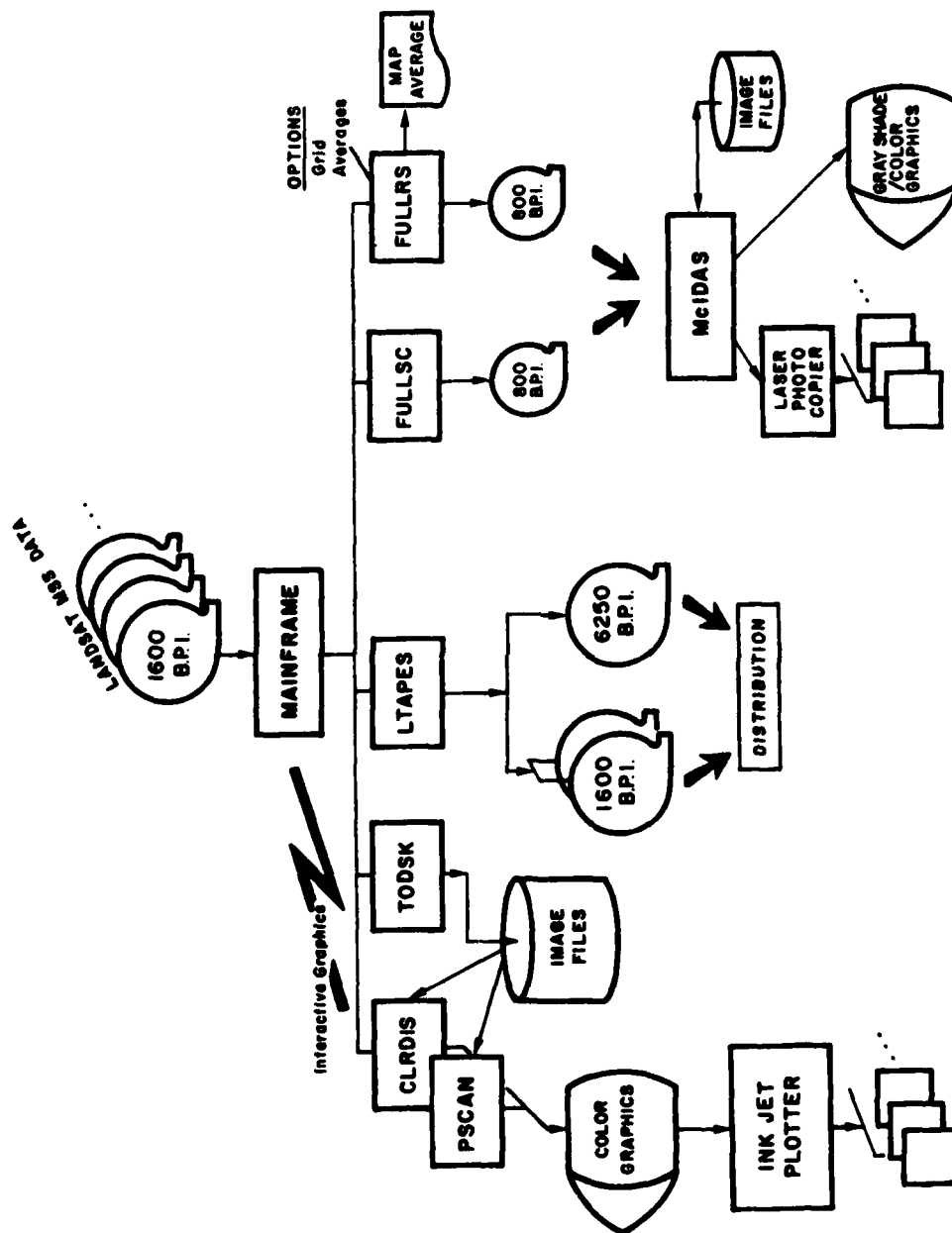
Fig. 59. Satellite High Resolution MSS Data Handling Configuration

in that physical records on originals that are not divisible by 60 are copied with 32 additional trailer bits per physical record. For example, original records containing 479 60-bit words plus 28 bits are copied as 480 60-bit words. The extra 32 bits are to be ignored.

Image film products from EDC that normally accompany LANDSAT data tapes were not ordered for the cases involved in this study. Therefore program FULLSC was designed to compress a full scene of band 4 data to a manageable size for display purposes through use of the McIDAS image display system. The compression technique uses an averaging process explained below.

Average digital values that make up a single scan line in a full image photo are derived by summing segments of six consecutive LANDSAT pixels over six sequential band 4 scan lines as in Eqs. (6) and (7).

$$B_{(i/6 + 1)} = \sum_{\text{Scan line} = 1}^{\text{Scan line} = 6} \sum_{i = N}^{i = N + 5} \text{Pixel}_i \tag{6}$$

for $N = 1, 7, 13, \ldots, 3541$
where B is a 591 element array.

Then, for each compressed scan line, average B_i is computed by

$$\bar{B}_i = B_i/36 \text{ for } i = 1, 2, 3, \ldots, 591. \tag{7}$$

The process effectively compresses full images originally dimensioned 3546 pixels by 2982 scans to 591 pixels by 497 scan lines. During the process saturated values stored in additional pixels on both sides of compressed scan lines are inserted that are not part of the LANDSAT data but are made as markers available to represent every 60 uncompressed image scan lines. The markers are useful as guides for determining locations of full resolution image sectors (explained later). Both LANDSAT tapes making up a full image are needed as input to FULLSC to produce and store the compressed images onto 800 B.P.I. tapes. Using McIDAS, 16-level grayshade photos of the compressed data are generated on a laser display unit. Fig. 60 shows an image generated from the data received 31 Oct 80, mostly off
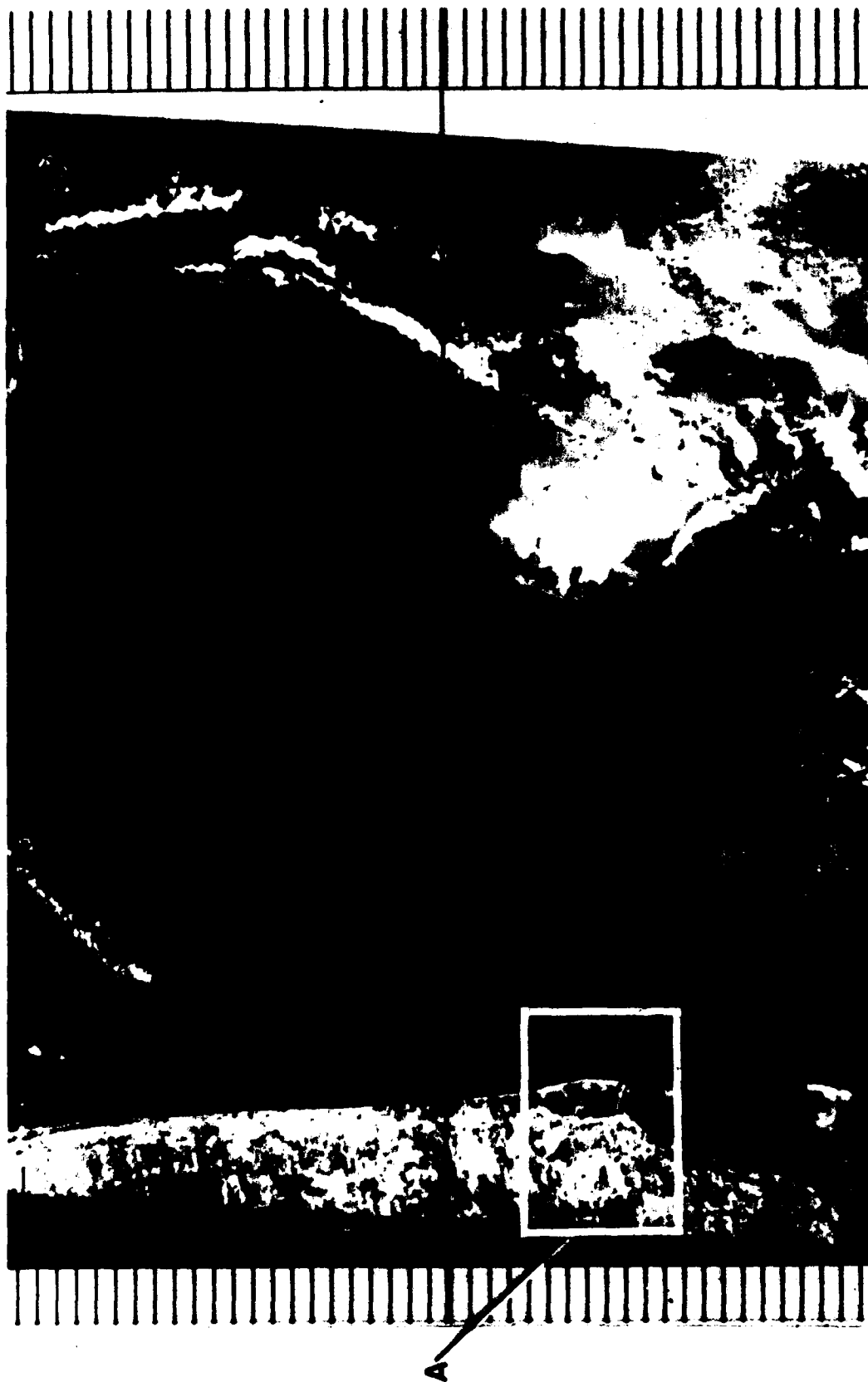
Fig. 60. Compressed Full Image LANDSAT MSS Data From Band 4 on 31 Oct 80

A cloud free land area (left) extends from Palm Beach southward over Miami, FL. Small cumulus clouds are visible eastward over the Atlantic. The southern inflection point of Grand Bahama Island is visible at the top right. Every 60 scans are depicted by markers on both sides of the image and the center line divides the information contained on a volume one tape from that on a volume two tape.

159

the east coast of Florida. The solid black line through the center of the figure is produced by the compression process to distinguish information contained on a source one data tape (top) from that on a second source data tape (bottom). Annotation is provided over a small portion of the bottom of each image identifying year and Julian day of data acquisition. These compressed full images are extremely useful for selecting subsections that can be extracted and displayed at full resolution.

Extraction of the data at full resolution was made possible through the design of a program called FULLRS. Selected subsections extracted are recorded on tape at a density of 800 B.P.I. A grid option is provided to allow the insertion of vertical and horizontal grid lines at given pixel – scan line intervals for scaling and reference purposes. Display capabilities of the McIDAS are again employed to produce grayshade photos of the subsections created. Each subsection is composed of 672 pixels by 470 scan lines. To produce these images, a return to the original LANDSAT data tapes is necessary. A desired bandwidth number (4, 5, 6, or 7) and the initial pixel and scan line number coordinates of the upper left corner of a full resolution area are also necessary.

Two transparent diagrams were invented to assist in the area extraction. One is a MSS full image pixel alignment diagram (Fig. 61), the second is a full resolution data extraction window (Fig. 62). Initial co-ordinates of desired areas are obtained by first overlaying the LANDSAT MSS full image pixel alignment diagram in Fig. 61 on the compressed full image picture. Second, the LANDSAT MSS full resolution data extraction window (Fig. 62) is laid over the appropriate area of interest within the compressed full image. Finally, the resulting pixel and scan line coordinates of the top left corner of the window area are read off, using the x and y scales in Fig. 61. Full resolution subsection A of Fig. 60 with upper left coordinates at pixel 120 and scan line 1740 was a specially chosen section extracted primarily over a cloud free land area that will be used for deriving scaling parameters discussed later on. The full resolution subsection is shown in Fig. 63. The figure reveals features that would otherwise go unnoticed by sensors with lesser resolution, such as those on conventional meteorological satellites. For example, several of the causeways spanning Biscayne Bay from Miami to Miami Beach are readily discernible. Okeechobee road along the Miami Canal appears as a diagonal line extending inland northwestward from Miami.
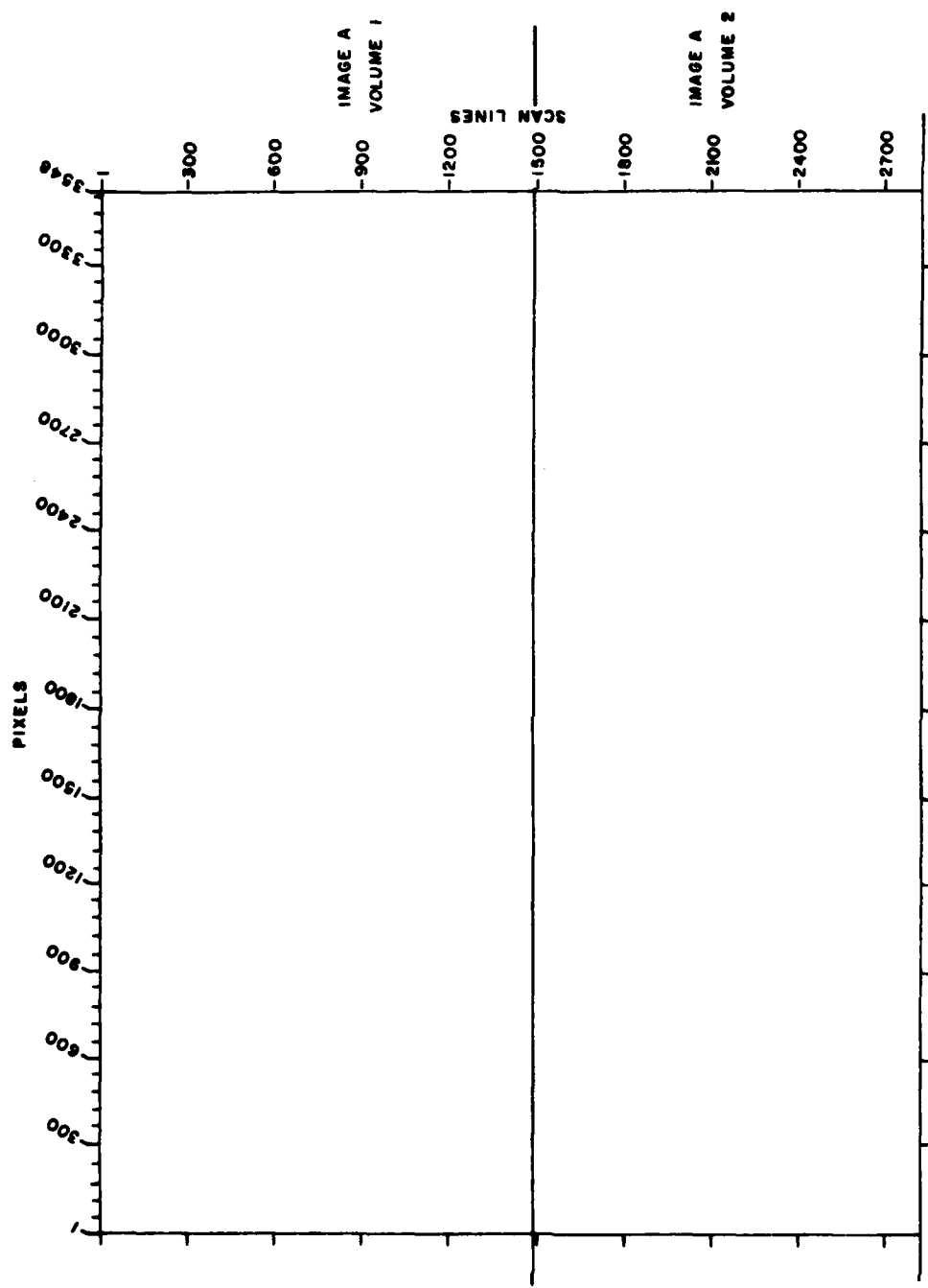
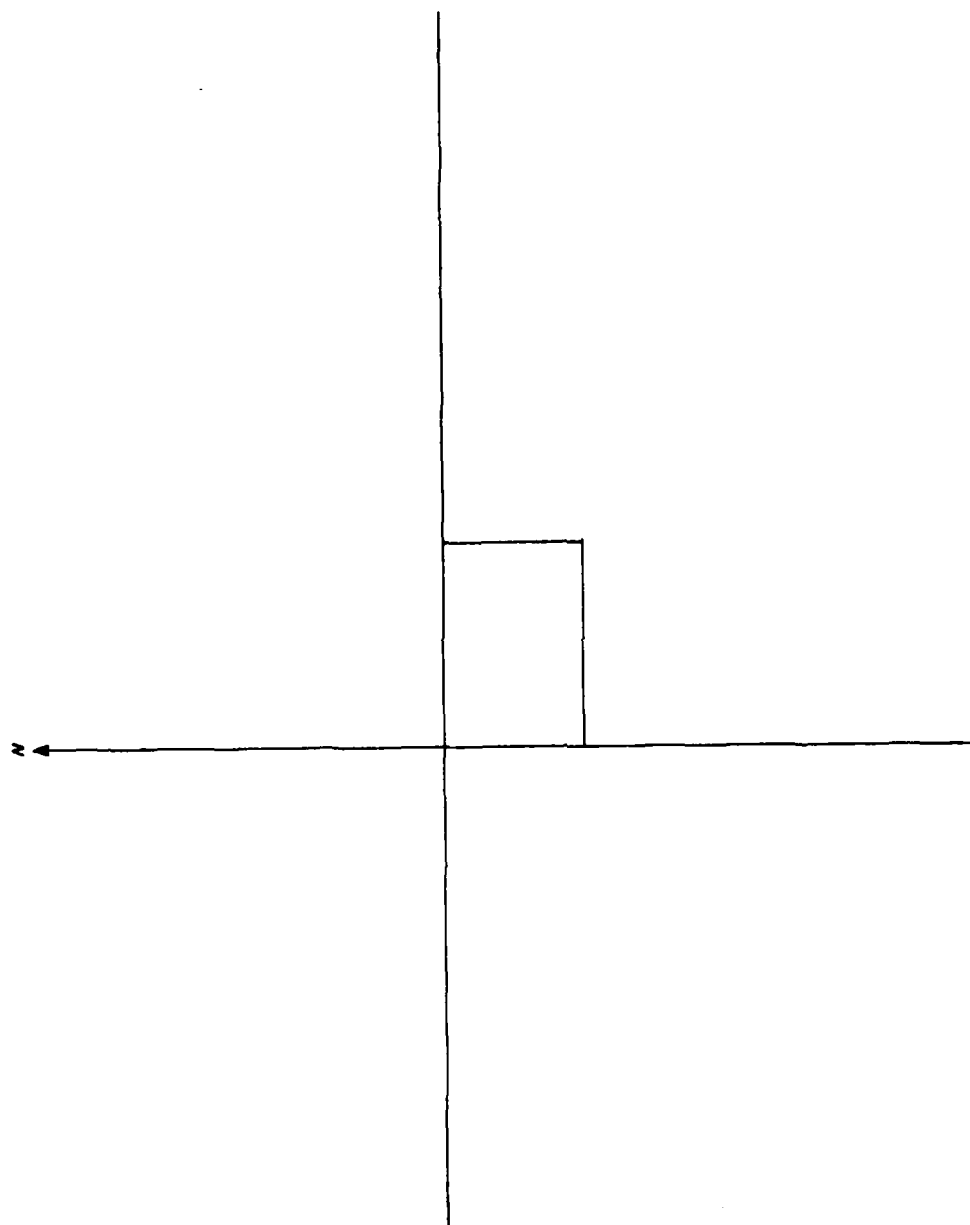Fig. 61. LANDSAT MSS Full Image Pixel Alignment Diagram

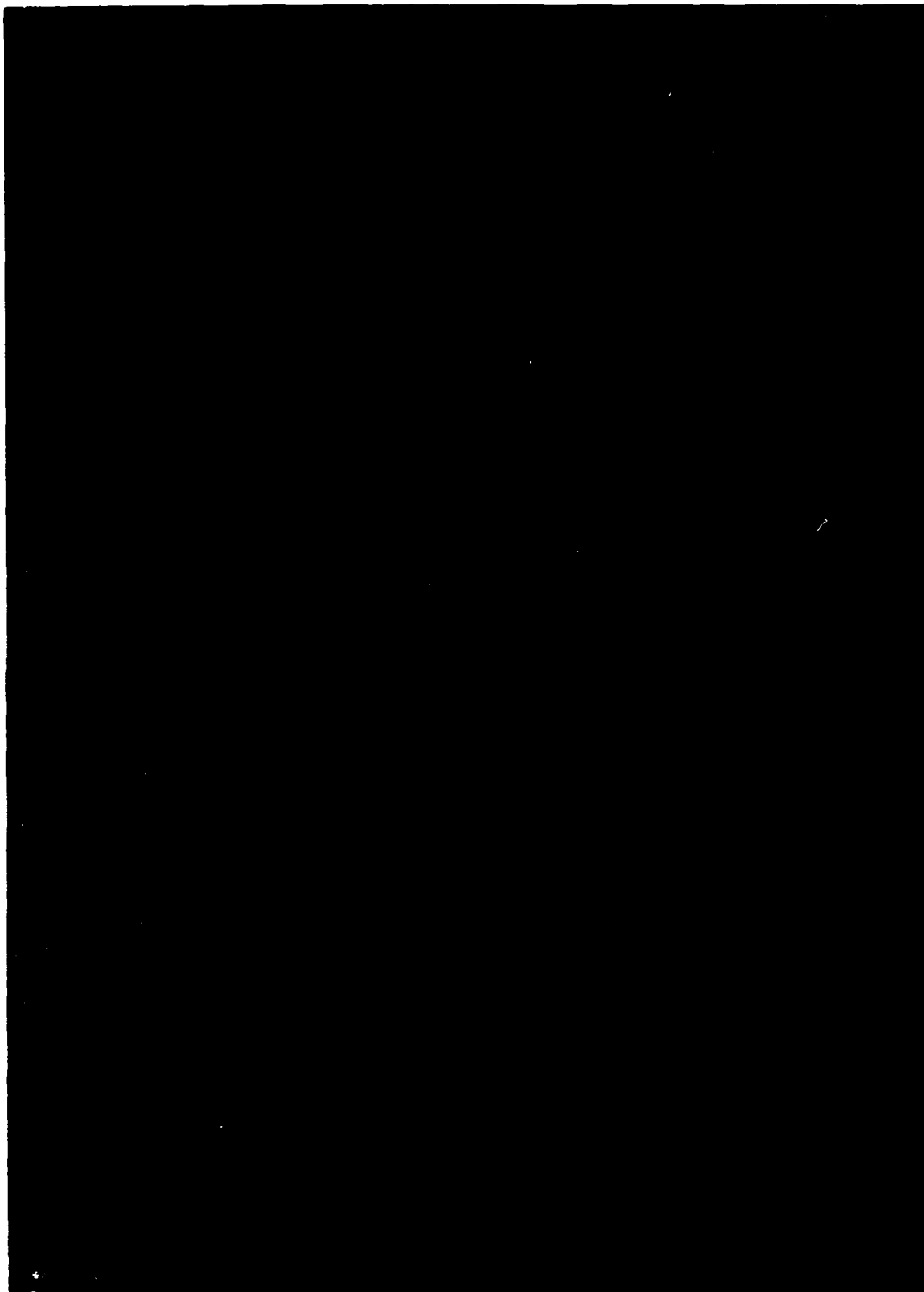Fig. 62. LANDSAT MSS Full Resolution Data Extraction Window

Fig. 63. Full Resolution Subsection from (A) in Fig. 60 Mostly over Miami, FL
Grid lines are included for scaling purposes.

A grid option is provided by program FULLRS to allow the display of grid lines on full resolution subsection photos that define specified .75 nm grid cells. Photo interpretation techniques were used to derive the pixel-scan line dimensions for the grid cell in which a section of the photo from Fig. 63 showing land features mostly in the Miami Beach - Biscayne Bay area was used in conjunction with a 1:250000 Transverse Mercator map projection over the same area (see Fig. 64). As shown on the photo in Fig. 64, 21 pixels span from one vertical line to the next and 25 scan lines lie between one horizontal line and the next. Given these dimensions it can be seen that in the horizontal direction 64 pixels lie between a point on North Bay Village eastward to another point on the western coastal boundary of Miami Beach. In the vertical direction, 162.5 scan lines make up the portion of the photo between a point on the western coastal boundary of Surfside southward to a point in the middle of Belle Island. Distances in nautical miles between these points are shown on the conventional map adjacent to the photo. Relationships (a) and (b) below were then formulated to compute the number of pixels x and scans y that approximate the cell size:

$$x \ : \ 64 \ \text{pixels as} \ .75 \ \text{nm} \ : \ 1.9 \ \text{nm} \qquad (a)$$
$$y \ : \ 162.5 \ \text{scans as} \ .75 \ \text{nm} \ : \ 5 \ \text{nm.} \qquad (b)$$

Then

$$x = 25.3 \ \text{pixels}$$
$$y = 24.4 \ \text{scans.}$$

Since fractions of pixels and scans are not possible, the final cell size was specified to be 25 pixels by 25 scans, where the last columns of pixels and rows of scans will be saturated by the program to make grid outlines visible on the photos. In Fig. 65 a full resolution subsection containing cumulus clouds of various sizes as viewed by band 7 over the Florida straits on 25 Sept 80 is shown with the .75 nm grid superimposed.

An averaging process, Eq. (8) below, was also added to program FULLRS to be used on option for computing average digital counts within each grid cell:
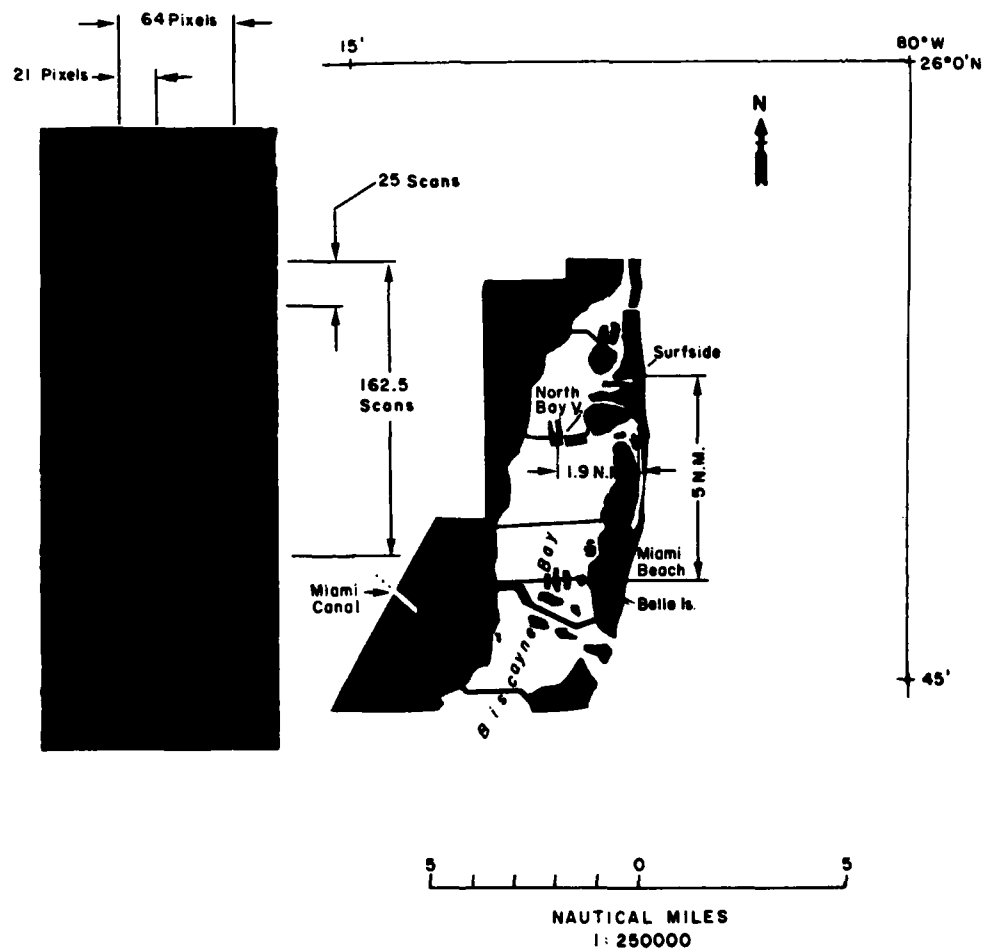
Fig. 64. Photo Interpretation Scheme for Deriving .75 nm Grid Cells

Pixel-scan counts of discernible land marks from a portion of the photo in Fig. 63 over the Biscayne Bay-Miami Beach area (left) are paired with distances on the conventional map (right).

Fig. 65. Cumulus Clouds over Florida Straits from Band 7 on 25 Sept 80

Grids are superimposed to represent approximate .75 nm grid cells.

$$\left[\sum_{Scan = 1}^{Scan = 24} \sum_{i = 1}^{i = 24} Pixel_i\right]\Bigg/ 576. \qquad (8)$$

Printouts of the results in map form are provided, which will be combined with average cloud amounts derived subjectively using the visual products similar to Fig. 65.

As the next step, a cloud/no cloud threshold criterion is being investigated that will be used objectively to separate clouds from the ocean background. A 4115B Tektronix high resolution color graphics terminal is being used to assist in the visual interpretation of the results.

Program TODSK, similar to FULLRS, is utilized first to provide smaller subsections of the original LANDSAT MSS data on public disk image files for optimum interaction with the software supporting the color graphics terminal. These image files provide input to program PSCAN designed to plot digital count values of pixels along chosen scan lines. The top of Fig. 66 shows, for example, plots of the digital counts that occur along a single scan line extracted from band 7 to compare with the digital counts for the same scan line as observed from band 4. Graphs of this type can be useful for determining cloud/no cloud threshold values. For instance, the dashed line across the band 4 distribution (Fig. 66) at digital count value 65 might be one of several values of interest in deriving a satisfactory cloud/no cloud discriminator. This threshold is utilized by the CLRDIS program which displays pictorially the results of the cloud/no cloud decision as it is applied throughout the entire image, as shown at the bottom of Fig. 66. Thresholds resulting from these procedures will be combined with the existing averaging process as a final cloud/no cloud decision device for computing cloud amounts over small cumulus cloud fields.
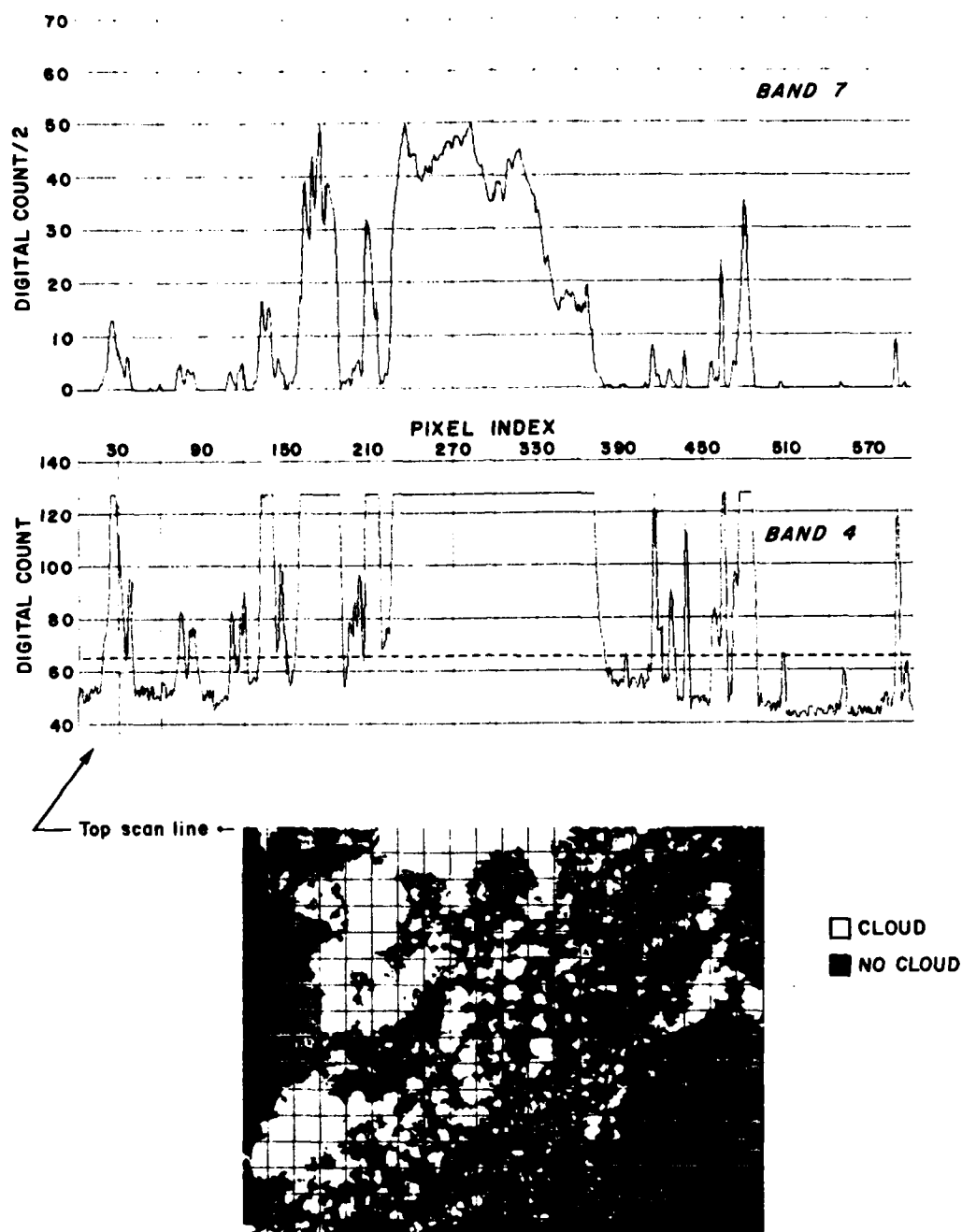
Fig. 66. Interactive Graphics Displays of Pixel Distributions from Band 7 and 4 Together with Full Resolution Image as it Appears Using the Cloud-No Cloud Threshold in Band 4 (Note that band 4 digital counts saturate at 128)